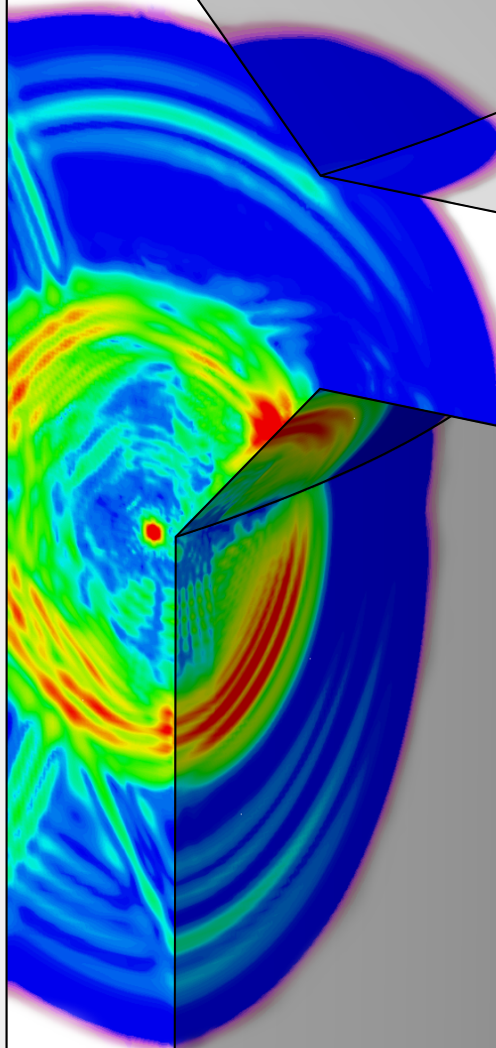# Investigating the Behaviour of Acoustic Emission Waves near Cracks

Using the Finite Element Method

ing. N.L. van Rijn

TUDelft

Delft
University of
Technology

Challenge the future

Investigating the Behaviour of Acoustic Emission Waves near Cracks

Using the Finite Element Method

by

ing. Nicolaas Leendert van Rijn

in partial fulfillment of the requirements for the degree of

Master of Science

in Offshore & Dredging Engineering
Structural Analysis and Design

at the Delft University of Technology,
to be defended publicly on Tuesday November 14, 2017 at 4:00 PM.

An electronic version of this thesis is available at http://repository.tudelft.nl/.

PREFACE AND ACKNOWLEDGMENTS

<div align="right">

ing. *N.L. van Rijn*
Delft, October 2017

</div>

ABSTRACT

During fatigue crack growth of metallic structures, acoustic stress waves are introduced into the material. These *acoustic emission* waves are the result of the sudden stress release during the nucleation of the crack surface. Using dedicated acoustic emission monitoring equipment, these waves can be recorded. When multiple sensors are able to pick up the waves of a certain fatigue crack growth step, the location of this crack can be determined by using the differences in time of arrival of the signals at these sensor locations. This localization is performed by the method of multilateration, which is the same method that is used to calculate the epicentre of earthquakes.

TU Delft and the 4D-Fatigue joint industry project will use acoustic emission to predict fatigue crack depth, in order to determine the crack growth rate in a multi-axial fatigue loaded test specimen. The location of the fatigue crack will be known, so sensors can be applied very close to it. This use of acoustic emission is unconventional due to the fact that most appliances focus on a much larger scale, since this is one of the advantages of this method. The accuracy goal which is set during this project is also far exceeding traditional use, aiming at a crack depth prediction with an error less than 1 mm. Little literature on acoustic emission focuses on this close range, inducing the need for additional research.

The goal of this thesis is to perform finite element simulations, in order to determine the behaviour of acoustic emission waves in close proximity of the crack. This knowledge should be used to determine what accuracy values are achievable, and whether there are ways to improve on this accuracy.

The first step in order to achieve this goal was the simulation of a Hsu-Nielsen source, more commonly referred to as a *pencil lead break*. This is a very simple to perform acoustic emission source, and will serve to establish appropriate finite element simulation parameters. This simple first step is also convenient to establish the effect the acoustic emission monitoring equipment has on the obtained signals. The multiple filter steps which are performed by the hardware, and the frequency response of the sensor have a great influence on the signal. Pencil lead breaks were performed on a steel plate of 5 mm thickness, at several distances of a sensor. Signals produced by the simulations were verified by the experimental signals in a range of 5 mm–70 mm, verifying the used simulation methods.

The next step was to simulate actual fatigue growth in the same steel plate of 5 mm thickness. Experimental signals were attempted to be acquired during fatigue tests of the plate. The fatigue machine that was used however, turned out to produce high amplitude noise, making it not possible to obtain the desired signals. Since verification of the simulated signals would not be possible, several source models were investigated in order to simulate fatigue crack growth acoustic emission, comparing the localization results with each other. Localization using conventional methods were able to achieve an accuracy of 0.6 mm. Using a new method of wave speed determination however, which makes use of the simulation results, the localization accuracy was improved to 0.4 mm.

The final step was to perform a simulation of a specimen which is used by the 4D-Fatigue JIP. This *tubular specimen* contains flanges, which reflect inbound waves back to the sensors, potentially influencing the localization accuracy. The simulations however, concluded that these reflections arrive after the initial wave has passed. The effect on localization was found to be negligible. Localization using conventional methods was not found result in reliable data. This decrease in accuracy compared to the accuracy found in the 5 mm plate, is attributed to the larger differences in travel distance the signals have, due to the 10 mm thick body of the tubular specimen. Localization using the new speed determination method, resulted in a localization accuracy of approximately 1 mm.

Although localization accuracy was found to be sufficient to satisfy the initial goal of 1 mm, it should be noted that the localization was performed using an estimated noise amplitude value. Also, during these numerical simulations the sensor is exactly known, which is not the case during experiments, so additional location error should be taken into account. The work in this thesis does however describe multiple phenomena which influence the localization accuracy, and forms basis for further research to improve on it.

CONTENTS

LIST OF FIGURES

LIST OF TABLES

GLOSSARY

ABBREVIATIONS

AE	Acoustic Emission
AEM	Acoustic Emission Monitoring
AIC	Akaike Information Criterion
BK	Baer & Kradadolfer
CFRP	Carbon Fibre Reinforced Plastic
FE	Finite Element
FIR	Finite Impulse Response
HC	Hinkley Criterion
IIR	Infinite Impulse Response
JIP	Joint Industry Project
LUCY	Location Uncertainty
MA	Maximum Amplitude
PLB	Pencil Lead Break
TDOA	Time Difference of Arrival
TOA	Time of Arrival
TS	Tubular Specimen

NOTATION

A	amplitude	α	angle
c	velocity of sound	ϵ	strain
E	elasticity modulus	λ	wave length
F	force	ν	Poisson's ratio
h	half plate thickness	ρ	mass density
k	wave number	σ	stress
t	time	τ	shear stress
U	displacement	ω	angular velocity

SUBSCRIPTS

a	arrival
ax	axial
e	estimated
exp	experimental
g	group
i	index number
L	longitudinal
m	measured
n	sample number
p	phase
ref	reference
s	surface
sim	simulation
T	transverse

<div align="right">

1

</div>

<div align="right">

INTRODUCTION

</div>

This chapter aims to provide an introduction to the involved parties and the subject of acoustic emission (AE). A problem statement and the thesis goal will be described, followed by the intended approach and the thesis outline.

1.1. CONTEXT

The involved parties include the 4D-Fatigue joint industry project (JIP) and Allseas Engineering B.V. A brief introduction will be given here.

1.1.1. 4D FATIGUE JIP

The initiative of this graduation assignment lay with the 4D Fatigue JIP. This JIP investigates multi-axial fatigue, in order to obtain a reliable way to assess the resulting damage in welded joints which are variable amplitude loaded. A testing machine has been designed for this purpose. The machine consists of two hydraulically driven Stewart platforms, in which both ends of the specimen will be loaded. This way, the specimen can be loaded with six degrees of freedom (main platform) and the applied force can be measured (smaller platform). As this machine, dubbed "Hexapod", is being manufactured and assembled, the research in this thesis is performed in anticipation of its commissioning.

The multi-axial fatigue phenomenon is aimed to be investigated using a *tubular specimen* (TS) and a *bar specimen*. The TS, on which emphasis will be laid during the last part of this thesis, consist of a tubular member, containing weld and flange geometry. A microscopic defect will be applied at a certain location in the weld toe, to ensure the fatigue crack initiates in the intended location, and speed up the fatigue initiation process.

1.1.2. ALLSEAS ENGINEERING B.V.

Allseas Engineering B.V. was founded in 1985 by Edward Heerema. Since then it has grown to one of the largest offshore pipelay and subsea installation companies. The company is based in Switzerland, but has multiple offices all over the world. With the recent addition of *Pioneering Spirit* to the existing fleet of five in-house designed pipelay and support vessels, it entered the market of heavy lifts, installing and decommissioning offshore platforms. Since multi-axial fatigue is a phenomenon occurring in ship hull structures, the assessment of this type of damage is of great interest for Allseas. The membership of the 4D-Fatigue JIP therefore is a logical step.

1.2. ACOUSTIC EMISSION MONITORING

Figure 1.1 gives a simplified overview of the AE system. AE monitoring starts at *A*, which represents the AE source. The AE source introduces waves in the material *B*, in which they will be affected by interaction with geometry and dispersion. At some point, the waves will be picked up by a transducer *C*, which transforms their motion to an electric signal. In order for the signal to travel greater distances through a coaxial data cable, a pre-amplifier *D* amplifies the signal. The signal arrives at one of the ASIP-2 signal processing cards *E* in the AMSY-6 unit *F*. This card does the analog to digital conversion, along with several filter passes. The

<div align="center">

1

</div>
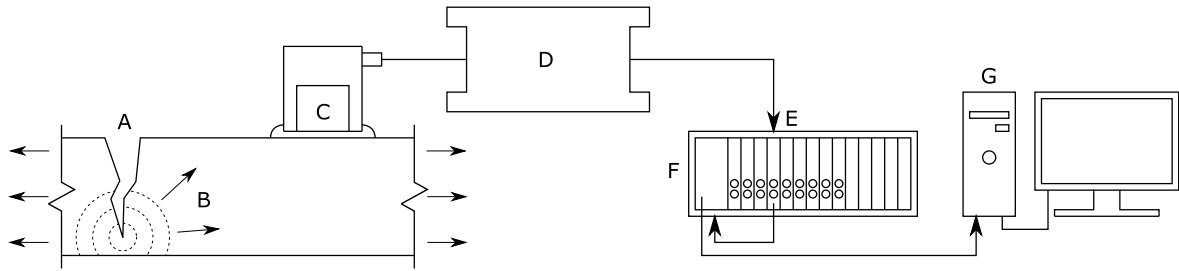
Figure 1.1: Overview of total AE system

AMSY-6 unit 'collects' the signals from the several ASIP-2 cards, and provides the interface with the personal computer *G*. Here the data can be analyzed further, to find the source location and form a prognosis on structural damage. This section will provide an introduction to all mentioned topics.

1.2.1. APPLICATIONS OF ACOUSTIC EMISSION

Acoustic emission monitoring is often used to detect fatigue crack growth, but is not limited to it. Corrosion fatigue, pitting corrosion, valve leakage, seismic activity and high-voltage partial discharges in transformers can also be detected. The AE monitoring equipment should be selected based on several influencing factors such as the material and geometry of the specimen, as well as the source mechanism which is investigated, and the noise in the environment.

A distinction can be made between short-term and long-term monitoring. During short term monitoring, a single controlled overload test is performed. In these conditions, effort can be made to rid the environment of noise generation. Long term monitoring can be performed during in-service conditions. The amount of events which are detected in a certain area can lead to a prognosis on the severity of a certain source mechanism.

The application of AE monitoring lies in a broad scale range. [14] describes full scale fatigue testing of a tubular *K joint*. While this experiment was focussed on a single joint, the monitoring of every weld in a complete pressure vessel with a length of 25 m and a diameter of 4 m can also be performed [22]. The latter case would involve sensor distances of several metres, while during the former case it could be much smaller, in the range of 0.5 m.

1.2.2. ACOUSTIC EMISSION SOURCES

An often used example of acoustic emission is the breaking of a tree branch. A loud cracking noise can be heard, as a result of the breaking of individual fibres. During fatigue crack growth in metallic structures, the amplitude of AE waves are much smaller, but a comparable phenomenon can be witnessed. During mechanical loading of a specimen, the material is stressed up to a point where a nucleation of the material will occur. This sudden release of stress produces elastic stress waves, which travel through the material, and can be detected with sensors.

In this thesis, great emphasis is layed on AE by pencil lead breaks (PLB), and by fatigue crack growth. Unfortunately there are other sources of AE, literature reports several source mechanisms of AE during fatigue loading [3],[4],[11], [14], [26]. These sources include:

- Environmental mechanical noise. Two examples would be the mechanical gripping of the specimen by the fatigue testing machine or a collision between two objects. These signals tend to be in the low frequency range, from 10 Hz to 200 kHz.

- Environmental electrical noise. This can be the switching on of a light source in a room, of magnetic waves from nearby machinery. These signals are typically far above 1 MHz.

- Plastic deformation in the specimen. The change of the crystal lattice of the material is accompanied by AE waves.

- Friction between the crack surfaces. During the opening and closing of the crack, collision between the crack surfaces can generate waves, comparable to mechanical noise.

(a) Burst signal

(b) Continuous signal
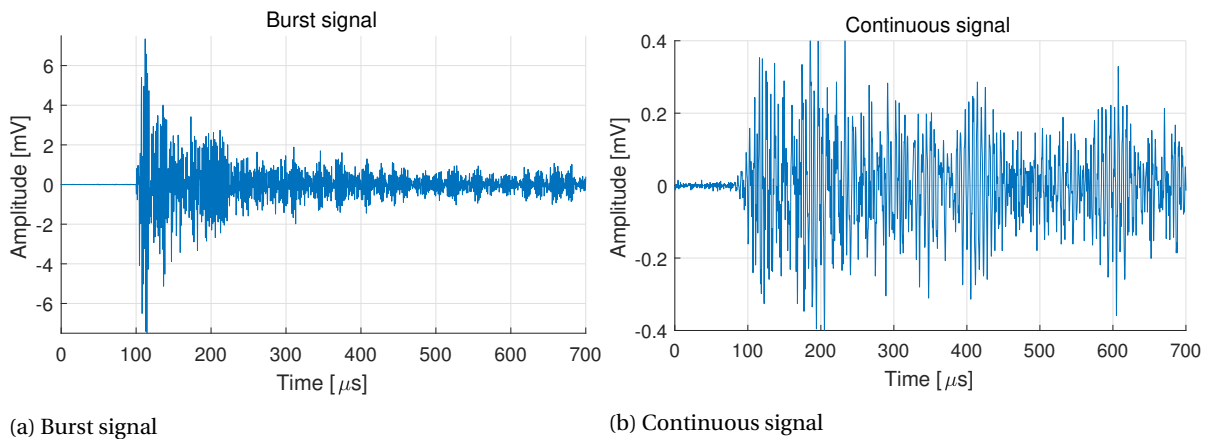
Figure 1.2: Signal waveform types

Figure 1.3: 0.5 mm and 0.35 mm Hsu-Nielsen sources

Several authors report different frequency ranges and characteristics for plastic deformation and crack growth in different materials and specimen types. A consensus however is that a distinguished signature of crack growth is its sharp burst-like signal, which has a small rise time, and diminishes quickly after its peak. An example is shown in Figure 1.2a. The authors agree that plastic deformation is characterized by continuous types of waves, shown in Figure 1.2b.

Hsu-Nielsen source   A very specific type of AE source mechanism is the Hsu-Nielsen source, more commonly referred to as pencil lead break (PLB). As the latter name suggests, the basis for this source is the breaking of a simple pencil lead, usually this is a ⌀0.35 mm or ⌀0.5 mm with a 2H hardness. The breaking is performed using a special mechanical pencil, which has an aiding ring on it, to ensure the breaking is done under a consistent angle with respect to the surface. Figure 1.3 shows two Hsu-Nielsen sources. The underlying principle of the source is that a force is applied to a small area of the plate, which is suddenly released after the breaking of the pencil lead. This sudden release in pressure introduces a sharp burst-like wave in the material.

This wave form is similar to a wave originating from fatigue crack growth in the way that it has the same burst-like form, which is shown in Figure 1.2a. Other aspects which make the use of PLB's convenient are the fact that they have a high repeatability, are very cheap and are simple to perform. They are widely used to calibrate and verify AE equipment setups. Because of the mentioned characteristics of PLB's, this source is used during this research as an initial goal to reproduce with simulations.

1.2.3. ACOUSTIC EMISSION WAVES

Once the AE source has introduced elastic stress waves into the material, these will start to spread throughout the structure. One particular wave type that is often used in AE monitoring is the Lamb Wave. This type of wave forms in thin plate-like bodies, which are often used in engineering structures, e.g. bridges, ship hulls and pressure vessels. The fact that Lamb waves have a great travel range, makes them useful for AE monitoring purposes, because less sensors will need to be applied. Lamb waves have an infinite number of

(a) Sensor applied to steel plate   (b) AEP5H Pre-amplifier   (c) AMSY-6 system, containing ASIP-
                                                                          2 cards
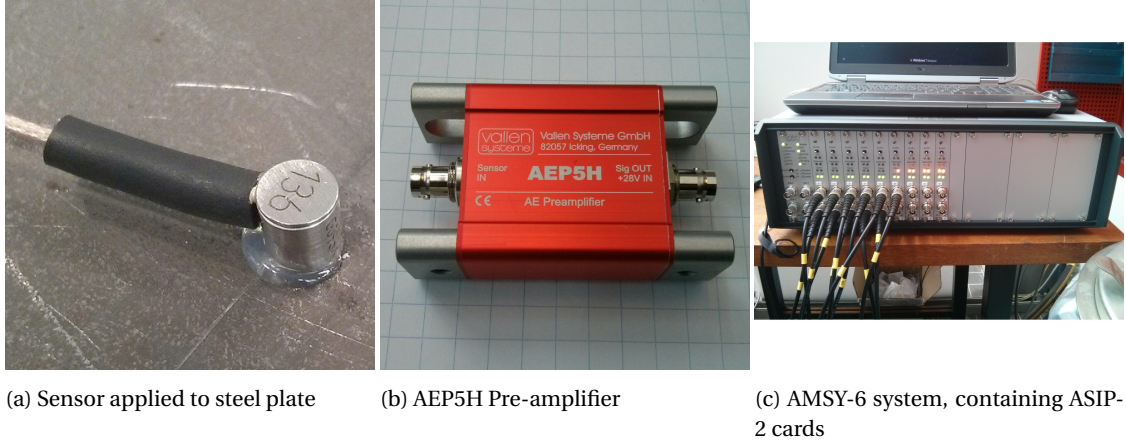
Figure 1.4: AE monitoring equipment

wave modes, divided between symmetric (S) and anti-symmetric (A) modes, which will be elaborated on in
Section 2.1. The most commonly observed wave modes are the first symmetric (S0) and first anti-symmetric
(A0) wave modes, which travel at approximate speeds of 5.5 mm/μs and 3.2 mm/μs, respectively. Figure 1.5
shows the symmetric (a) and antisymmetric (b) wave forms. The frequency range of AE waves are typically
in the range of 20 kHz–2000 kHz [22]. Section 2.1 will provide more detail on the encountered wave types
encountered during in this thesis.

1.2.4. ACOUSTIC EMISSION MONITORING EQUIPMENT

AE monitoring is used in several industries to detect different kinds of (un)wanted behavior in a system.
When the right setup is used, plastic deformation, tearing, fatigue crack growth, stress corrosion cracking
and valve leakage can be detected. This *right* setup depends on the applied sensors, amplifiers, filters and
acquisition settings. During this project the AMSY-6 system of Vallen Systeme GmbH will be used during the
experiments, with the sensors being of VS600-Z2 type. Information on the systems characteristics have been
obtained from official data sheets [25], [24], [23], or by means of communication with Vallen itself.

PIEZOELECTRIC SENSOR

The most common AE sensor type is the piezoelectric transducer. A piezoelectric material converts defor-
mation of its shape into an electric current. Figure 1.6 shows a sketch of a section cut of a typical AE sensor.
The sensor is attached to the plate using a coupling material. This coupling in necessary for the waves to be
transferred from the material to the sensor, since it provides acoustic contact. Often used coupling agents are
silicone grease and hot glue. When the former is used, the sensor needs to be attached to the object using
some sort of clamping, for which magnets can be used. This is unnecessary when hot glue is used, since this
couplant provides adhesion itself.

    The sensor is attached to the surface of the plate, so deformation of the piezoelectric element is done by
out-of-plane motion. Wave forms of pure in-plane nature would not be sensed by this type of transducer.
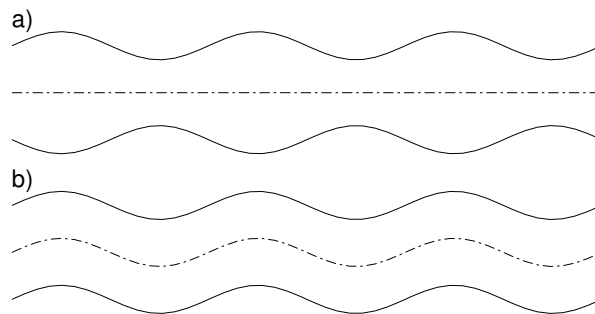
Figure 1.5: Lamb waves   Figure 1.6: Section view of a piezoelectric sensor
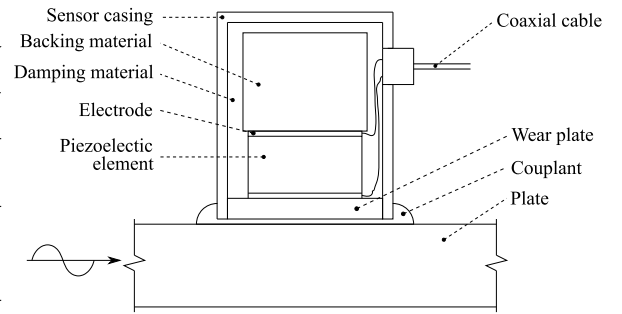
Apart from the damping material which surrounds the piezoelectric element, sometimes a more rigid material is used as backing for the sensing element, in order to influence the modal properties, and thus the sensor response.

The sensors which will be used during the recordings in this thesis are VS600-Z2 sensors (datasheet given in Appendix D [25]). This is a sensor that resonates at 600 kHz and has an diameter of 4.75 mm. Figure 1.4a shows one of these sensors which is attached to a steel plate by hot glue.

PRE-AMPLIFIER
The signal which is produced by the sensor is of very low voltage, which makes it unable to travel great distances without significant loss of energy. To circumvent this, the signal needs to be amplified. An analog pre-amplifier often is embedded into a sensor itself, but in the case of the VS600-Z2 sensors, an external pre-amplifier is used, since the sensor itself is too small to contain one. Some filtering is done in the pre-amplifier in order to prevent disturbance in the signal.

The pre-amplifier used by the 4D-Fatigue JIP is AEP5H pre-amplifier, which outputs a signal at 28 V, and accommodates a gain of 34 dB or 40 dB. An AEP5H module is shown in Figure 1.4b, its datasheet is given in Appendix D.

ASIP-2
The ASIP-2 is a signal processing card which contains two recording channels. This module performs several steps in the signal manipulation.

Analog filter   The analog filter in the ASIP-2 unit is mostly in place to prevent aliasing during the ADC step, but also filters out low frequency noise. Aliasing occurs when a signal is sampled with a insufficient sampling rate. High frequency waves become indistinguishable from certain low frequency waves.

ADC   The analog to digital converter converts the analog signal to a 16 bit digital signal with a sampling rate of 40 MHz.

FIR filter   A digital filter is in place to reduce the ADC noise. This is a 18bit, 27 taps (26th order) lowpass, finite impulse response, linear phase filter with a cutoff frequency of 3.6 MHz.

Application specific filter   The application specific filter is arguably the most important filter because it has the narrowest passband. When using a sampling rate of 40 mega samples per second (MSPS), the highpass filter can be set to bypass and 100 kHz, the lowpass filter can be set to bypass, 1000 kHz, 1800 kHz and 2000 kHz. The application specific filters at 40 MSPS are fourth order infinite impulse response (IIR) Butterworth filters. Experience learns that the most convenient filter to use is the 100 kHz–1000 kHz filter.

1.2.5. ACQUISITION
AMSY-6   For the actual acquisition of AE signals, the AMSY-6 system is used. In the case of the 4D-Fatigue JIP, the system contains nine ASIP-2 cards, totalling eighteen recording channels. The AMSY-6 system *collects* te signals from the channels, and provides an interface for communication with a personal computer.

Sampling rate   The highest sampling rate supported by the system is 40 MSPS. Lower sampling rates are also supported, in order to obtain signals of smaller data size, which can be beneficial during long term monitoring. All the signals in this report have been acquired with the highest sampling rate, in order to obtain as much information as possible.

Hits and events   When one individual sensor picks up a signal, this is referred to as a *hit*. When multiple hits are detected on different sensors and in a short time interval, they can be grouped together in an *event*. If an event contains enough hits, localization of the event can be attempted. Based on the determined location, wave form and frequency components of the signals, a prognosis can be formed on the source type.

Threshold based vs. continuous monitoring   During AE monitoring, a choice must be made between threshold based and continuous monitoring. Threshold based hit registration works as follows. The output signal of all recording channels is monitored. As long as the amplitude of the signal remains below a user specified value, it is considered to be background noise, and is not recorded. When the amplitude crosses the threshold value, the signal is recorded until the amplitude has decreased below the threshold for a certain specified duration. A user specified length of signal preceding the threshold crossing is also recorded. Figure 1.7 shows an example of an AE wave, which crosses the threshold at $t \approx 5$. The signal preceding the first threshold crossing is recorded from a buffer. The last threshold crossing is at $t \approx 36$, and the recording ends at $t = 50\mu s$.

During continuous monitoring, all data received from the channels is recorded. This way, a more sophisticated method of hit discrimination can be used, enabling the user to obtain more useful data. A downside, however, is the large amount of data storage that has to be available. Fatigue tests typically take multiple days, magnifying the need for data storage. Threshold based recording is deemed satisfactory during the current research.

Measuring range   The maximum voltage magnitude that can be measured by the used equipment is 100 mV. In a low noise environment, the noise might range from 0.01 mV to 0.1 mV. Since these values are of different scales of magnitude, it is convenient to use a logarithmic scale. The decibel scale is used:

$$A[\text{dB}] = 20\log\left(\frac{U_{\text{out}}}{U_{\text{in}}}\right) \tag{1.1}$$

When talking about sound levels in decibel, often a reference value $U_{\text{in}} = 1\,\text{V}$, or $U_{\text{in}} = 2 \cdot 10^{-5}\text{Pa}$ for acoustics, is used. Due to the low voltages in AE, another reference value of $U_{\text{in}} = 1\,\text{mV}$ is used. When working with this dB$_{AE}$ scale, an increase of 6 dB is equal to multiplication of the voltage with a factor 2.

1.2.6. LOCALIZATION

In most cases of AE monitoring, the goal is to establish a certain phenomenon, e.g. fatigue crack growth, is occurring, and the location it occurs. This section will provide an introduction to the localization of AE sources.

Multilateration   Localization of an AE source is done by multilateration. This is a technique that uses the differences in arrival times of a single wave at multiple sensors. It is also used to find the epicentre of seismic activity. The method works as follows. When two sensors with known locations pick up a wave, a time of arrival (TOA) is registered for both of them. With the difference in arrival time and the wave travel speed, which should also be determined, a difference in traveled distance can be determined for the waves at both sensors. This difference in traveled distance, or *range* difference, can be used to determine an infinite number of possible source locations. In a two dimensional case, these locations would be in the shape of a hyperbole. Figure 1.8 shows an example of such an hyperbole. Sources on each location on the hyperbole, result in exactly the same time difference of arrival (TDOA) value for the sensors applied. When another sensor is added, with which another hyperbole of possible locations can be formed, the actual source location can be found on the intersection of the two lines.

Wave speed determination   In order to determine the wave speed to be used for localization, conventionally two methods are used.

When two sensors are placed on the specimen in a straight line, a PLB is performed in line with these sensors. Since the travel distance and the time it takes for the waves to cross this distance are known, the travel speed can be calculated. Mostly the speed of symmetric or anti-symmetric Lamb waves are determined, which are dependent on the frequency of the waves.

Another way of speed determination can be used when the location of the defect is known. Two sensors are placed in a straight propagation line from the source. The travel speed can now be determined in the same way as described for the previous method. In this case however, the propagation speed for each specific event can be determined.

Accuracy   During classical use of AE monitoring, when a bridge section or pressure vessel is monitored for fatigue crack growth or other failure mechanisms, the actual detection of the failure mechanism is a goal
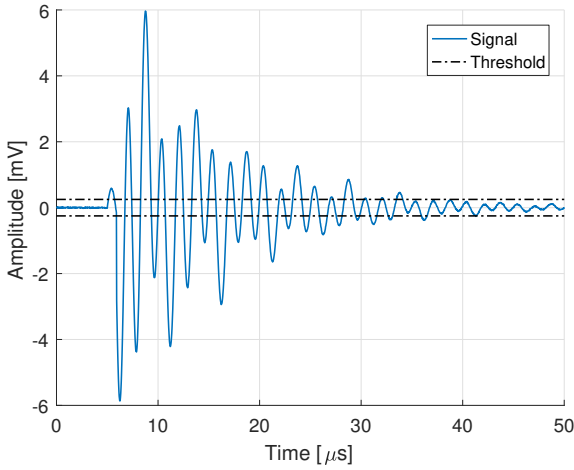
Figure 1.7: AE signal
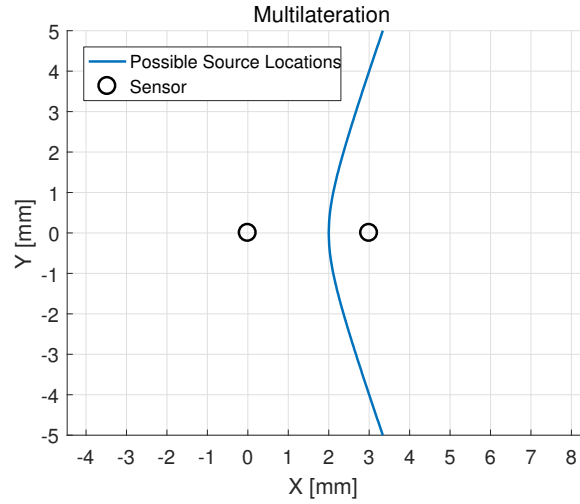
Figure 1.8: Localization results for multilateration using two sensors

on itself. Depending on the used sensor spacing and specimen geometry, location accuracy in the order of magnitude of several centimetres is the best result which is possibly achievable. For the intended purpose this often is sufficient. The global location of damage is then known, so remedial actions can be performed or other means of investigation can be applied.

Time picking   The determination of the TOA of a signals is referred to as *time picking*. A study [20] on improvement of the localization accuracy determined time picking to be a major influence in this respect. Traditionally the TOA is defined by the first threshold crossing, as stated in Section 1.2.5. Section 2.3.2 will elaborate on potentially more accurate time picking methods.

1.2.7. GROWTH RATE MONITORING
Aside from AE monitoring, there are other, more conventional, ways of determining crack depth.

Digital image correlation   One of these methods uses digital image correlation (DIC) to determine the opening displacement of the crack. Using a fracture mechanics model, this displacement can be linked to a certain crack depth.

Striation   Another method consists of the post mortem investigation of the crack surface. After a specimen has failed due to fatigue, often the crack surfaces contain striations. These striations are formed during the crack growth steps, and in some cases can be linked to individual loading cycles. Since the load history is known, the crack growth rate can be determined by measuring the distance between the striation marks.

1.3. PROBLEM STATEMENT
Multi-axial fatigue is a phenomenon which is not fully understood yet. Multiple damage prediction methods have been proposed, yet there is no consensus which method most accurately predicts the lifetime of a structure. In order to further investigate the multi-axial fatigue phenomenon, experiments will be carried out using a dedicated multi-axial fatigue testing machine. However, due to the multi-axial nature of the loading, conventional methods of determining crack growth rates are impeded. When a specimen is loaded in both bending en torsion, the crack surface will be polished, making investigation of striation impossible. DIC and CMOD investigation methods during multi-axial loading are also less straightforward compared to an uni-axial load case.

   Acoustic emission, among other methods, has been selected as a potential means of determining the crack depth during the fatigue testing. This is however a highly unconventional application of AE monitoring, since the intended location accuracy far outreaches all current applications. The minimal location accuracy,

defined by the 4D-Fatigue JIP, states that the crack front depth must be able to be predicted with an error less than a millimetre. The final goal in this respect is an error of less than 0.1 mm.

To achieve this level of accuracy, sensors will be located very close to the initial defect. This also in uncommon in the field of AE monitoring, since the location of the defect generally is not known. Interaction of the stress waves with the crack surface will play a bigger role at such close proximity, which is something that is not of interest during regular AE monitoring.

The theoretical propagation speeds through the body of the specimen are known. If these waves are able to be recorded, localization accuracy will be very high. In practical situations however, environmental noise will prevent accurate pinpointing of the absolute first arrival of these waves. The fact that the specimen will be loaded in a hydraulic machine, will increase the noise level to a yet unknown noise level. Practical TOA values will therefore not be able to be based on the speeds of the longitudinal or transverse wave speeds, but rather on the speeds at which a certain signal characteristic travels, e.g. a threshold crossing. Travel speeds of such characteristics are not constant, and are less predictable, since they are dependent on specimen geometry, among other potential influences.

One of the intended specimens to be fatigue loaded during the 4D-Fatigue JIP is the TS. Crack growth in the weld toe is investigated. The fact that the AE is produced in such close proximity of complex geometry, has the effect that waves will be reflected by it. These reflections might pose a risk for an accurate crack front localization, since they might influence the TOA determination.

Simulations of AE can help determining the potential accuracy of crack front localization. In this thesis finite element (FE) modeling will be used to achieve this, as well as determine the behaviour of the AE waves. Literature does describe simulation of AE, but most literature sources focus on much greater sensor distances, since this relates more to common practical use. The great decrease in sensor distances might be accompanied by different requirements for the model.

1.4. THESIS OBJECTIVE

The goal of this thesis is to use the FE method to gain knowledge on the behaviour of acoustic emission in close proximity to its source mechanism, in order to determine factors which influence the localization accuracy. In this case *behaviour* encompasses the following topics.

- **Wave types in close proximity.** Since the sensors will be located very close to the fatigue crack, Lamb waves will not have developed yet. Other wave types on the other hand, will play a bigger role than usual, due to this close proximity.

- **Crack geometry and depth.** The geometry of the crack might influence the localization of the crack front, since waves may travel over the surface of the crack, potentially influencing the time picking. With increasing crack depth, this effect may vary.

- **Reflections.** Since the fatigue crack in the TS will be very close to a flange, inbound waves might be reflected by it, directing part of the wave energy back to the sensors. This effect might influence localization.

Realistic localization accuracy for a fatigue crack tip should be determined, with the above topics taken into account. It should be aimed to improve on this accuracy.

1.5. APPROACH

The finite element method has been chosen to investigate the behaviour of AE, since the problem is too complicated to be solved analytically.

The first step will be to obtain a reliable FE model which is adequate to simulate the generation and propagation of AE waves. The basis for this model will be several PLB's on a steel plate, at varying distances from the sensor. Appropriate element type, element size and time discretization will be investigated for relevant wave travel distances. Boundary conditions and the signal processing structure will be established, as well as a source model for PLB's.

The second step will be to obtain a source model for fatigue crack growth. An uni-axial fatigue test of a simple steel plate is performed in order to validate a source model, which is reproduced from existing literature sources. Conclusions on time picking, wave speeds and crack front localization accuracy will be drawn based on these simulations.

The obtained source model for fatigue crack growth AE will be used in a simulation of the tubular specimen. Here the effect of the flange will be investigated. The crack front localization methods will also be investigated with the tubular specimen geometry.

1.6. THESIS OUTLINE

The chapters in this thesis encompass the following topics:

Chapter 2: Theory and Background   Theory on several major topics in this thesis will be given. These topics include AE monitoring in general, waves in solid bodies, signal processing and localization by multilateration. Simulation of AE by several literature sources is also reviewed.

Chapter 3: Software and Methods   Used software and analysis methods are described, as well as the criteria to which the simulated signals will be tested. This includes the finite element simulation of the AE waves, and simulation of the AE monitoring equipment.

Chapter 4: Simulation of Pencil Lead Break   This chapter describes the process and results of PLB simulation. The main goal of this chapter is the verification of the simulation method, including the sensor response simulation. PLB's are easy to perform, making it a convenient first step in the simulation process. The simulated signals have been successfully verified by experimentally obtained signals.

Chapter 5: Simulation of Fatigue Crack Growth   The next step is the simulation of actual fatigue growth, in order to investigate the accuracy with which the crack depth can be located. Fatigue experiments were performed, which did not result in useful signals to verify the fatigue sources. The simulation of AE from fatigue crack growth is based on three AE source models, which are found in literature sources. Localization of the crack front was performed with an accuracy of 0.5 mm.

Chapter 6: Influence of Local Geometry   One of the intended specimens for multi-axial fatigue testing is a tubular member containing a flange. A potential risk is that reflections of this flange will impede the crack front localization feasibility. This risk is investigated, after which it can be concluded that the reflections are of low importance. Crack front localization is determined to be possible with an accuracy of 1 mm. The decrease in accuracy with respect to the simple plate is due to the increased thickness of the body.

2

THEORY AND BACKGROUND

This chapter will provide theory and background information on several components of the system during AE monitoring. Basic theory on waves in solid bodies, signal processing and AE source localization will be provided. Literature on simulation of acoustic emission will also be reviewed.

2.1. WAVES IN SOLID BODIES

This section will provide a description of relevant theory on waves is solid bodies.

2.1.1. WAVE TYPES

Waves in solid bodies tend to be more complicated than waves in fluids. This is due to the fact that the former, apart from elasticity of their volume, also have elasticity of their shape. After an applied force has been removed, fluids will restore to their original volume and pressure. Solids like steel however, unless stressed too high, will additionally return to their original shape. This is possible because steel has both longitudinal and transverse elasticity.

Two main wave types can be identified, namely longitudinal and transverse waves. Respectively, these are pressure and shear waves. Longitudinal waves posses an oscillation in the travel direction of the wave, while transverse waves oscillate in the direction perpendicular to the travel direction. Longitudinal and transverse waves are visualized in Figure 2.1a and b respectively.

Wave speeds of longitudinal (c_L) and transverse waves (c_T) are dependent on material properties, and are given in Equations (2.1) and (2.2) respectively, in which E is the elasticity modulus, ρ the mass density and ν Poisson's ratio.

$$c_L = \sqrt{\frac{E(1-\nu)}{\rho(1+\nu)(1-2\nu)}} \tag{2.1}$$

$$c_T = \sqrt{\frac{E}{2\rho(1+\nu)}} \tag{2.2}$$
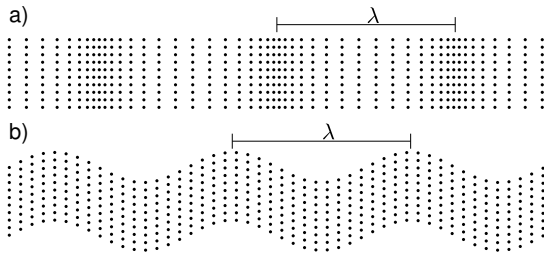
Figure 2.1: Longitudional (a) and transverse (b) wave displacements
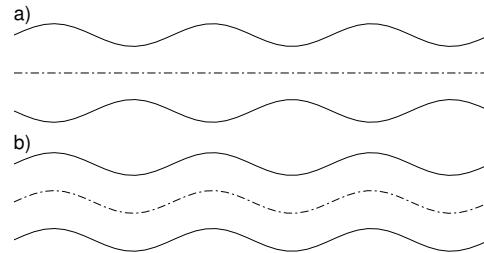
Figure 2.2: Symmetric (a) and anti-symmetric (b) lamb waves

11

When typical material properties of steel ($E = 210\,\text{GPa}$, $\rho = 7800\,\text{kg/m}^3$ and $v = 0.287$) are used, the wave speeds in Equations (2.3) and (2.4) can be calculated.

$$c_L \approx 5.9\,\text{mm/μs} \tag{2.3}$$

$$c_T \approx 3.2\,\text{mm/μs} \tag{2.4}$$

Some special types of waves in solids will be discussed in this section.

Rayleigh waves   One of the waves that are formed by a combination of longitudinal and transverse waves is the *Rayleigh* wave, or *Rayleigh surface* wave. This type of wave is present in bodies which contain a free surface, and are not unlike ocean waves. The magnitude of oscillations decreases when observing nodes further away from the surface. The velocity of a Rayleigh surface wave is approximated by $c_S \approx 0.93 \cdot c_T$ [11].

Lamb waves   Another type of wave is the *Lamb* wave, or *plate* wave, which forms in thin solid media with two free surfaces, as the latter name suggests. Lamb waves are named after sir Horace Lamb, who published his analysis on waves in solid plates in 1917. Due to the complexity of the waves, not much attention was drawn to his work until 1945, after which the waves became slowly better understood. In the 1980´s the use of lamb waves became popular in engineering applications, partly due to the advances in computing devices [21]. Nowadays Lamb waves are of great interest for non destructive testing purposes, because of their great travel distance, and dominance in thin walled structures like pressure vessels.

There are two forms of Lamb waves, namely the symmetric and anti-symmetric form, visualized in 2.2 a and b, respectively. Without digging too far in the theory behind Lamb waves, the wave equations for symmetric and anti-symmetric waves are given in Equations (2.5) and (2.6) [21]. Both Lamb wave types have an infinite amount of modes, which are generally not analytically determinable, but are found through numerical iteration. Figure 2.3a and 2.3b show a typical graph of phase and group velocities respectively, over a range of frequencies. Only the first symmetric (S_0) and first two anti-symmetric (A_0 and A_1) are shown in the graph, these are the waves most likely to be distinguishable. The group velocities are obtained using Equation (2.7) [21].

$$\frac{\tan(qh)}{\tan(ph)} = \frac{4k^2 qp}{\left(k^2 - q^2\right)^2} \tag{2.5}$$

$$\frac{\tan(qh)}{\tan(ph)} = \frac{\left(k^2 - q^2\right)^2}{4k^2 qp} \tag{2.6}$$

$$c_g(f \cdot 2h) = c_p^2 \left(c_p - (f \cdot 2h) \frac{dc_p}{d(f \cdot 2h)} \right)^{-1} \tag{2.7}$$

With:

$$p^2 = \frac{\omega^2}{c_L^2} - k^2 \tag{2.8}$$

$$q^2 = \frac{\omega^2}{c_T^2} - k^2 \tag{2.9}$$

$$k = \frac{2\pi}{\lambda_{wave}} \tag{2.10}$$

$$\tag{2.11}$$

Variable k is the wave number, ω the angular velocity, h half of the plate thickness, and λ_{wave} the wave length. As has been mentioned, Lamb waves are used widespread in NDT, and more specifically AE monitoring. However, most AE applications are focused on detecting defects further away from the sensor than is the case during the current research, in which the most likely sensor distance will be in the range of $5\,\text{mm} < s < 15\,\text{mm}$, in structures with plate thicknesses of $5\,\text{mm} < t < 10\,\text{mm}$. Literature reports that Lamb waves are not fully developed until at least a distance equal to four times the plate thickness has been traveled [11].
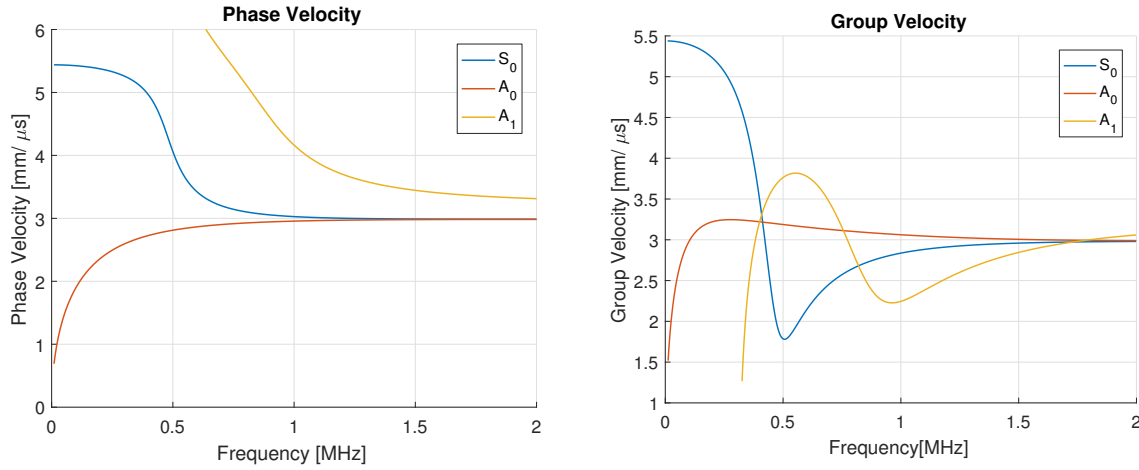
(a) Lamb wave phase velocities

(b) Lamb wave group velocities

Figure 2.3: Phase and group velocities of S_0, A_0 and A_1 lamb wave modes
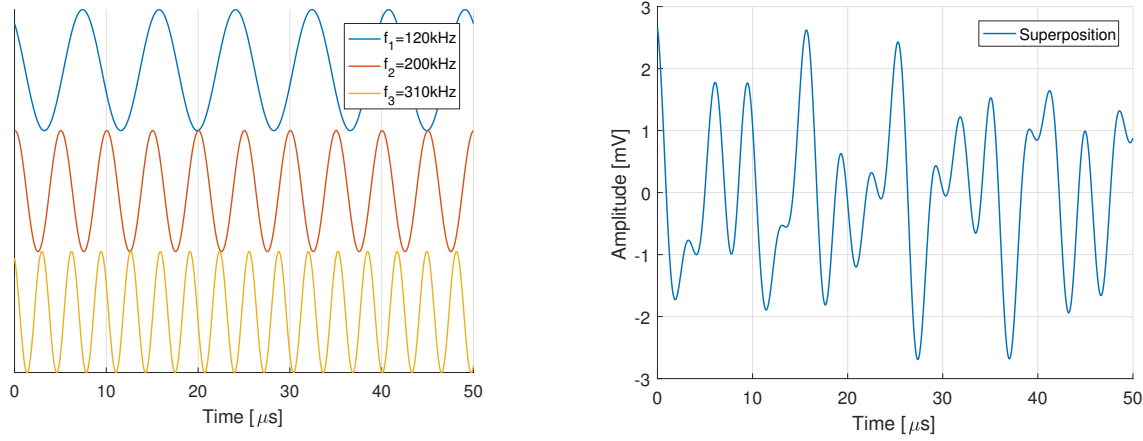
(a) Individual waves

(b) Superposition of individual waves

Figure 2.4: Wave superposition

Head Waves   A third relevant wave type is the *head*, also called *creeping*, wave [11]. This is a wave that travels over a free surface of the body with a speed of a longitudinal wave. Along its travel path, it excites a transverse wave into the body, with an angle of $\phi_t = \arcsin(^{c_T}/_{c_L})$ [11] with the free surface. Due to this property, the head wave itself attenuates quickly. Due to the small sensor distances used in this thesis, head waves are expected to be observed.

2.1.2. WAVE DEVELOPMENT

Several wave types have been discussed, which all occur in the specimen body. The way these waves form the single wave which can be observed by a sensor, is by the principle of superposition. For instance, when the three waves in Figure 2.4a are superposed, they form the wave in Figure 2.4b. By the naked eye, the individual waves are now unrecognizable, but they are still present and behave according to their own properties.

In the previous section it was found that waves of different frequencies, travel at different velocities. For Lamb waves this was visualized in Figure 2.3. Longitudinal and transverse waves also travel at vastly different speeds, as do Rayleigh and head waves. As result of this, wave properties, like the speed and amplitude of a certain peak, do not always travel at constant speeds. This has a negative effect on the accuracy of localization of the source, as this is based on the constant travel speed of certain signal characteristics, which will be made clear in Section 2.3.
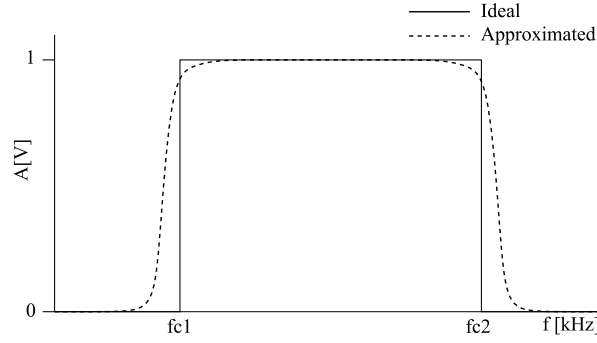
Figure 2.5: Ideal and approximated bandpass filter

2.2. SIGNAL PROCESSING

When waves are picked up by the sensors, the next step is for the AE monitoring equipment to sort out the good from the bad signals. An important part in this, is filtering out waves outside the relevant frequency range. Before the simulation of AE equipment will be described in section 3.3.2, some aspects of filter theory will be summarized here.

In signal processing, filters are used to manipulate a signal in such a way that certain frequencies are attenuated. The ideal filter completely attenuates the frequencies in the stopband, while both the phase and amplitude of the frequencies in the passband remain unchanged. In reality such a filter does not exist, so concessions must be made. In Figure 2.5 an ideal bandpass filter is shown, along with an example of it's approximation by what could be an actual existing filter. In the case of the physical filter, the transition at the cut-off frequencies is gradual. Inside the passband slight attenuation occurs. Different filter designs will approximate the ideal filter in their own way, prioritizing other characteristics of it.

The Butterworth filter design for instance, has a flat amplitude response in the passband. It has a monotonic roll off, meaning there are no ripples in the response. The phase response of the Butterworth filter is very good, with slight delays in the passband. Chebychev filters on the other hand, values the roll-off rate, which is higher than that of the Butterworth filter. A trade off with Chebychev filters is that there are ripples in either the passband or the stopband, and there is a bigger phase shift.

A filters characteristics are often assessed in the frequency domain. The frequency domain behavior is defined with its transfer function. This transfer function is the ratio of the Laplace transforms of the output and input signals of the filter.

$$H(s) = \frac{V_{OUT}(s)}{V_{IN}(s)} \tag{2.12}$$

In digital filtering a distinction can be made between infinite impulse response (IIR) and finite impulse response (FIR) filters. Transfer functions of the former contain components in both the numerator and the denominator, while the latter only has components in the numerator. Although FIR filters are more versatile in their frequency response, they generally need a higher filter order to achieve the same gain or attenuation rates, compared to their IIR counterparts. This makes them more expensive in analog filters, which consist of actual hardware components. They are popular in digital appliances however. FIR filters often have a constant phase shift.

2.3. LOCALIZATION OF AE SOURCES

When multiple sensors record signals of the same event, its origin in space and time can be determined. This is done by multilateration, which makes use of the time difference of arrival (TDOA) between signals and the travel speed of the wave. The following is based on [20].

The location of the AE source (S) and receivers (R) are denoted as:

$$S = (x, y, z) \in \mathbb{R}^3 \tag{2.13}$$

$$R = (x, y, z) \in \mathbb{R}^3 \tag{2.14}$$

The travel distance, or *range*, between the AE source and a receiver can now be calculated:

$$r = ||S - R|| \tag{2.15}$$

With $||...||$ being the Euclidean norm, calculating the vector length. The following equation shows the relation between the time of arrival and the time of the event:

$$t_{ai} = t_0 + \frac{r_i}{c} \tag{2.16}$$

With c denoting the wave travel speed, t_0 the time the waves were created, and t_{ai} the recorded arrival time at sensor i. For a three dimensional case, four unknown variables are present in this system, namely the three source coordinates and t_0, resulting in the need for four recorded arrival times.

It is more convenient to rewrite these equations in terms of TDOA, removing the t_0 term:

$$\delta t_{i,j} = t_i - t_j = \frac{r_i - r_j}{c} \tag{2.17}$$

Indices i and j refer to individual sensors. Using this, a range difference can be calculated:

$$\Delta_{i,j} = c(\delta t_{i,j}) = r_j - r_i \tag{2.18}$$

Example   Figure 2.6a is used to demonstrate this principle for a two dimensional situation. Sensor locations R_1 and R_2, as well as a source location S_1 and wave travel speed c values are:

$$R_1 = (0,0)\,\text{mm}$$
$$R_2 = (3,0)\,\text{mm}$$
$$S_1 = (2,0)\,\text{mm}$$
$$c = 1\,\text{mm/s}$$

For this case it is easy to calculate arrival times and TDOA using Equations (2.16) and (2.17):

$$t_{a1} = 2\,\text{s}$$
$$t_{a2} = 1\,\text{s}$$
$$\delta t_{1,2} = t_{a1} - t_{a2} = 1\,\text{s}$$

(a) Source at (x,y)=(2,0)mm   (b) Source at (x,y)=(-4,3)mm
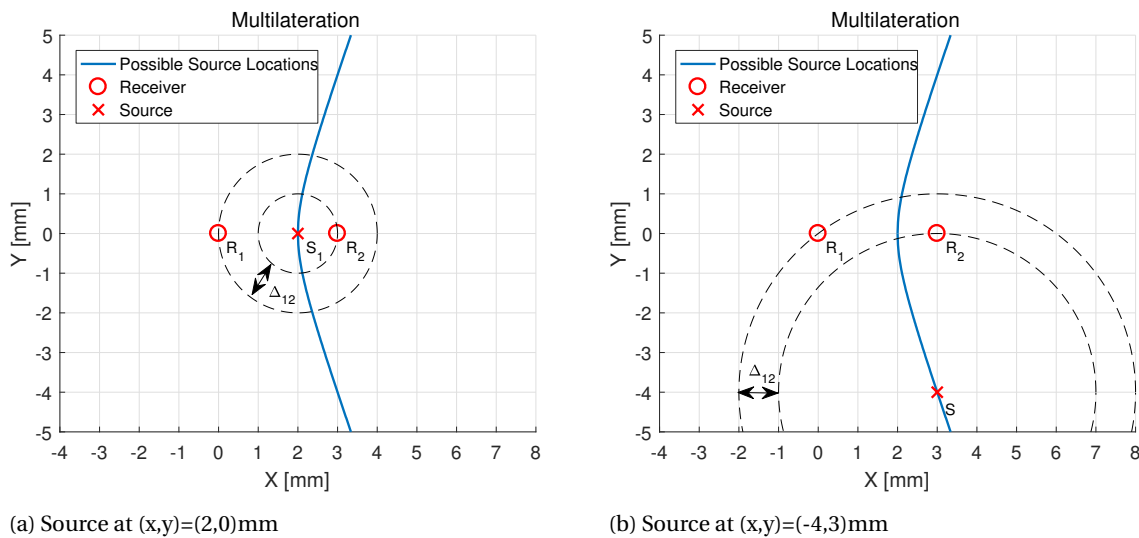
Figure 2.6: Localization results for multilateration using two sensors

Equation (2.18) now concludes on a range difference of:

$$\Delta_{1,2} = 1\,\text{mm}$$

The blue line in Figure 2.6a depicts all possible source locations which satisfy the range difference for the case which has been described. This is visualized by Figure 2.6b, which shows the wave front radiation from a source location $S = (3, -4)$mm. Although the waves have travelled further than was previously the case, the range difference is exactly the same.

Adding another sensor to the example, would result in another range difference value, and thus another hyperbole at which the source can be located. By finding the intersection of the two lines, the source location is found. It should be noted that with the addition of a third sensor, actually two extra TDOA values can be calculated ($\delta_{1,3}$ and $\delta_{2,3}$). However, with the addition of only one extra TOA, the second TDOA would result in redundant information.

The described example could also be extended to a three dimensional case. Two sensors would lead to a hyperbolic sheet of possible locations, and a minimum of four sensors would be necessary to obtain a single source location.

2.3.1. LOCATION UNCERTAINTY

The localization of an event using a perfectly accurate set of arrival times and sensor locations can be done using a simple Linear Least Squares Solver, albeit at the cost of an extra extra sensor and arrival time, in order to linearize the system of equations. The exact location of the AE source mechanism will be found. This however, will never be the case, since small errors in both parameters will always be present.

To determine the most likely source location, Vallen uses a location uncertainty (LUCY) parameter. This parameter compares the measured TDOA's and their likeliness to have originated from a certain point in space. Multiple points in space are evaluated, resulting in the most likely source location at the point with the lowest LUCY value. The LUCY value is determined by Equation (2.19):

$$\text{LUCY} = \sqrt{\frac{\sum\limits_{n=2}^{N} (\Delta_{1n}^{e} - \Delta_{1n}^{m})^2}{N-1}} \tag{2.19}$$

In which the Δ values refer to the range differences, calculated in Equation (2.18). The indices 1 and n refer to the sensor used in it. Superscripts e and m refer to the estimated data and measured data, respectively. N is the total number of sensors which are used in the localization.

2.3.2. TIME PICKING

The determination of signal arrival times has a major influence on the localization accuracy. This is actually less straightforward than it might seem, since each signal is different. This introduces the need to determine a certain feature of the wave to be used for TOA definition. One common method to determine the TOA, is to set an amplitude threshold, and register the time of the first sample that crosses this amplitude value. This method however, is dependent on the amplitude of the signal at a certain sensor, which is influenced by the sensor distance and the way the sensor is attached to the specimen, both of which can vary between sensors. Other methods could be the time of a first peak after the threshold crossing, or the time of the maximum signal amplitude (MA). These time picking methods have been visualized in Figure 2.7.

In [20] an investigation was performed on several alternative time picking methods, with the aim to find a method which results in higher accuracy of hit localization. The two most promising methods are using the time of the minimum Hinkley criterion (HC) and minimum Akaike information criterion (AIC) values over time. The HC function takes the sum of the energy in a time window up to a certain sample, and compares it to the mean energy in the total length of the signal. The AIC function compares the variance of the signal before a certain sample with the variance of the signal after it.

The HC and AIC values of a certain sample in a signal are calculated using Equation (2.20) and Equation (2.21), respectively.
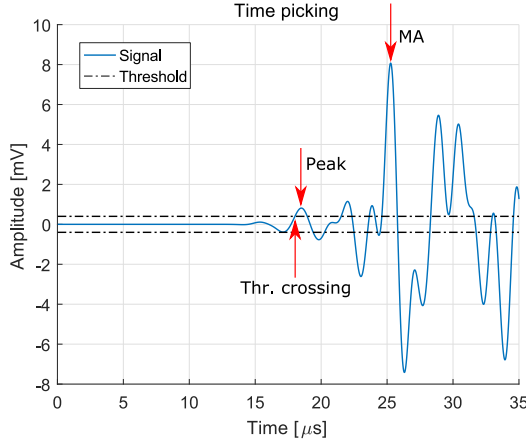
Figure 2.7: Time picking criteria
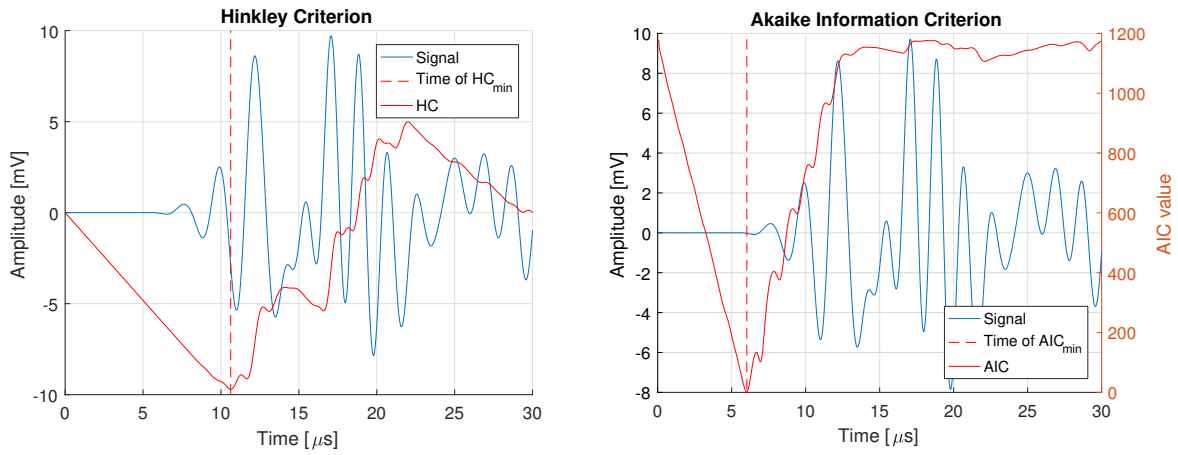
(a) Hinkley criterion

(b) Akaike information criterion

Figure 2.8: Time picking functions

$$\mathrm{HC}_n = \sum_{m=1}^{n} U_m^2 - \frac{n \sum\limits_{m=1}^{N} U_m^2}{\alpha N} \tag{2.20}$$

$$\mathrm{AIC}_n = n \log_{10}(\mathrm{Var}[U_{n-}]) + (N - n - 1)\log_{10}(\mathrm{Var}[U_{n+}]) \tag{2.21}$$

In which N is the total number of samples in a signal, U is the value of a sample, α is a scaling factor, which is set to 1. n indicates a certain sample, while $n-$ and $n+$ indicate all the sample before and all the samples after n, respectively. Figure 2.8 shows the HC and AIC values calculated for a signal, and the picked arrival time.

Another time picking option is based on work of Baer & Kradolfer (BK), evaluating the energy in a signal. The BK function is given in Equation (2.23) [20].

$$e_n^2 = U_n^2 + \dot{U}_n^2 \frac{\sum\limits_{m=1}^{n} U_m^2}{\sum\limits_{m=1}^{n} \dot{U}_m^2} \tag{2.22}$$

$$\mathrm{BK}_n = \frac{e_n^4 - \overline{e_{n-}^4}}{\mathrm{Var}[e_{n-}]} \tag{2.23}$$

2.4. LITERATURE ON SIMULATION OF ACOUSTIC EMISSION

Simulation of AE in both steel and carbon-fibre reinforced plastics (CFRP), using FEM, has been a subject of interest for several authors. As history progressed, finer discretization in both time and space, as well as more efficient algorithms and faster computers became available. This has made simulations more widespread available, and has raised the standard for them.

PLB simulation   In 1999, W. H. Prosser reported [13] on two-dimensional PLB simulations of a 3.125 mm aluminum plate. For these simulations the authors used a previously published DFEM code [8], which was suitable for the prediction of AE signals in plates. He used a through-thickness discretization of 130 elements near the source, decreasing to 5 elements when moving away from it. Time-steps ranged from 0.082 μs to 0.0033 μs, to satisfy the Courant-Friedrichs-Lewy (CFL) stability condition, to which a DFEM model must adhere. The CFL condition states that the time-step must be smaller than the time it takes for a wave to transverse a single element. Sensor output signals were obtained at 25.4 cm in [8] and 7.62 cm in [13]. Prosser studied not only the first pass of the wave, but also reflections from the plate edges, PLB's performed on the edge of the plate, and the existence of Rayleigh surface waves on the edge of the plate. The edge PLB's proved to contain more energy in symmetric Lamb waves, compared to regular PLB's on the plate surface. He attributed this to the fact that the source was directed in-plane. He stated that if it were physical possible to perform a PLB on the exact centre of the plate, this would eliminate the anti-symmetric waves. This was actually the case with his simulation, causing the need to introduce a slight asymmetrical component in the model. In his experiments, Prosser used sensors with a flat frequency response from 20 kHz–1 MHz and a fourth-order Bessel bandpass filter at 50 kHz–1 MHz.

R. Hill published a paper [10] on the simulation of PLB's in 2004, also simulating the sensor transducer using the FE method. The model consisted of a 25 mm plate with uniform mass density. Two-dimensional plane strain elements were used. Adhering to a maximum time interval of $t = (20 \cdot f_{max})^{-1}$ and a element length of $l_e = \lambda_{min} \cdot {}^1/_{20}$ to be able to model AE propagation. The used source model was an impulse force at several elements, located on, and directed perpendicular to the surface of the plate, with a duration of 2 μs. The sensor model was located at 20 cm from the source.

Fatigue crack growth simulation   Several papers [15–19] by Markus G. R. Sause report on simulation of AE in both metals and CFRP's, regarding both PLB's and crack growth. The earlier works use a dipole source model for fatigue crack growth, while in the more recent [19] he describes a new source function, to more accurately simulate how the waves interact with local geometry, such as matrix-fiber boundaries.

The dipole source, or *point* source, simply consists of two nodes being excited in opposite direction of each other, of which a representation is shown in Figure 2.9a. This is a simple representation of the nucleation of the material at a certain depth. Excitation times generally range from 0.1 μs to 2 μs. Several displacement functions $u(t)$ are suggested.

The *extended* source [19] is an extension on the dipole source. This source model uses the same principle, but the crack geometry is modelled in this case, and is used in [5, 6]. For a sketch, see Figure 2.9b.

The third investigated source is based on fracture mechanics, and will be referred to as *separation* source, of which a representation is shown in Figure 2.9c. This source model is not dependent on a certain excitation function, but on the stresses present in the model. A certain boundary condition is set in the crack surface, which releases nodal constraints at the moment the failure criteria of the material are met. The model is loaded up until the point of failure, after which the constraint is released. The crack surfaces will move away from each other due to the stresses present, generating the AE waves in the process.

(a) Dipole source   (b) Extended source   (c) Separation source
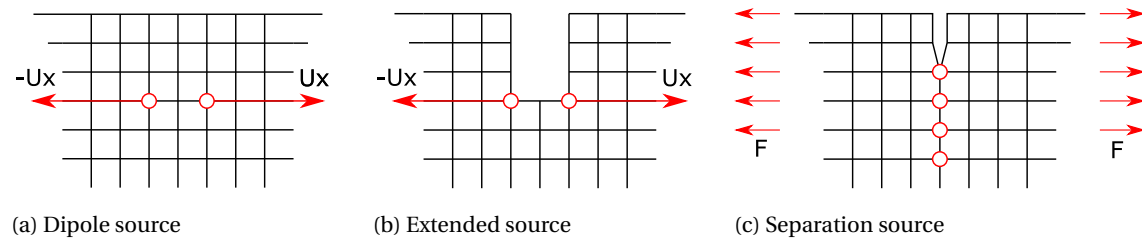
Figure 2.9: Fatigue AE source models in literature

3

SOFTWARE AND METHODS

The aim of this chapter is to shed light on working methods used in the following chapters. Criteria for convergence of the FE results and similarity of the simulation result with respect to the recorded signals are discussed. The simulation of the piezoelectric sensor response and signal processing will also be treated.

3.1. AXIS CONVENTION

In the following chapters the axis convention shown in Figure 3.1 will be used. The origin of the axes will mostly lie on the bottom of a plate, which is only not the case for the TS, at which the origin will lie on the axis of the tubular. The main propagation direction is along the y-axis, at which the travel direction is $\alpha = 0°$. PLB and fatigue sources will always be located at $(x, y) = (0, 0)$mm, at varying values for the z coordinate. When cracks are modelled, their growing direction is in the negative z direction for depth, and in both positive and negative x directions for length, although only the positive x direction will be modelled, due to symmetry boundary conditions.

3.2. FINITE ELEMENT METHOD

3.2.1. SOFTWARE

The FE software used for the calculations is Abaqus 6.13. This application features a graphic user interface, as well as script input. Two different solvers can be used in Abaqus, namely the explicit and implicit solver.

Explicit   The explicit solver uses central-difference time integration. This makes each increment relatively inexpensive in term of computational time, but increases the need for small elements. The stiffness matrix is updated after each time step. This method is accurate when the model has not changed too much during that time step. In the case of AE, the smallest element is the bottleneck for the length of the time step, since
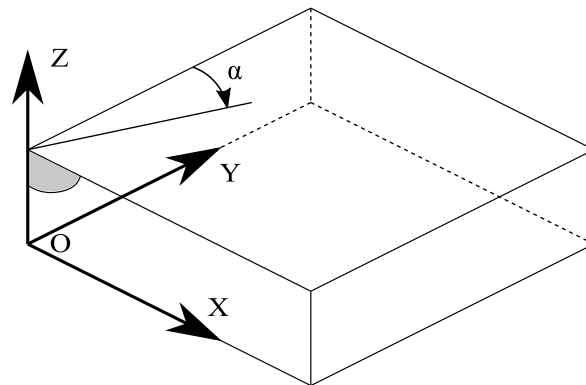
Figure 3.1: Axis convention

19
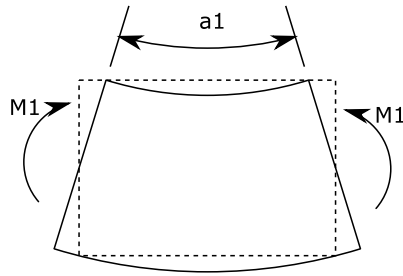
Figure 3.2: Beam bending
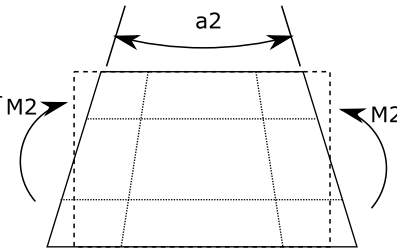
Figure 3.3: Bending of linear full integration element
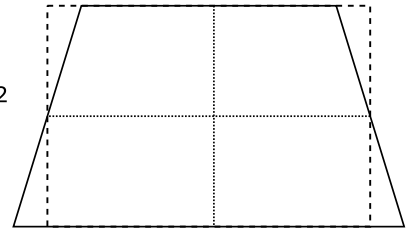
Figure 3.4: Zero energy mode in reduced integration element

the latter needs to be smaller than the time it takes for a wave to traverse it. When this condition is not met, the solution will become unstable, resulting in oscillating responses which increase rapidly in amplitude. The explicit solver generally is preferred when large models are used, with relatively short dynamic response times.

Implicit   The implicit solver uses direct integration, and is able to solve nonlinear dynamic problems. While bigger time steps are allowed with this solver, each incrementation takes a longer time to solve. The implicit solver performs Newton-Raphson iterations in order to enforce equilibrium between the internal and external forces. This increases computational effort, but allows for bigger time steps that the explicit solver. For static and nonlinear dynamic simulations the implicit solver is preferred [1].

3.2.2. SHEAR LOCKING AND HOURGLASS MODE

Generally two types of integration can be used for elements in a FE model. The first one is *full integration*, which, in the case of a linear hexagonal element, use $2 \times 2 \times 2$ Gaussian points for the integration scheme. Elements using the full integration method, however are computational very expensive. In the case of linear fully integrated elements, shear locking can occur, which makes the model far stiffer in bending, than it would be in reality. The second integration scheme is *reduced integration*, which uses a single Gauss point. Reduced integrated elements are far cheaper in computational sense, and are more flexible as shear locking cannot occur. This method however, also has its downside: it is prone to hourglassing.

Shear Locking   The phenomenon of shear locking is the inability of an element to accurately simulate bending deformation. It is best explained using Figures 3.2 and 3.3. A natural bending form in shown at the left. A representation of the same bending form by a linear four-noded 2D element is shown at the right. Note that in order to achieve this form, a shear stress is introduced. This leads to a greater required energy which is needed, increasing the bending stiffness.

Hourglass Mode   The hourglass mode is a non-physical, zero-energy mode that produces no stress or strain [1]. The phenomenon is visualized in Figure 3.4. The dashed line shows the deformed element, but the stress and strain in the element are still zero, since the dotted lines are still the same length, and the angle between them have not changed.

There are several methods to prevent hourglassing. Artificial stiffness or viscosity can be added to the element, preventing the formation of the unwanted mode. Care should be taken however, since this stiffness might also have an influence on the other deformation modes. Another option is the use of tetrahedron elements, although linear tetrahedron elements suffer from other stiffness related problems, and are often shunned [7]. A smaller mesh size also generally helps negating the hourglass mode. Whenever possible, point loads should be avoided, and replaced with a pressure on a surface.

Conclusion   To summarize, both fully integrated as reduced integration elements have their downsides. During the research in this thesis, emphasis will be on reduced integration elements, since the computational resources are a greatly limiting factor. The hourglass mode will be observed in the following chapters, but effort is made to prevent it as much as possible.
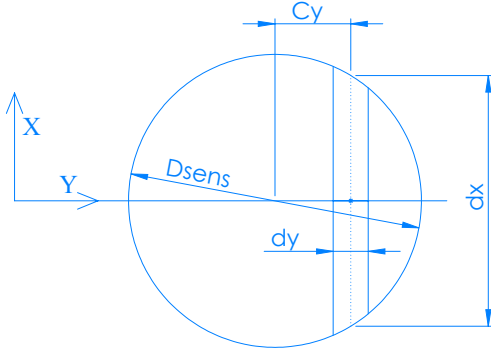
Figure 3.5: Straight line output

3.2.3. OUTPUT

The method to obtain signals from the FE simulation results is described here.

OUTPUT VARIABLE

The output of the simulation is in the form of nodal displacements in z direction, which is perpendicular to the plate surface. The fact that displacements are used instead of velocities or accelerations, is based on multiple literature sources mentioned in Section 2.4, which also use piezoelectric transducers in their experiments. This is not the case for all piezoelectric sensors, since [12] reports some sensors to be responding to acceleration rather than displacement. During this research, all three output options were investigated, which finally resulted in the best choice of displacement.

In FE modelling, a single node has an infinitely small geometry. In reality, a sensor will be excited by a larger area, so multiple nodes will be the basis of the output signal. This is contrary to the conclusions inl [9], which concluded that this is unnecessary for small sensors. In that paper however, the focus lay on sensors further away, so waves were more developed, and more spread out with regard to frequency, due to dispersion. Also the time picking accuracy was not as high a priority as currently is the case.

OUTPUT NODES

Two different methods will be used to extract time history data from the output nodes. The first is a lightweight method used during PLB simulations, in which the spreading waves are equal in all directions, while the second one is used during the fatigue simulations.

Single line output   A large number of simulations will be performed during the writing of this thesis. In order to keep the required storage limited, and to keep the processing time within bounds, not all nodes in the model produce a full history output of their displacements. Since the waves produced by a PLB are uniform in all travel directions, only the nodal displacements of nodes in a single straight line away from the source are recorded. To account for the fact that the sensor has a circular sensing area, thus picking up more energy in the middle node of this line, weight factors are assigned to each node. Suppose the schematic top view of the sensor in Figure 3.5. The weight factor f_{weight} is based on the sensor diameter D_{sens}, its location along the y dimension of the sensor (C_y), and the nodal distance (dy). Based on these variables, a fraction of the sensor area can be calculated, using Equation (3.1).

$$f_{weight} = dx \cdot dy = 2 \cdot dy \cdot \sqrt{\left(\frac{D_{sens}}{2}\right)^2 - \left(C_y\right)^2} \tag{3.1}$$

The z displacement along each node in the sensor area is multiplied by their respective weight factor. The mean sensor displacement can be calculated by obtaining the mean values of all the nodes.

Although this sensor is very accurate for greater sensor distances, it potentially lacks accuracy closer to the source. At greater distances, the waves front will arrive perpendicular to the sensor, which is also how the weight factor is calculated. Close to the source however, this might not be the case. For this reason, a more complete output method has been designed for the final PLB simulation and fatigue simulations.

(a) Nodes near crack in plane output   (b) Sensor surface in plane output
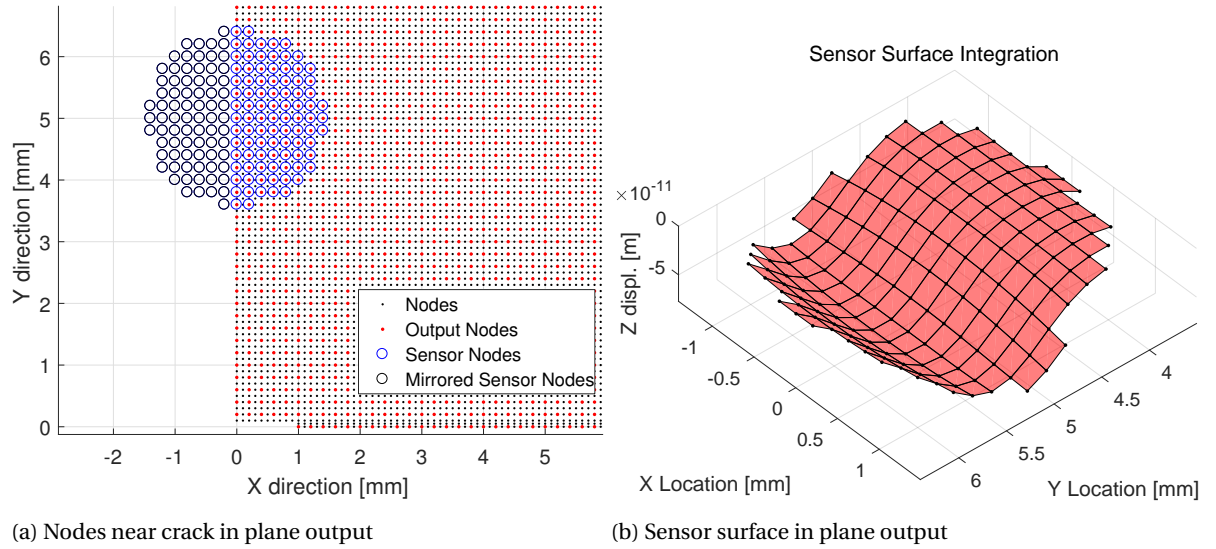
Figure 3.6: Finite Element Plane Output

Plane output   Apart from the fact that wave fronts do not arrive in a straight perpendicular line to their travel direction, wave spreading during fatigue crack growth also does not have the property of uniform wave spreading in all directions. This arises the need to have outputs in multiple directions, and an accurate representation of the sensor area.

Nodal outputs are generated for the top and bottom surface of the plate. To reduce the data size and handling time, not every node in these planes are used, but the nodes are selected in the form of a grid, close to the source location. The nodal locations and their history output are loaded in MATLAB, after which a virtual sensor location and diameter can be chosen. In between these nodes a surface is generated, the volume beneath this surface is determined, which will act as the output of the virtual sensor.

Figure 3.6a shows the location of all nodes on the top surface in close proximity of the AE source, which is located at $(x, y) = (0,0)$. The nodes which have been used to output their z displacement over time have been highlighted in red. The blue circles indicate the nodes that have been used to generate the sensor output. Since the sensor is located on the symmetry plane, some of the nodes have been mirrored in the yz plane. Figure 3.6 shows the generated plane at some moment in time. This volume beneath this surface is obtained through integration, and is divided by the sensor area, in order to obtain the mean displacement in z direction.

3.2.4. CONVERGENCE CRITERIA
In order to make sure that the discretization of the FE model in both time and space is done in a satisfactory manner, the convergence of the results must be investigated. The results of the FE simulations will be investigated in both the time and frequency domain. Sause et al. [16] propose a way to investigate convergence of two AE simulations by testing their coherence. Coherence is defined as

$$\eta_{xy}(f) = \frac{\left|P_{xy}(f)\right|^2}{P_{xx}(f) \cdot P_{yy}(f)} \tag{3.2}$$

P_{xy} being the cross power density spectrum of the two signals, while P_{xx} and P_{yy} are the power spectral densities of signals x and y, respectively.

Since time picking characteristics of the signal are of great importance during this research, another convergence criteria is selected, namely the arrival time of the first peak at a certain sensor distance. The amplitude of this peak will also be investigated.

3.3. SIMULATION OF SIGNAL PROCESSING
When the waves have been simulated using the FE method, these waves need to be converted to a signal, in the same way the AE equipment would. The way this is done, is described here.
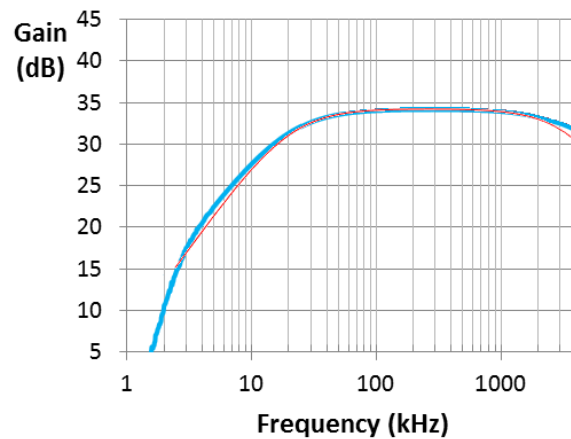
Figure 3.7: Pre-amplifier response in spec-sheet (thick blue line) and simulation (red line) [24]

3.3.1. MATLAB

MATLAB [2] will be used for signal processing and plotting of results. This software package is a powerful tool for matrix calculations. Its Signal Processing Toolbox provides multiple ways to analyze and manipulate signals in the time and frequency domain. Standard filter designs like Butterworth of Chebychev are readily available, as well as a filter designer, to create complicated multiband filters.

3.3.2. SIGNAL PROCESSING

Several signal processing steps are performed in the components of the AE equipment, as has been described in Section 1.2.4. The Abaqus output, having the same time intervals as the time integration in FEM, is first down sampled to a sampling frequency of 40 MHz, like will be the case with the recorded signals. Specifics on filters are, unless specified otherwise, taken from the equipment datasheet, given in Appendix D.

PRE-AMPLIFIER

The frequency response of the pre-amplifier specification is shown in figure 3.7, with the simulated pre-amplifier overlapped. Between 20 kHz and 2 MHz the replication is very similar. The simulated filter consists of a first order Butterworth bandpass filter, using 3dB cutoff frequencies at 20 kHz–3.4 MHz.

ANALOG FILTER

The 18 kHz–2.4 MHz analog anti-aliasing filter consists of a third order highpass, and a fifth order lowpass Butterworth filter. This filter will be simulated, using a digital filter with the same characteristics.

DIGITAL BANDPASS FILTER

The ASIP-2 unit features a large number of digital bandpass filter which can be chosen from in varying testing environments with different noise characteristics. When the highest sampling rate is chosen, this number is limited however. Experience dictates the 100 kHz–1000 kHz bandpass filter is very convenient, filtering out the low amplitude mechanical and high pass electrical noise, while maintaining engery in the right window for AE in steel.

3.3.3. SENSOR RESPONSE SIMULATION

The sensor that is used in this project has a big influence on the signal. Different from the signal processing filters, which are designed using electrical components, the frequency response of the sensor is dependent on it's physical properties. The response of the sensor is influenced by piezoelectric material, its geometrical properties and the backing material. Literature has reported on different sensors, responding to different properties of a wave, i.e. perpendicular displacement, velocity, acceleration, or in most cases a certain combination of these [12]. Successful studies have been performed that include a piezoelectric sensor in the FE simulation [10], [16]. However, finite element simulation of the VS600-Z2 sensor, and the verification of this model does not fit inside the scope of this thesis. During the simulations described in Chapter 4, it was found that the use of a certain filter in MATLAB, applied over the nodal displacement perpendicular to the plate

(a) VS600-Z2 Specification [25]   (b) VS600-Z2 Verification
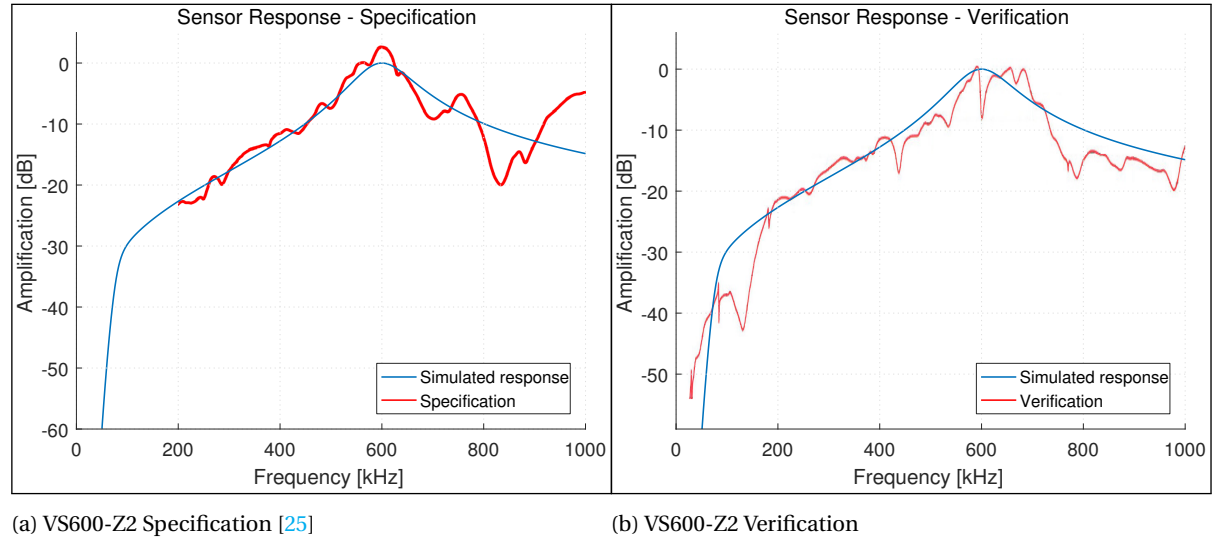
Figure 3.8: Sensor frequency response

surface, led to very good results. This filter, which simulated the sensor response, will be referred to as the *sensor response filter*.

SENSOR RESPONSE FILTER

Available data   The available data on the sensor response has been displayed in Figure 3.8. Figure 3.8a contains a graph of the frequency response supplied in the specification of the actual sensor (red), along the frequency response of the sensor response filter, which will be used throughout the following chapters. Figure 3.8b shows a comparison between the used filter, and the verification of a single sensor. This last verification graph has been supplied by Vallen GmbH, since the sensor response in the low frequency ranges (0 kHz to 200 kHz) was unavailable. It should however be noted that the sensor response of each sensor is somewhat different due to production tolerances, so the verification of a single sensor cannot be used a global way to determine the frequency response of all sensors. In this case it shows that the response of a sensor can deviate from the specification in a significant way.

IIR vs. FIR   The filter frequency response shown in Figure 3.8 is the result of a investigation between two filtering methods. First, a peaking IIR filter has been investigated. This is a filter that is available in MATLAB Signal Processing Toolbox. This is not a versatile filter, since just the location of the peak on the frequency axis, and the steepness of the slope can be determined. The shape of the of the sensor response however, does seem to globally match this form, apart from some fluctuations in the >600 kHz range, which can be seen in Figure 3.8a. To accommodate a steeper roll off rate at the lower end of the frequency response, an extra sixth order 80 kHz highpass Butterworth filter has been used.

The second type of filter that has been investigated is a FIR multiband filter. The MATLAB Signal Processing Toolbox accommodates an interface in which a filter can be designed, using specifying different attenuation rates at certain frequency intervals. Using this method, the sensor response can be recreated, including the fluctuations which are left out in the previously mentioned IIR filter solution. Although the frequency response of this filter can be tuned very precise, this cannot be said for the response in time domain, which in the case of this type of filter, proved to be unnatural.

The filter response of the IIR filter turned out to yield better results. Specifications have been given in Table 3.1. The phase response and derived group delay are shown in Figures 3.9 and 3.10 respectively. Significant delay is introduced by the sensor response filter, up to 110 samples, which relates to 2.75 µs. Since this delay is introduced for all signals, this will not have an effect on localization accuracy.

3.4. SIMILARITY CRITERIA

In order to verify the simulations, simulated signals need to be compared to the experimental recorded signals. To effectively do this, a way needs to be determined to establish their degree of similarity. It is impossible
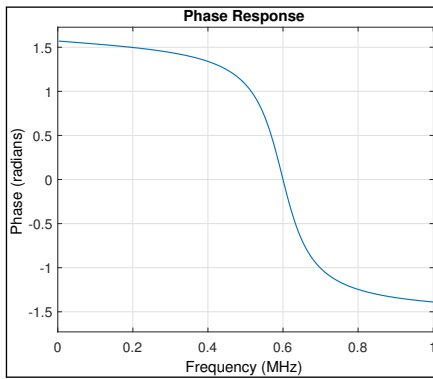
Figure 3.9: Phase response of sensor response filter
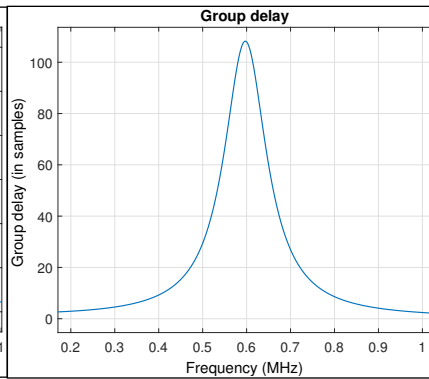
Figure 3.10: Group delay of sensor response filter

Table 3.1: Sensor response filter specification

Peak frequency	600 kHz
Bandwidth	60 kHz
Pass amplitude	1dB
Order	2

for them to exactly match, so a minimum degree of similarity should be established. Three main criteria are chosen: frequency components, amplitude of local maxima and minima and arrival time of certain characteristics.

3.4.1. COMPARISON METHOD
The three main similarity criteria are discussed here.

Frequency components   One way to compare signals with each other is by their frequency components. In Equation (3.2) a method was introduced to do this based on their FFT obtained power spectra. However, the signals are likely less similar when comparing simulations to experimental data, then they are during convergence studies. This makes the use of FFT less suitable. Also, the time of certain frequency component are of interest, but FFT analysis is not a accurate method for this. The Vallen software package offers two alternative ways to decompose a signals frequency components over time.

The first is Wavelet analysis. Wavelet analysis makes use of a *mother wavelet* to scan the signal for similarities with itself. By changing the duration, and thus the frequency of this wavelet, the signal is tested for different frequencies. A convenient side effect of this method is that the high frequency waves are scanned with high temporal resolution, and the low frequencies with a lower temporal resolution. The temporal resolution at the low frequencies is less important, since these tend to change less abrupt. This way the Heisenberg uncertainty principle, which states a temporal resolution is a trade off with frequency resolution, is less inconvenient.

A second method to decompose the frequency components of a signal is using Choi-Williams transformation. This method is a more recent development in signal processing, promising a better frequency and
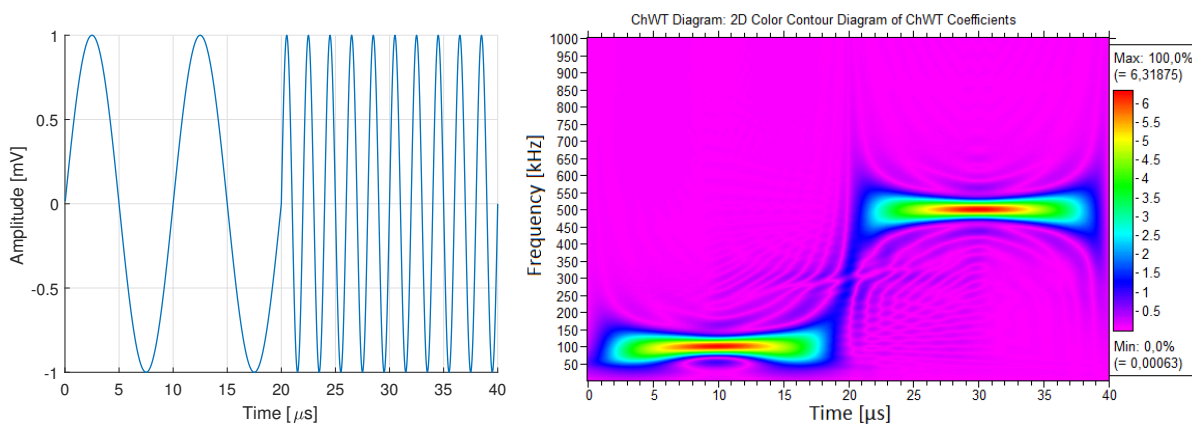
(a) Example signal in time domain

(b) Example signal in frequency domain

Figure 3.11: Choi-Williams transformation

temporal resolution, with a lower amplitude accuracy as trade off. This method will be used throughout this thesis, using the *Vallen Wavelet* program to calculate and display the transformed signals.

An example of a Choi-Williams is presented is Figure 3.11. A signal that consists purely of a 100 kHz sine wave for $t < 20\,\mu s$, and a 500 kHz sine wave for $t \geq 20\,\mu s$ is shown in Figure 3.11a. A CW transformation is performed, of which the results are plotted in Figure 3.11b. The two frequencies are clearly recognizable.

Amplitude   Apart from comparison in the frequency domain, the signal in time domain will be used. The relative amplitude of different waves are a very intuitive way to compare signals. For time picking purposes, the relative amplitude of different waves or wave components yield more relevant information than the absolute amplitude. No effort will be put in simulating the actual amplitude of the signals, but the simulated signals will be monotonically scaled in amplitude to the relevant experimental signals. After amplitude scaling the simulated signal to the experimental signal, the relative amplitudes of waves will be compared, in order to establish their similarity.

Arrival times of characteristics   The arrival time of certain signal characteristics are also of great interest. This might be the most important aspect of the simulation, since this has direct consequences for time picking, and thus localization of AE sources. Several characteristics will be evaluated in order to establish the degree of similarity between simulated and experimental signals. Local maxima and minima, HC, AIC, BK and MA, described in Section 2.3 will be used.

3.4.2. MINIMAL DEGREE OF SIMILARITY
PLB's are to some extent a stochastic process. Although the recorded signals can look very similar, two signals will never be exactly the same. Slight deviations in the PLB location and pencil lead material are two examples of variables in this process. Crack growth signals are expected to deviate even more from each other, simply because every step in crack growth is different in geometry, location, time interval. These are all factors that are not easily measured, and will need to be approximated by matching the simulation results to the experimental results.

As stated in Section 1.4, the goal of this research is to determine what influence crack geometry, specimen geometry, and other local factors, have on the AE signal. In order to do this, comparable signals must be generated as those that could be encountered during experimental measurements. However due to the stochastic nature of the source functions, exact replication of signals might not be possible. Rather than exactly replicating a certain signal, the goal of the simulations is to reproduce certain properties, in order to verify the physical correctness. When this is the case, the model can be used to predict the influences of more complex geometry components.

Effort will be put in getting the signals to match as closely as possible. Afterwards it will be discussed whether the achieved results are satisfactory for the current goals.

4

SIMULATION OF PENCIL LEAD BREAK

As a starting point for the simulation of Acoustic Emission, Pencil Lead Breaks on a simple steel plate are simulated. This is a convenient first step, because the source model is simpler, better controllable and easier to generate than AE waves originating from fatigue crack growth. This way, the rest of the model can be set up, before the more complicated source model for fatigue crack growth is implemented.

4.1. EXPERIMENTS

Specimen   The used specimen is a steel plate with a thickness of 5 mm, its form shown in Figure 4.1. The material has a yield strength of 235 MPa. In order to avoid reflections arriving at the sensor before the initial waves have completely passed, a larger plate would be preferable. However, this plate is used because of it's availability, as well as the fact that it will be used for the fatigue experiment in chapter 5. This way the geometry and material will be the same for both simulations.

Equipment   The AEM equipment that was used is described in section 1.2.4. One sensor was used to obtain the signals for simulation. Two other sensors were used to verify the general location of the PLB. A pencil of type 0.35 mm 2H was used. The amplitude threshold was set at 40dB. Recordings were made using a 100 kHz–1000 kHz digital bandpass filter.

Procedure   Two separate tests have been performed on different dates. During the first test, focus was laid on obtaining signals at a broad range of distances, mostly ranging from 10 mm to 100 mm. The second test was later on in the project, and laid focus on PLB's close to the sensor, i.e. 5 mm to 20 mm. Data of the first test will be used to verify the simulations at greater distances, while data of the second test will be used to verify the simulated signals close to the source.

Environment   The PLB's were carried out in the PME workshop at the Delft University of Technology 3ME faculty. Machining activities were ongoing during the AE measurements. The specimen was laying on a wooden work bench, being separated from the surface by bubble wrap. Typical noise, preceding the PLB signals, had an amplitude of approximately 0.02 mV, which is 26dB$_{AE}$. PLB signals had an amplitude in the range of 70dB$_{AE}$ to 90dB$_{AE}$. The noise was of little influence.
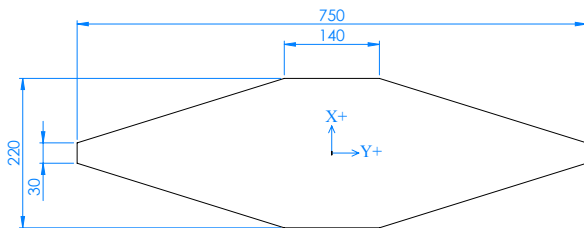
Figure 4.1: Dimensions of plate specimen

(a) Experimental signals at 5mm

(b) Experimental signals at 10mm

(c) Experimental signals at 30mm

(d) Experimental signals at 70mm
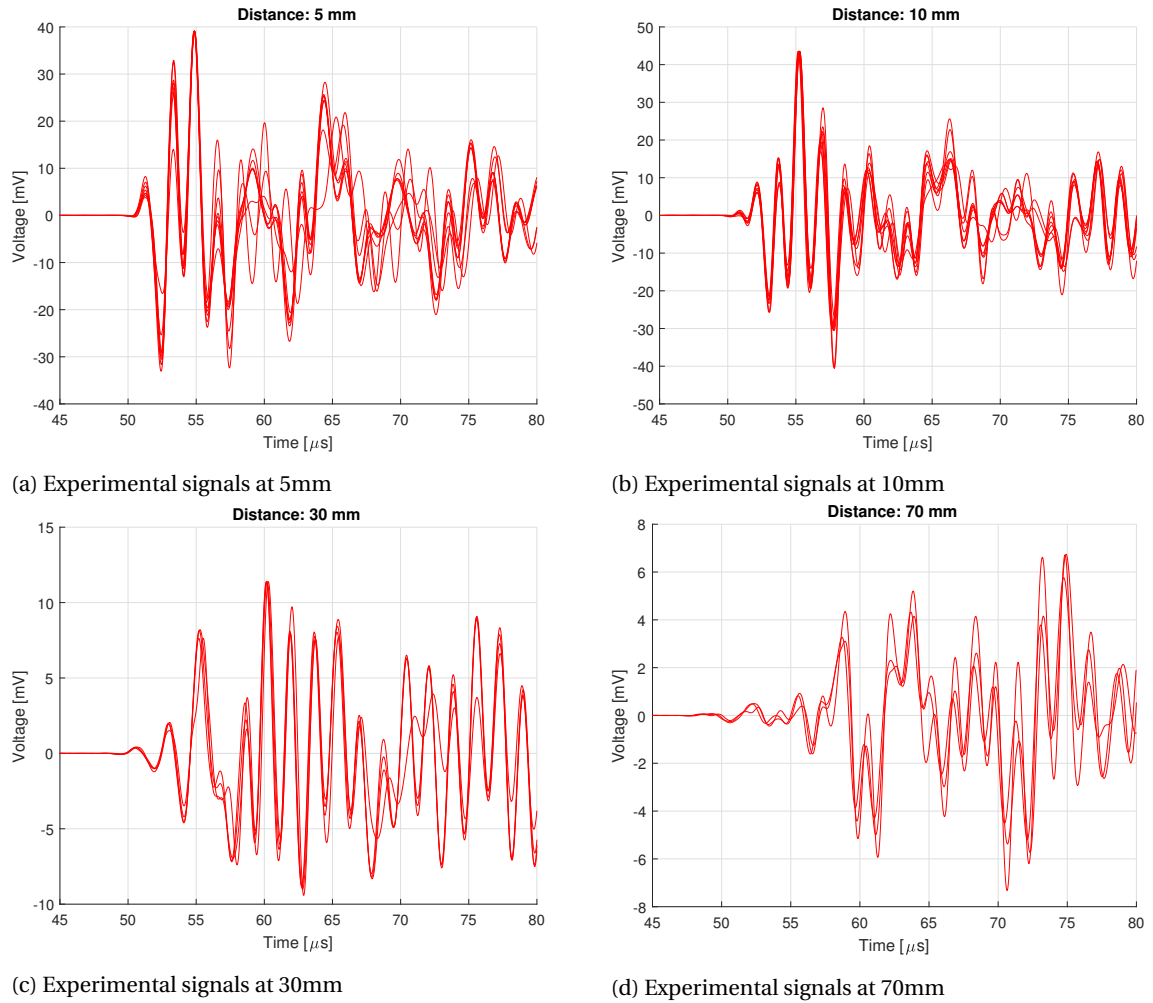
Figure 4.2: Experimental signals at several distances from the sensor

Results   Figure 4.2 shows the signals generated at several distances away from the sensor. Attention should be paid to the different *y*-scales. Each line in the graphs represents a single recording. Note that the signals have been shifted in time, to better be able to compare them to each other. The way the signals are detected is based on a certain amplitude threshold. It was found that synchronizing the first peak arrivals rather than the threshold crossing is better way to compare them, since the amplitude of each signal differs to some extend, affecting the relative TOA.

The amplitude of a signal can yield important information on of the size of a defect, or whether a PLB has been performed correctly. However, as explained in chapter 3, for time picking purposes the relative amplitude of wave components are more relevant than the absolute amplitude, so the simulated signals will be monotonically scaled to the experimental signals. For this reason, and to be able to compare them more easily, the maximum amplitudes of the signals have been scaled to be identical with the chronologically first signal.

When comparing the figures, two notable aspects can be observed. First of all, the maximum amplitude shows a rapid decrease in the first travelled millimeters. From a maximum observed of 60 mV at 5 mm, to 24 mV at 20 mm. The second aspect is the similarity of the grouped signals. At 30 mm, the signals seem to resemble each other well during the whole shown time interval. Both arrival time of peaks, as well as relative amplitude of peaks are a good match. The same cannot be said for the recordings at 5 mm. At this distance the signals seem to be similar for the first few waves, but after approximately 8 μs they seem to deviate from each other. During simulation of these recordings, emphasis will be laid at the first few waves.
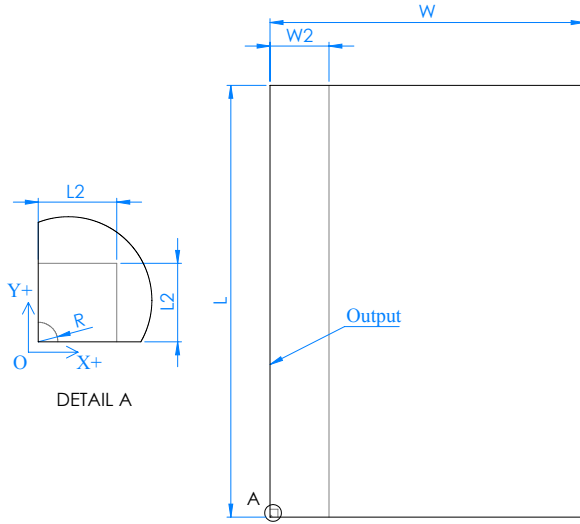
Figure 4.3: FE model geometry
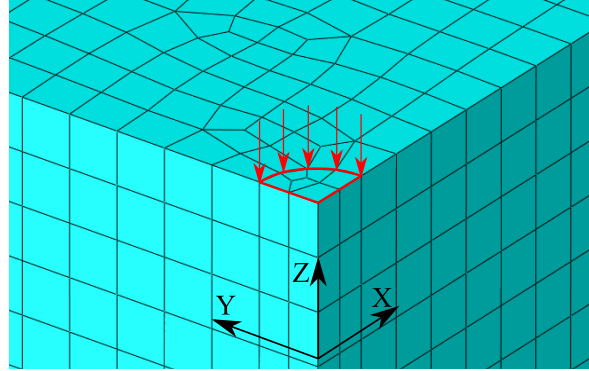
Figure 4.4: Close-up of loaded PLB surface

Table 4.1: Material properties

Elasticity modulus	E	$210 \times 10^9 \, \text{N/m}^2$
Poisson ration	v	0.287 –
Mass density	ρ	$7800 \, \text{kg/m}^3$
Longitudinal wave speed	c_L	$5.917 \, \text{mm/µs}$
Transverse wave speed	c_T	$3.234 \, \text{mm/µs}$

4.2. MODEL DESCRIPTION

4.2.1. GEOMETRY AND MATERIAL

The geometry of the models that will be used throughout this chapter is given in Figure 4.3. Although the dimensions and mesh will be vastly different, the global layout will be the same. The source function, which will be described in the next section, is located at the top surface of the plate $z = 5$ mm, at $(x, y) = (0,0)$mm. The edge on the $x = 0$ mm plane has a x symmetry condition, meaning movement in the x direction and rotation around both the y and z axis are constrained ($U_x = R_y = R_z = 0$). The edge on the $y = 0$ plane has a y symmetry condition ($U_y = R_x = R_z = 0$). To prevent rigid body motion in z direction, the outermost node $(x, y, z) = (W, L, 0)$ is constrained in z direction ($U_z = 0$).

Single line outputs, described in Section 3.2.3, will be generated along the top and bottom surface edges on the $x = 0$ plane, since the waves propagate uniformly in all directions through the plate. To reduce the computational load, the fine mesh in the range ($0 < x < W2$) will be coarsened at $x = W2$ to the coarse mesh size used in the range ($W2 < x < W$). To make sure no significant reflections will be generated at this interface, outputs in nodes $(x, y, z) = (0, 5, 5)$[mm] and $(x, y, z) = (5, 0, 5)$[mm] will be compared with each other. The mesh size near the AE source at $(x, y) = (0, 0)$ will be increased further, to allow for multiple element lengths to be excited by the source force.

The material properties used are given in Table 4.1. The theoretical longitudinal and transverse wave speeds, according to Equations (2.1) and (2.2), are also given here.

4.2.2. SOURCE MODEL

During a PLB, a force is applied on a small surface. When the pencil breaks, this force is suddenly removed, this process forms the AE waves. The development of the load over time is not easily measured, due to its fast nature. For this reason, several *source functions* are used in simulations, to determine which one fits best to the experimentally recorded signals. The source functions that were investigated are listed in Table 4.2.

The source functions are set up in such a way, that they are opposite of reality in terms of load development. In reality, a quasi-static force acting on the surface is removed. The modelled PLB however, starts a a load of 0 N, ramps up to a certain value, after which it stays constant at 1 N. In post processing, the obtained

signal is mirrored with the $z = 0$ axis, to obtain physically correct signals. This method saves a pre-loading computational step, and has been described by Prosser et al [13].

Table 4.2 lists all investigated source models, and refers to the functions named *Ramp*, described in Equation (4.1), sin^2 described in Equation (4.2), *sin* which is the same as the sin^2 function, but without the power of two, and lastly *exp* which is an exponential function described in Equation (4.3). In this function, *exp* denotes Euler's number to the power of the term in brackets. This last function is based on the work of Cuadra et al [6], which used a similar function, given in Equation (4.4), to model crack growth. During this research it was found to be a good source function to model a PLB.

For the magnitude of the force, a value of 1 N has been chosen. The actual load is unknown, but this value corresponds to what several authors used in papers which are discussed in Chapter 2. This arbitrarily chosen value is of low significance, since the obtained results will be monotonically scaled to the experimental signals.

Section 4.2.4 describes the selection process of the most accurate source function.

$$F(t) = \begin{cases} \frac{t}{T_0} & \text{for} \quad t \le T_0 \\ 1 & \text{for} \quad t > T_0 \end{cases} \tag{4.1}$$

$$F(t) = \begin{cases} \sin\left(2\pi t \cdot \frac{1}{4 \cdot T_0}\right)^2 & \text{for} \quad t \le T_0 \\ 1 & \text{for} \quad t > T_0 \end{cases} \tag{4.2}$$

$$F(t) = \begin{cases} \exp\left(-\left(\frac{1}{2}(t - T_0)\frac{5}{T_0}\right)^2\right) & \text{for} \quad t \le T_0 \\ 1 & \text{for} \quad t > T_0 \end{cases} \tag{4.3}$$

$$\delta(t) = \frac{C}{a\sqrt{\pi}} \cdot \exp\left(-(t - 1/2a)^2\right) \tag{4.4}$$
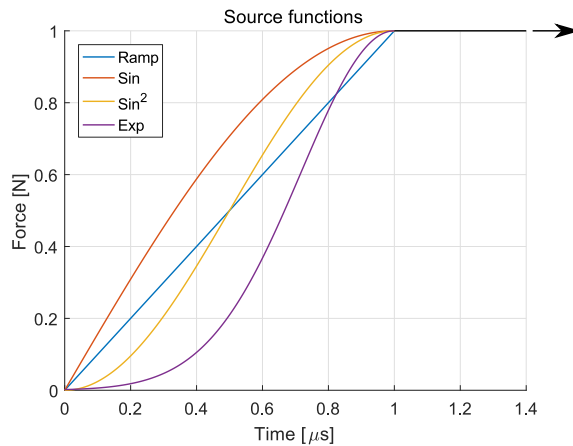
Figure 4.5: Source functions normalized to 1 μs

Table 4.2: Variations in PLB source function

Case	Function	T_0
1	Exp	1.5 μs
2	Exp	2 μs
3	Exp	2.25 μs
4	Exp	2.5 μs
5	Sin^2	1.5 μs
6	Sin^2	1.75 μs
7	Sin^2	2 μs

4.2.3. DISCRETIZATION

In order to reduce computation time, for the convergence study a smaller model is used than during the final PLB simulations. The layout shown in Figure 4.3 is used. A length L=30 mm, width W=50 mm and fine mesh zone width W2=20 mm are used. The plate thickness of 5 mm remains unchanged throughout this chapter. A simulated time of 15 μs has been chosen. Virtual single node sensors are located on 5 mm and 20 mm. This layout has been chosen to minimize simulation time, and ensure reflections will have traveled back along the y axis, but not along the x axis.

Both linear and quadratic elements have been investigated. Since the Abaqus does not contain quadratic hexagonal elements, only the quadratic tetrahedron elements are investigated. For the linear elements, hexagonal elements are used. Table 4.3 lists the element type, global mesh size and used time step of the used models. Time steps are kept nearly constant for each element, ruling out differences in that respect. Time steps are however assumed to be sufficiently small, since the CFL stability condition, mentioned in Section 2.4, for Abaqus/Exlplicit dictates a very fine time step.

Table 4.3: 3D element convergence

Element type	Elememet size mm	Time Step s
Linear Hexagonal	0.08	7.50E-09
Linear Hexagonal	0.1	7.50E-09
Linear Hexagonal	0.125	7.50E-09
Linear Hexagonal	0.25	7.50E-09
Linear Hexagonal	0.5	7.50E-09
Quadratic Tetrahedron	0.125	2.17E-09
Quadratic Tetrahedron	0.25	3.10E-09
Quadratic Tetrahedron	0.33	2.70E-09
Quadratic Tetrahedron	0.5	3.10E-09

PRODUCED SIGNALS

When looking at the produced signals in Figure 4.6, it can be concluded that most of them have the same global form. Only the most coarse linear mesh, which is represented by the red line in both figures, stands out in both plots.

The coherence between the signals is plotted in Figure 4.7. Both the 5 mm and 20 mm signals are divided by element type. The level of coherence seems to decrease for larger mesh sizes and higher frequency. This is to be expected, since higher frequency signals have smaller wave lengths, thus suffering form coarser mesh sizes first. The 0.1 mm and 0.125 mm linear elements seem to have a high coherence level with the 0.08 mm linear mesh, at both 5 mm and 20 mm travel distances. The 0.25 mm and 0.33 mm quadratic elements have a high coherence level with the corresponding 0.125 mm mesh.

INTERPOLATED SIGNALS

The most important feature to be evaluated for the mesh size is the arrival time of certain features. Figures 4.8a and 4.8b show the TOA of the first peak, along with their amplitude. Since the signals are sampled at 0.025 µs, but the differences in arrival time are far smaller, quadratic interpolation is performed on the signals to obtain a sampling time of 0.001 µs. While this is merely an approximation of what the signal would look like if a higher sampling rate was used, it does increase the ability to compare the arrival times in an effective manner.

Arrival times Both the linear and quadratic meshes seem to show a decrease in the rate of change when using a increasingly small element size. The arrival times using a mesh with quadratic elements are converging earlier than the linear element meshed simulation signals, even when taking into account the fact that the nodal distance of a quadratic element is actually half the element size. Note that the sample time of the AMSY-6 is 0.025 µs, the differences shown in the figures should be evaluated with this in mind.

Amplitudes The amplitudes of the first peaks also seem to converge to a certain value for both evaluated sensor distances. The quadratic mesh however does exhibit strange behaviour. Upon closer inspection of the simulation results, the deformed shape of the quadratic meshed model shows strange values. A static shape that is similar to hourglassing is observed for all mesh sizes. Although this seemingly does not affect the generated signals, except for a small amplitude shift, this behaviour is undesirable.

Selected mesh size Computational time and maximum model size are also a factor which should be weighted in. Because of this, it is not always the best option to go with the smallest elements. The discretization investigation concludes that the 0.125 mm linear elements are most suitable for the current purpose. When the mesh size is reduced further, the benefits do not weigh up to the increased computational time. The use of quadratic elements is averted, due to the strange hourglass like behaviour which was observed, and because it was found to be computationally far less time effective.

(a) Signals at 5 mm

(b) Signals at 20 mm
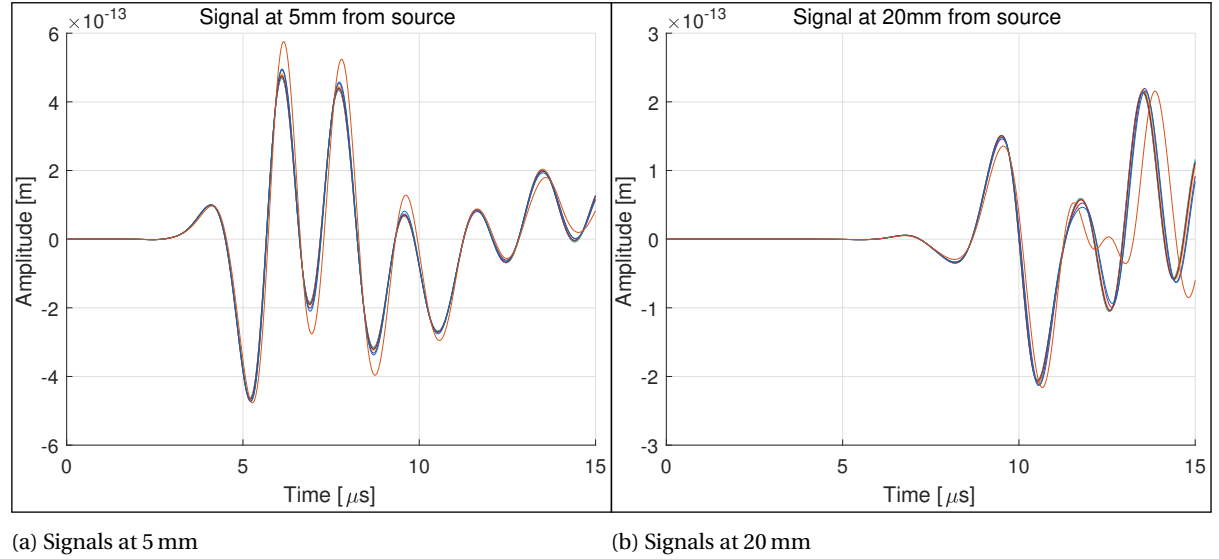
Figure 4.6: Simulated signals for convergence investigation

(a) Coherence between signals at 5 mm using linear elements

(b) Coherence between signals at 5 mm using quadratic elements

(c) Coherence between signals at 20 mm using linear elements

(d) Coherence between signals at 20 mm using quadratic elements
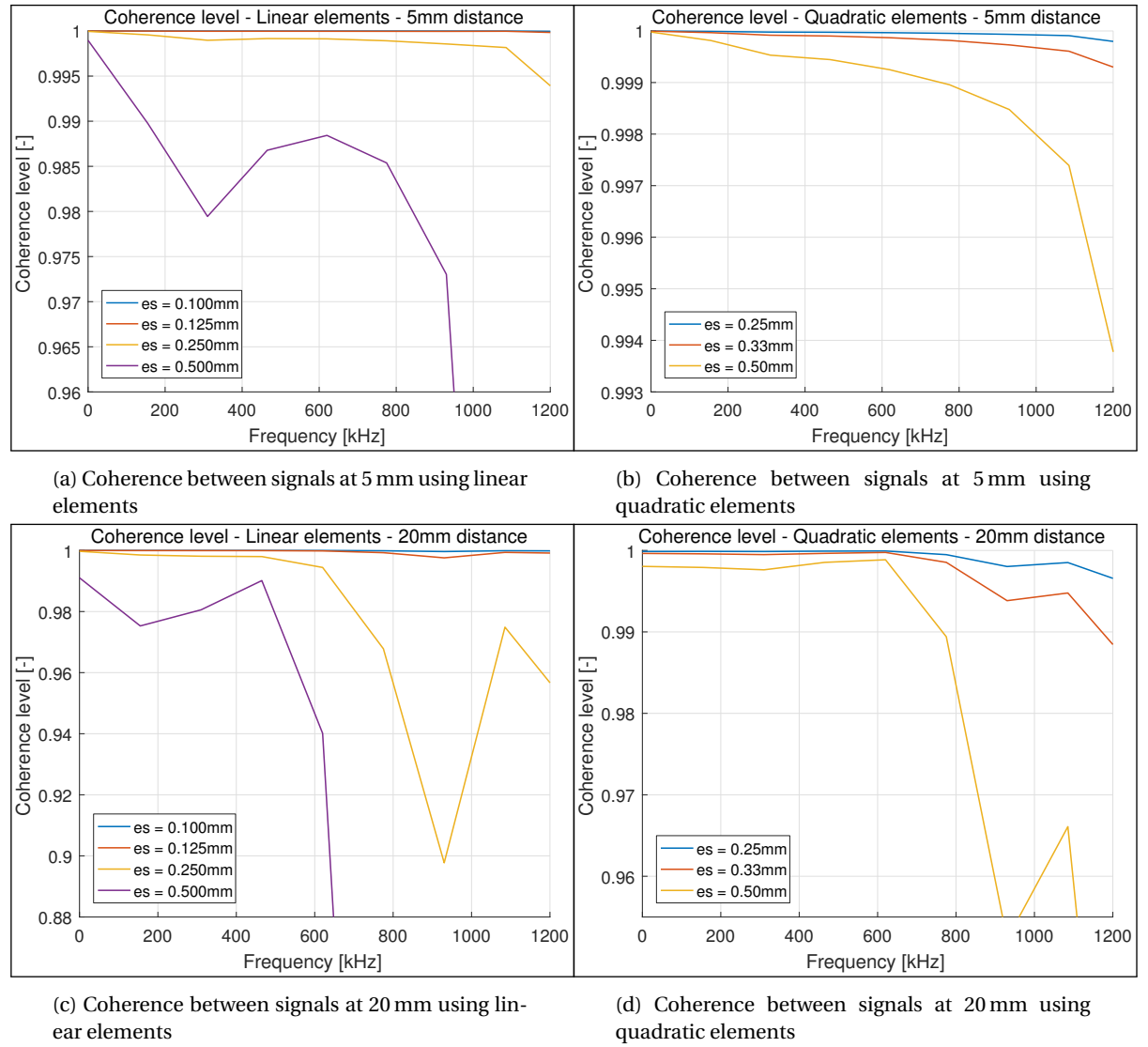
Figure 4.7: Coherence of the signals with respect to the finest mesh signal

(a) First peak at 5 mm   (b) First peak at 20 mm
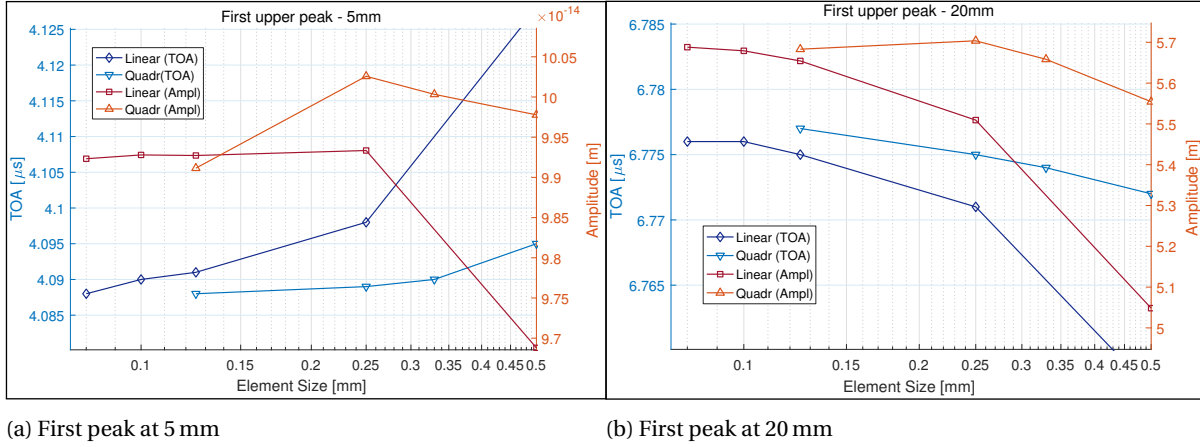
Figure 4.8: Comparison of amplitude and arrival times of first upper peak at 5 mm and 20 mm

4.2.4. SOURCE FUNCTION SELECTION

In order to determine the the best source function, similarity criteria have been established in Section 3.4. These similarity conditions contain:

- Arrival times of local maxima, local minima and minimum HC value

- Relative amplitude of local maxima and minima

- Frequency components over time

Some of the investigated sources listed in Table 4.2 can be disregarded in an instant, while others must be tested more thoroughly to determine the best candidate. The selected source functions are the two closest variants of both the *exp* and sin^2 functions. These will be investigated in this section.

Not every PLB is identical. Each PLB varies somewhat in location and load development, both of which are uncontrollable variables to a certain extend. Although the location will be attempted to be as close as possible to the desired location, an inaccuracy of half a millimetre is not unlikely. Since it is not possible to tell which experimental PLB signal is the *ideal* one, each candidate source function will be tested to every available experimental signal. Also a spread of 0.5 mm will be taken into account. For each simulated source function, the best matching signal will be selected, to compare it with. This means that the signals in the comparison graphs are not all tested against the same experimental signal.

The FE model to investigate the source used a length L=80 mm, width W=65 mm and width W2=20 mm, referring to the dimensions shown in Figure 4.3. Signals were obtained using the single line output described in Section 3.2.3.

SOURCE FUNCTION SUMMARY

Figure 4.9 shows the TOA and amplitude differences for the best four PLB source functions. A more in depth analysis has been given in Appendix A, as well as additional information on the other sources, which are omitted in the mentioned plots. This appendix also contains the CW transforms for the four investigated sources.

In general, it can be concluded that the *exp* sources outperform the sin^2 sources in terms of arrival time and amplitude differences. The sin^2 sources however, simulate the waveform of the first waves at short distances better. This could be due to the fact that the sensor response simulation filter attenuates these high frequency components too much, which can be seen in Figure 3.8, and the sin^2 sources actually generate too much of these. These low amplitude waves however, have less impact on the time picking than the bigger waves arriving immediately after them, which are better simulated by the *exp* sources. The difference in performance of the *exp* source functions do not differ significantly from each other. The *exp* 2.25 µs seems to overall be slightly better. For this reason the *exp* 2.25 µs source will be used to investigate the PLB signal simulation further.
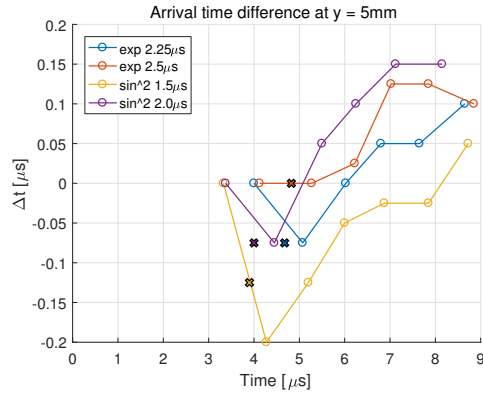
(a) Difference in arrival time at 5 mm
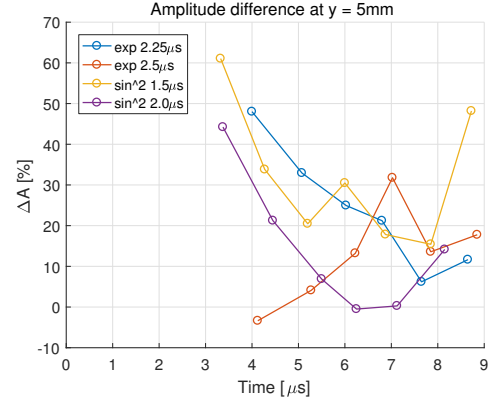
(b) Amplitude difference at 5 mm
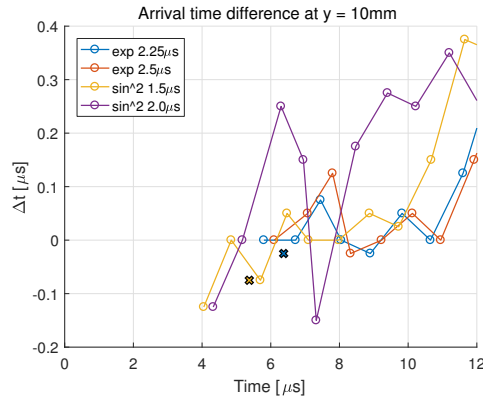
(c) Difference in arrival time at 10 mm
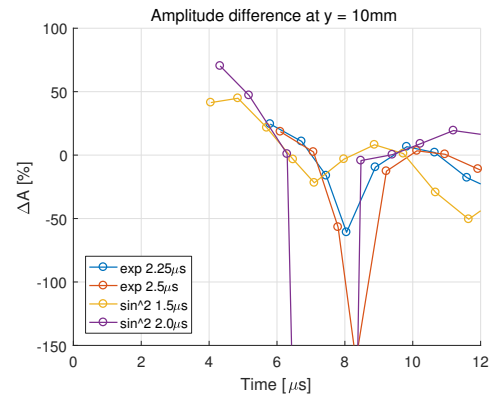
(d) Amplitude difference at 10 mm
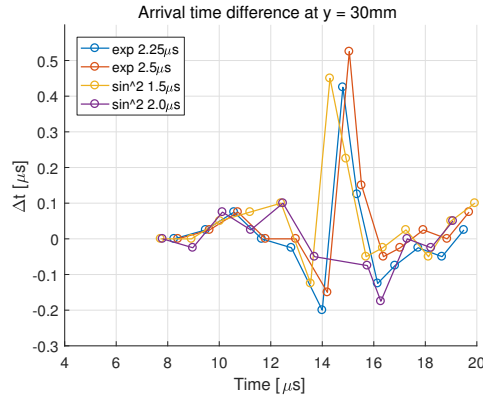
(e) Difference in arrival time at 30 mm
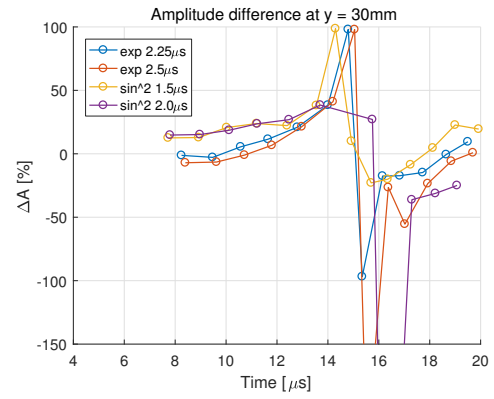
(f) Amplitude difference at 30 mm
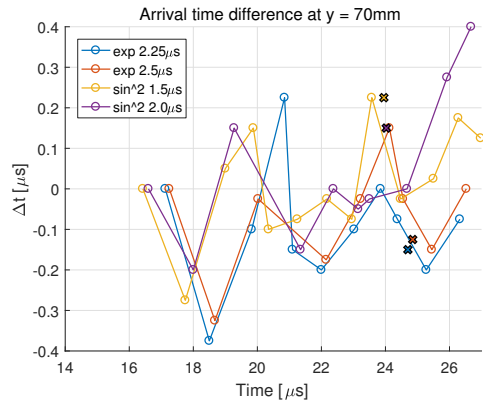
(g) Difference in arrival time at 70 mm
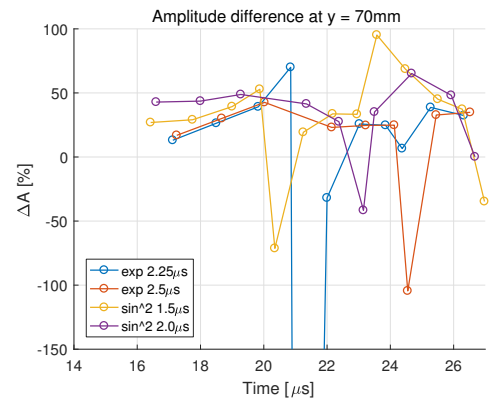
(h) Amplitude difference at 70 mm

Figure 4.9: Source comparison of best four PLB sources

4.3. SIMULATED SIGNALS

4.3.1. COMPARISON WITH EXPERIMENTAL SIGNALS

Section 4.2.4 described the process in which the *exp* 2.25 μs source was selected as best fitting source to simulate PLB's. One final PLB simulation has been performed with quarter plate dimensions of 80×110×5 mm. A mesh with a maximum element edge length of 0.125 mm has been used, in accordance with the findings in Section 4.2.3. The simulated signals at 5, 10, 20, 30, 50 and 70 mm travel distance are shown along with their best fitting experimental counterparts in Figures 4.11a to 4.11c and Figures 4.13a to 4.13c. Differences between the simulated and experimental signals in four time picking criteria have also been shown in Figures 4.11d to 4.11f and Figures 4.13d to 4.13f. These time picking criteria are the peaks, Hinkley criterion, Baer & Kradolfer function and Akaike information criterion. The frequency components over time are calculated using Choi-Williams transformation, and are shown in Figures 4.12a to 4.12c and Figures 4.14a to 4.14c.

Apart from the single line output, this simulation also makes use of an additional plane output, ranging from 0 < x < 15 mm and 0 < y < 15 mm, in order to extract the signals close to the source in a more realistic way.

Signals at all sensor distances seem to match the recorded signals in an accurate way. The HC determined TOA however, seems to be better simulated at smaller distances than at sensors further away. The AIC determined TOA is not accurately simulated.

4.3.2. COMPARISON WITH LAMB WAVE THEORY

Beside the comparison of the simulated signals to the experimental signals, it is also interesting to compare the signals to theory of wave theory in general. The simulated signal at 70 mm has been chosen for this comparison, because here a clear separation of the S0 and A0 wave modes should have taken place, so they can be observed separately. The signal at the top and bottom surface of the plate have been shown in Figure 4.10a. The signal obtained by the bottom sensor has been mirrored with the horizontal axis, because this sensor is physically upside down. When the surfaces move away from each other, so do the lines in Figure 4.10a. In this figure it can be seen that the first arrival of the waves around 15 μs are the symmetric waves, since the surfaces move away from each other, like is schematically shown in Figure 2.1. Somewhat later, at around 22 μs, the surfaces begin to move in a anti-symmetric fashion. Around 32 μs a symmetric waveform start to dominate the signal again.

Section 2.1 discussed dispersion curves, and the velocities of the different wave modes that take form. The Choi-Williams transformation of the top signal is shown in Figure 4.10b, overlaid with the dispersion curves for this particular plate. This figure predicts the S0 waves to arrive first. The energy of this mode is not visible, although the waves are visible in the left graph. This can be explained by the low amplitude of the waves. The arrival of the A0 wave however can clearly be seen in the CW transformation, as can the symmetric waves in which dominate the signal after 32 μs. These waves seemingly also belong to the S0 mode, but travel slower

(a) Wave at top and bottom of plate   (b) CW tranform with dispersion curves for 70 mm signal
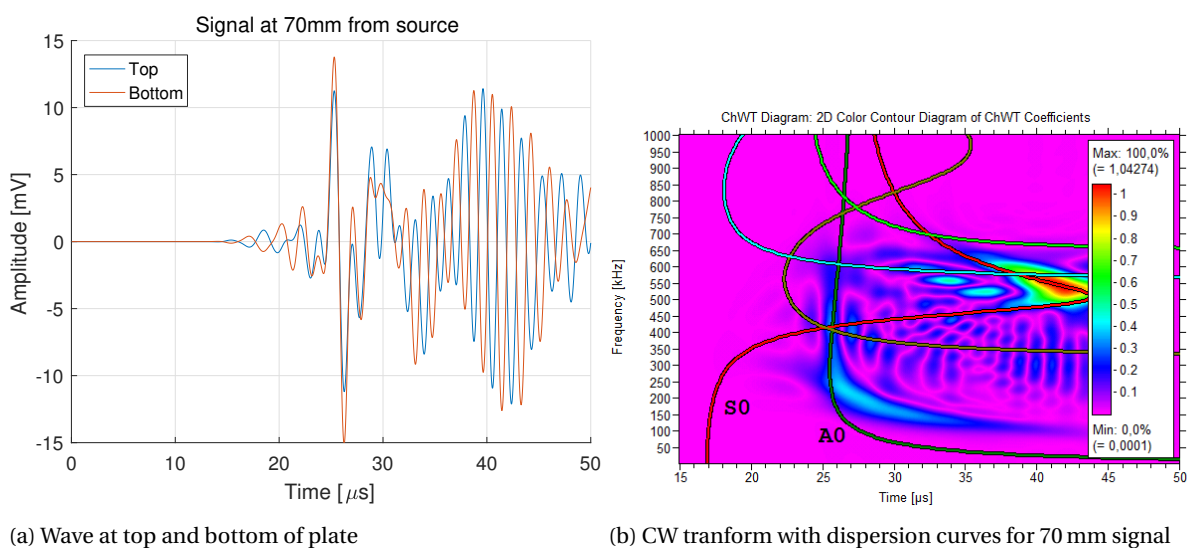
Figure 4.10: Analysis of the simulated PLB at 70 mm

than their low frequency parts. These waves are very pronounced since they lie near the resonating frequency of the VS600-Z2 sensors, which is 600 kHz.

4.3.3. ATTENUATION

In Chapter 6 the influence of local geometry on the signal will be predicted. Attenuation will play an important role here, since the amplitude of a reflected signal will in part determine the degree it will distort the original wave.

To compare the simulated attenuation with the experimental data, the maximum absolute amplitude in the first 20 μs of each signal is plotted alongside the maximum amplitude values of several recorded PLB signals in Figure 4.15. For this comparison the data of the second test is used, since multiple PLB's are performed at the same location, and the focus is laid close to the sensor, which is the case for the crack front localization, which is the goal for this thesis. Not enough data was accumulated at further distances to get a reliable attenuation profile. A second order polynomial is fitted through the experimental data. The 95 % confidence interval is also plotted.

The correspondence is good in the first 30 mm, in which the data is available. It should be noted that since the simulation does not use damping, the attenuation at greater distances will probably be underestimated. Close to the AE source damping does not play a great role, since attenuation is dominated by wave spreading [14].
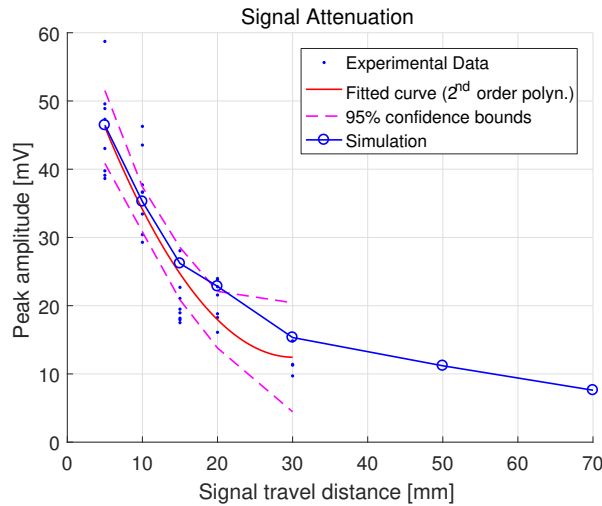
Figure 4.15: Attenuation profile of simulated and experimental signals

4.3.4. TIME PICKING

One of the advantages of a simulation is that sensor locations can be very easily varied, potentially generating a great number of signals. Figure 4.16 shows the summary of the analysis of a great number of sensor locations, ranging from 3 to 21 mm sensor distance. Each line shows the way a certain signal characteristic TOA develops over travel distance.

Each horizontal set of blue dots represent a single sensor location, corresponding to the travel distance which is indicated at the vertical axis. Each single node of this horizontal row of nodes represents a local maximum or minimum in the signal. By mentally connecting the diagonal rows of dots, one can observe the development of the several peaks, as they develop over distance. The slope of this dotted line indicates the speed at which it travels. Apart from the the local peaks, also the time pick criteria have been plotted. The separate markers at 5, 10, 15 and 20 mm show the arriving characteristics, matched by color, of the corresponding experimental signals. The AIC characteristic is omited from further analysis, since it poorly matches the simulated data.

Using this graph, travel speeds can be determined for the several signal characteristics. This is the same way as would be done in practice, but with far more probed locations.

(a) Signal at 5mm   (b) Signal at 10mm   (c) Signal at 20mm

(d) TOA comparison of signal at 5 mm   (e) TOA comparison of signal at 10 mm   (f) TOA comparison of signal at 20 mm
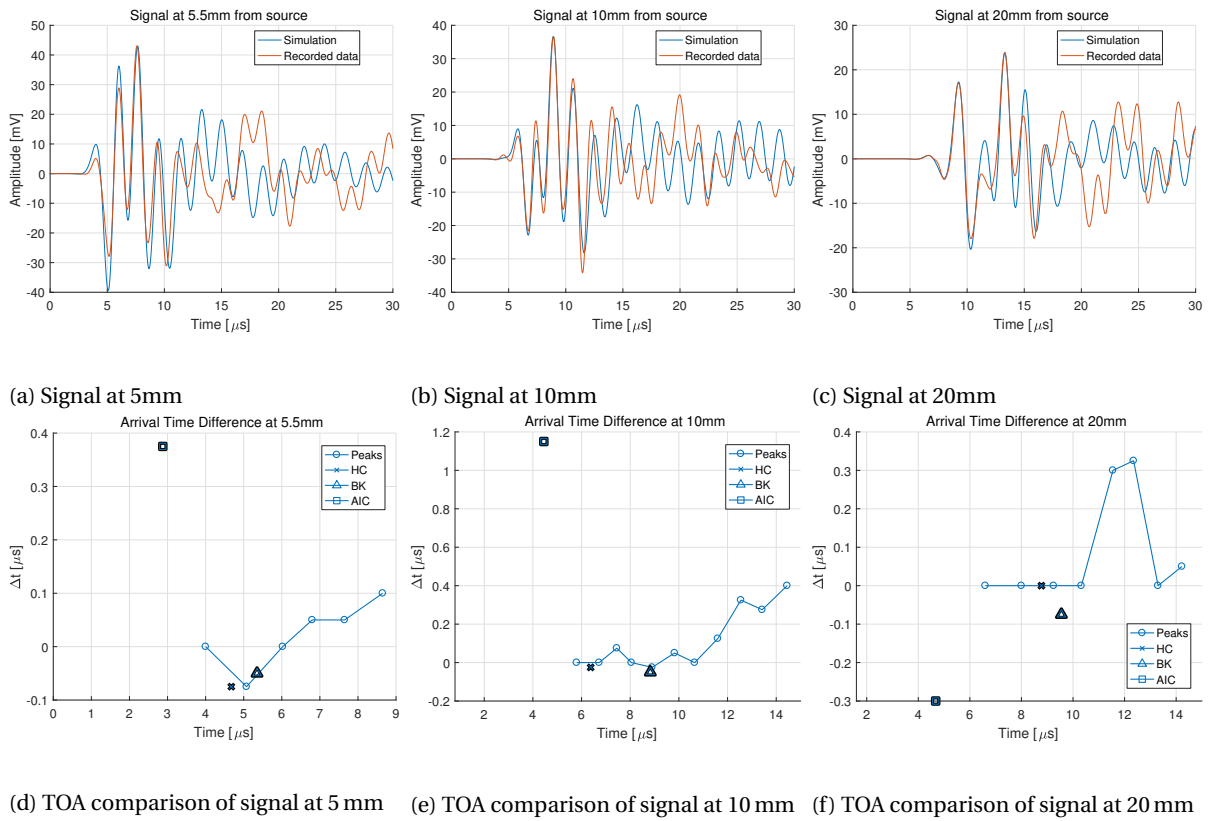
Figure 4.11: Signals and TOA comparison at 5, 10, 20 mm

(a) Choi-Williams transform of signal at 5 mm   (b) Choi-Williams transform of signal at 10 mm

(c) Choi-Williams transform of signal at 20 mm
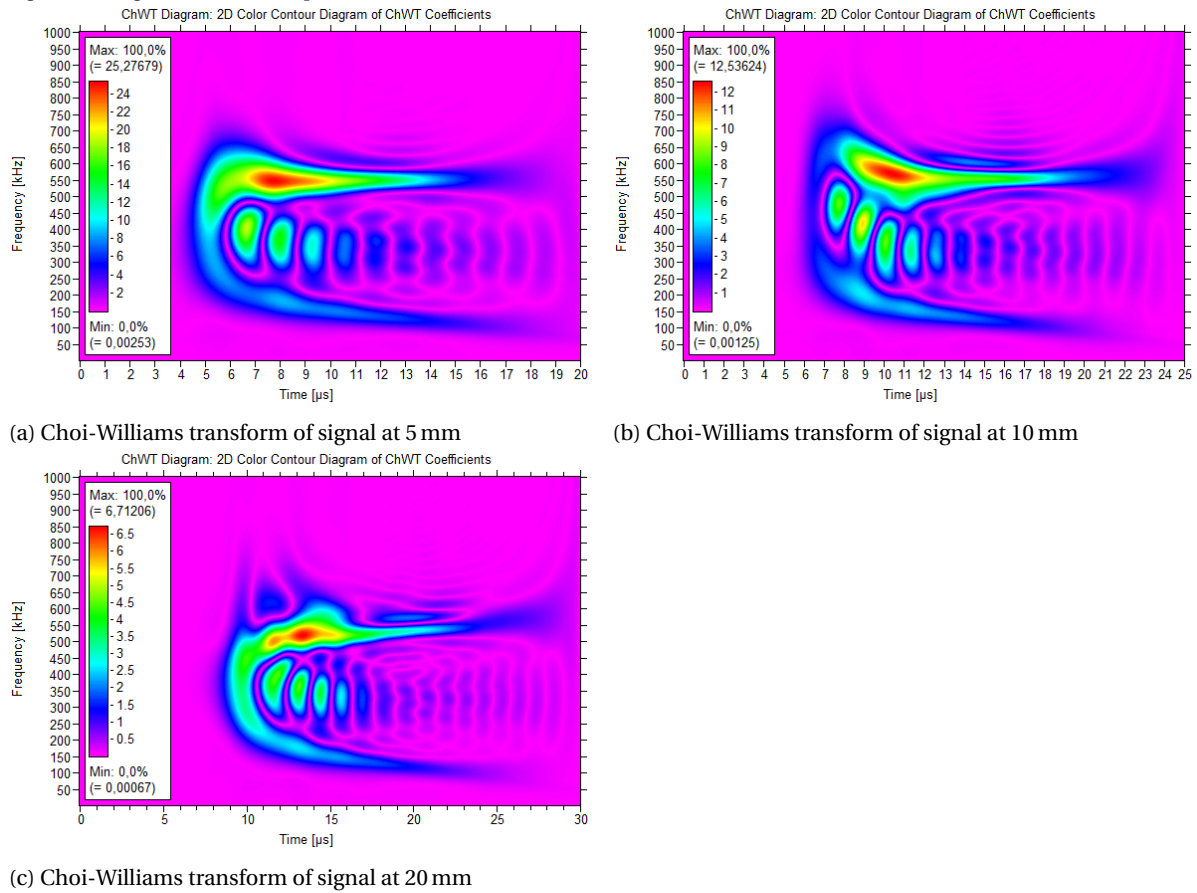
Figure 4.12: Choi-Williams transforms at 5, 10, 20 mm

(a) Signal at 30mm

(b) Signal at 50mm

(c) Signal at 70mm

(d) TOA comparison of signal at 30 mm

(e) TOA comparison of signal at 50 mm

(f) TOA comparison of signal at 70 mm
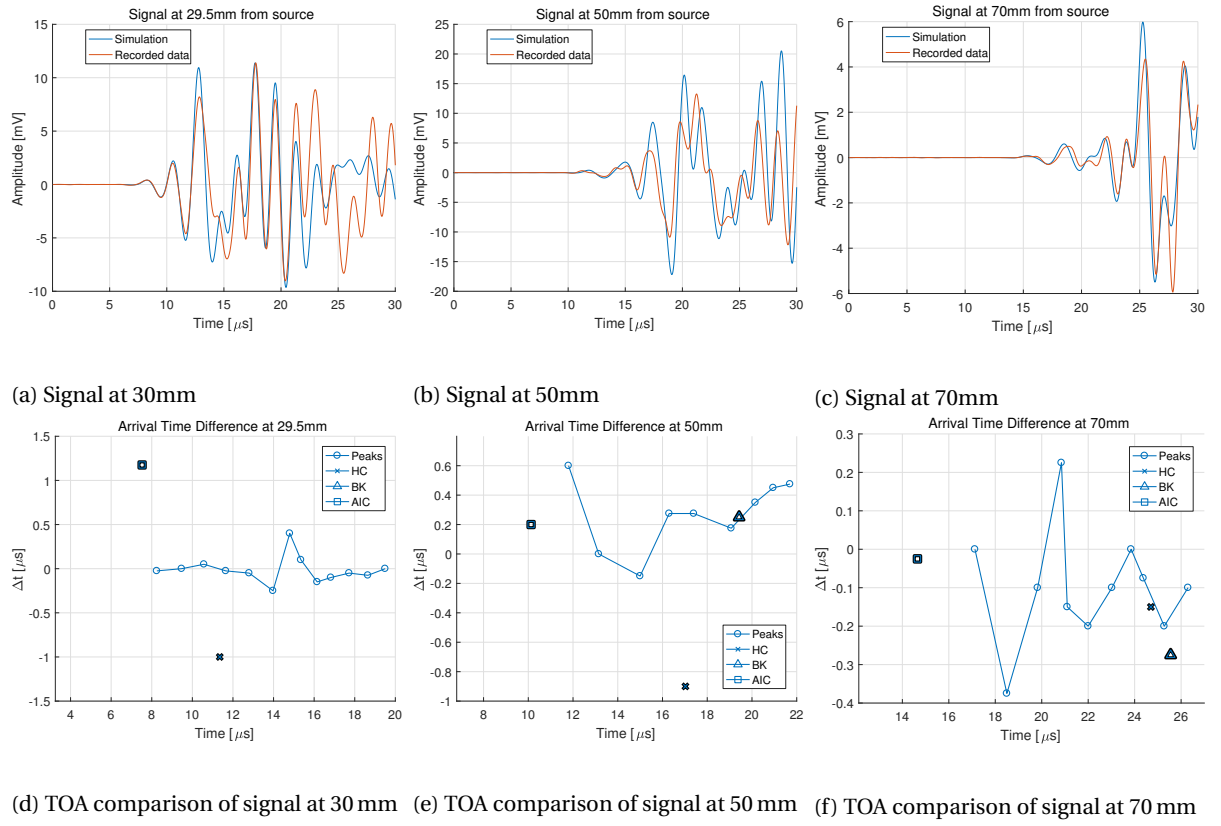
Figure 4.13: Signals and TOA comparison at 30, 50, 70 mm

(a) Choi-Williams transform of signal at 30 mm

(b) Choi-Williams transform of signal at 50 mm

(c) Choi-Williams transform of signal at 70 mm
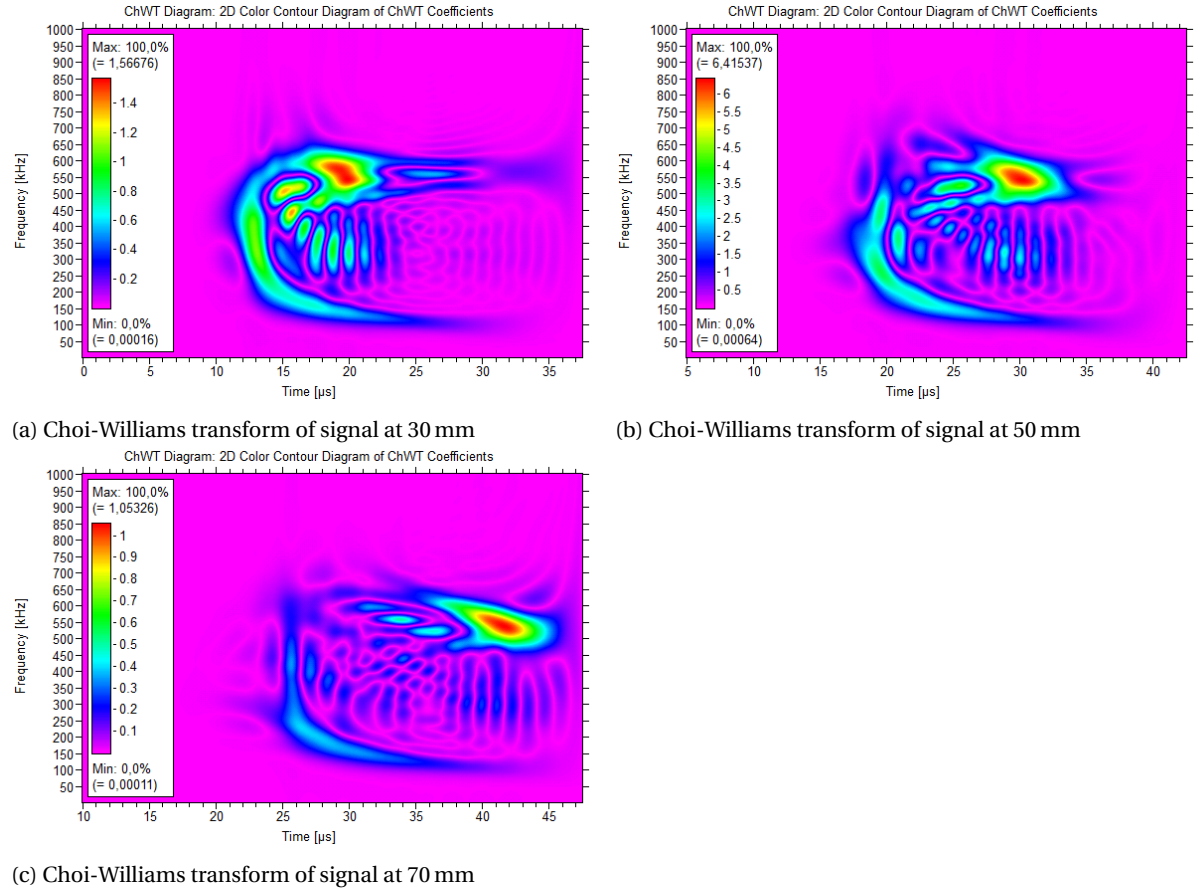
Figure 4.14: Choi-Williams transforms at 30, 50, 70 mm
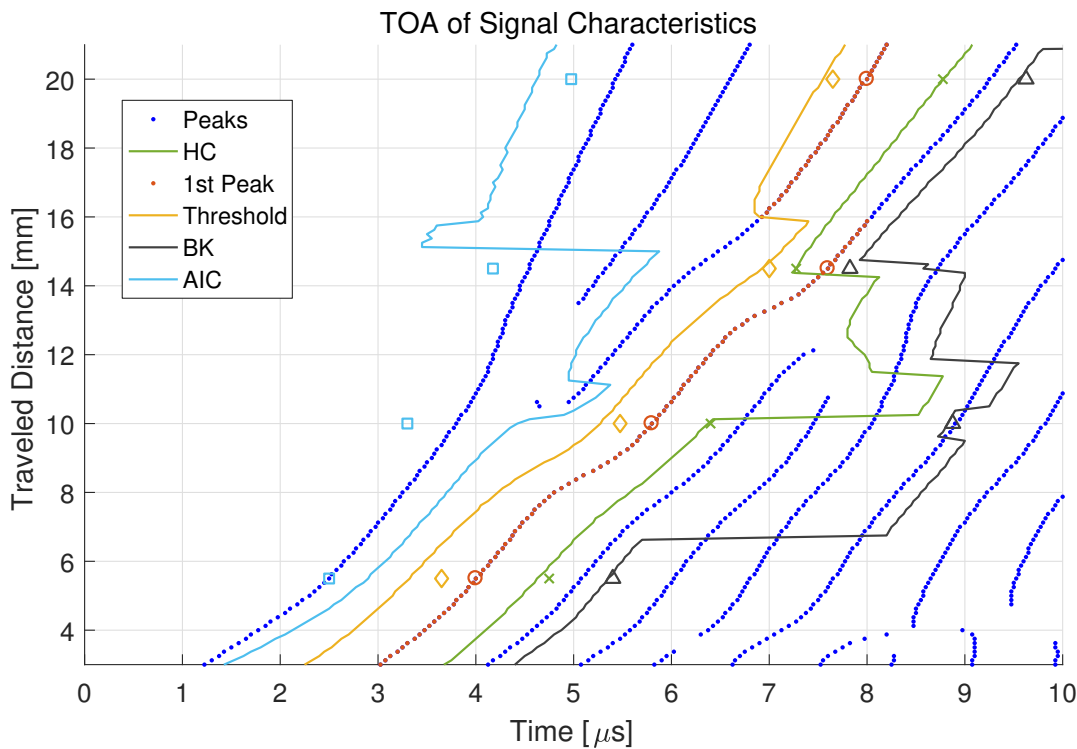
Figure 4.16: Arrival time of signal characteristics at multiple sensor locations

4.3.5. LOCALIZATION

For the distance range of 3 mm–6 mm, Figure 4.16 shows slight speed variations for the threshold, peak, HC and BK characteristics. The latter has a jump in TOA around 7 mm, but the rest of the characteristics remain mostly linear up until 10 mm. This would indicate that localization in this range would be very accurate. To investigate this, two virtual sensor arrangements are used.

Sensor arrangement *A*, which is shown Figures 4.17a and 4.17b, uses sensors at 4.5 mm, 5 mm and 5.8 mm. Localization is performed using a mean speed determined in the range of 3 mm–6 mm. The localization results for the four signal characteristics are shown in the mentioned figures.

Sensor arrangement *B* is shown in Figures 4.17c and 4.17d. The sensor distances are 8.5 mm, 9 mm and 9.5 mm. Localization is performed using the same speed as before, for which the results are also shown in the mentioned figures.

It can be concluded that the localization is highly accurate for sensor configuration *A*. It should be mentioned that this is assuming the exact sensor locations are known, which is not the case in actual experimental conditions. This high accuracy is to be expected, since Figure 4.16 shows mostly linear behaviour in this range. The speed is also easily obtained from this figure, so there is little uncertainty during localization. The localization for sensor configuration *B* is also very accurate, although it is to a slightly less degree. This is due to the slightly more varying speeds in this distance range. The localization using the BK TOA has the largest error, which is to be expected, since its TOA development makes a large jump at 7 mm, making the used speed less useful.

4.4. CONCLUSION

The PLB simulation can be regarded as successful. Signals at a range of 5 mm–70 mm have been replicated with very good likeliness. This replication at multiple distances, confirms the sensor response filter is accurate for the investigated combination of plate thickness, material and PLB source function.

There is room for improvement however, since it has been shown that the time picking of the AIC is not simulated well, as is the HC at greater distances. The arrival of a tiny first arriving wave is also unsuccessful, however this has very limited effect on the time picking functions, since its amplitude is very small. Simulation of attenuation rates in the first thirty millimetre have been verified, which will prove useful in Chapter 6, where the attenuation of reflections will be important.

(a) Sensor locations around 5 mm

(b) Localization magnified

(c) Sensor locations around 9 mm

(d) Localization magnified
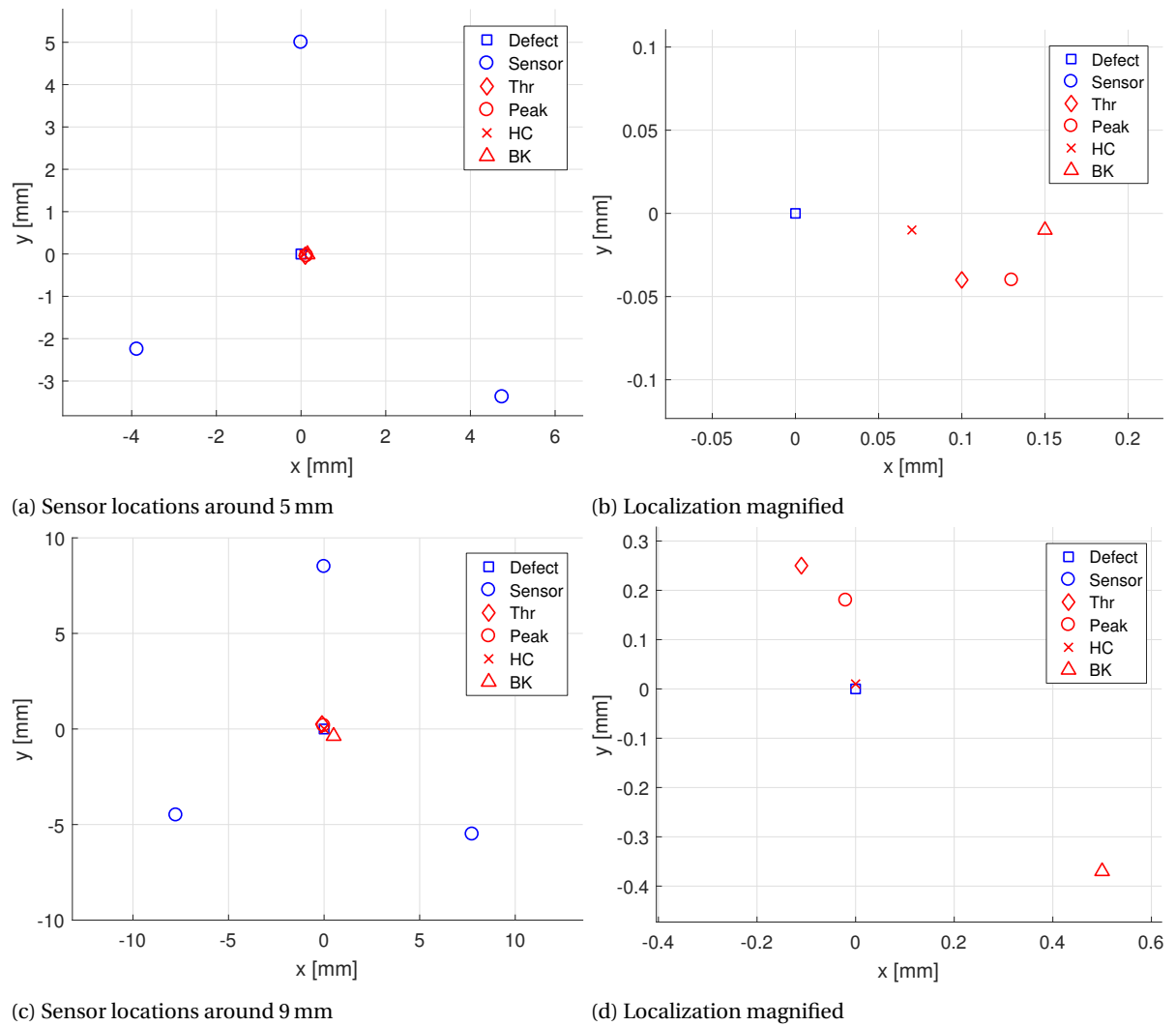
Figure 4.17: Pencil lead break localization

<div align="right">5</div>

SIMULATION OF FATIGUE CRACK GROWTH

The goal of this chapter is to report on the simulation of acoustic emission by fatigue crack growth. Effort to obtain experimental signals will be briefly touched. Since this effort remained unsuccessful, several FE source models have been used. The behaviour of the generated AE has been investigated, by examining the results of all source models. A localization accuracy down to a error of 0.5 mm has been achieved.

5.1. EXPERIMENTS

In order to form a basis for the simulations of the acoustic emission formed during fatigue crack growth, several experiments have been carried out, two of which encompassed an actual fatigue test.

One of the tested specimens was the plate with which the PLB experiments were carried out, the geometry of which is shown in Figure 4.1. The second specimen was of the same material and geometry. Both specimens were cut down to a width of 100 mm to increase the stress at the defect, and speed up the fatigue process. A semi elliptic surface defect with a depth of 1 mm, width of 5 mm and a mouth opening of 0.2 mm has been applied to both specimens by laser. The experiments have been carried out in the Material Science laboratory in the 3mE faculty in the TU Delft. An hydraulic MTS fatigue testing machine with a maximum capacity of 250 kN and maximum frequency of 20 Hz has been used. The specimens are shown in Figure 5.1.

5.1.1. FATIGUE TEST #1

The first test was carried out using a load range of 3 kN to 84 kN. The first visible fatigue crack was observed at 156,000 cycles, and was loaded until failure at 500,000 cycles. During this test, a noise level of approximately 97dB$_{AE}$ was observed, which is almost up to the full measuring range of the AMSY-6. This made it near

(a) First fatigue test   (b) Second fatigue test
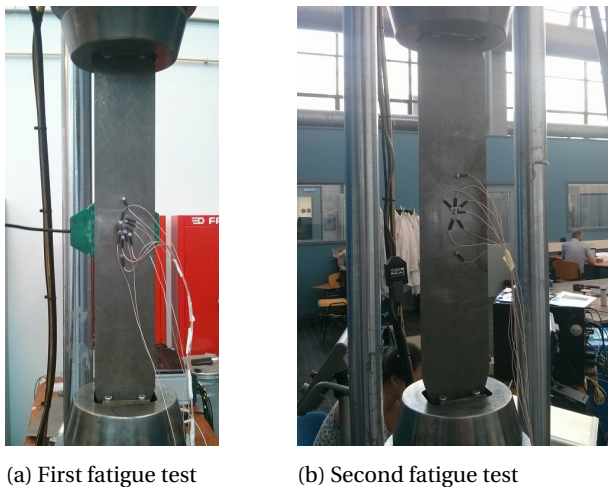
Figure 5.1: Specimens in fatigue machine

impossible to successfully record and identify AE from fatigue crack growth. The noise had a broad frequency range, which made it not possible to filter out.

At the end of the experiment, the noise suddenly decreased greatly in amplitude. During this time, some signals were recorded which could be attributed to the failure of the specimen. Since the sensor setup during this test was focused on the initial surface defect, accurate localization of these signals was not possible, since these signals originated near the outer edge of the specimen. The exact source mechanism of these signals could not be determined, because the opening and closing of the through crack could be generating this AE. Therefore, no useful signals have been recorded for comparison with simulated signals.

The source of the noise has not been determined, although the prognosis is that there was a problem with the clamping of the specimen.

5.1.2. FATIGUE TEST #2
During the second test the same setup was used, but greater care was exercised during the clamping of the specimen. The noise during this test was far lower, at a level of 72dB_{AE}, which still turned out to be too high to be able to distinguish AE from fatigue crack growth. When visual inspection of the defect established a fatigue crack had initiated at the defect, effort was made to decrease the noise level by lowering the loading frequency to 1 Hz. Although this did decrease the noise to a level of 57dB_{AE}, still no AE signals were found to originate from the defect zone.

This specimen was loaded until a total crack width of 50 mm, without any sign of useful signals.

5.2. FINITE ELEMENT MODELING
The simulations described in this chapter explicitly do not simulate the actual fatigue process. The AE which is formed during fatigue crack growth is simulated.

5.2.1. MATERIAL PROPERTIES
The material used during the fatigue AE simulations is identical to the material used during the PLB simulation, given in Table 4.1. Although the material condition surrounding the fatigue crack is complex, containing a plastic zone for instance, this is not included in the FE model. The change of acoustic properties in these conditions might not be negligible, but are chosen to not be included in the current thesis.

5.2.2. MODEL OF POINT AND EXTENDED SOURCE
A description of the source models found in literature has been given in Section 2.4. The *point* and *extended* source have a very similar implementation, differing only in specimen geometry. A representation of the point and extended sources have been shown in Figures 5.2a and 5.2b, respectively. Both sources use a node or element, which is excited in *y*-direction.

GEOMETRY
The geometry of the models used to simulate the extended and separation source are shown in Figure 5.3a. The point source model has the same global dimensions as the the extended model, the main difference being the crack geometry not being present in the former, thus enabling a structured mesh. The models make use of a symmetry planes in the *xz* and *yz* plane. The $z = 0$ plane will be referred to as the bottom of the plate. The top of the plate is located at the $z = 5\text{mm}$ plane, in which the opening of the crack will be simulated.

(a) Point source   (b) Extended source   (c) Seperation source
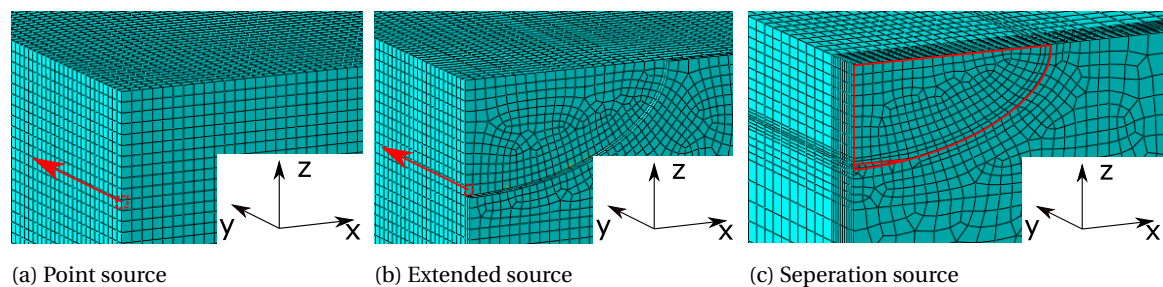
Figure 5.2: Implemented source models
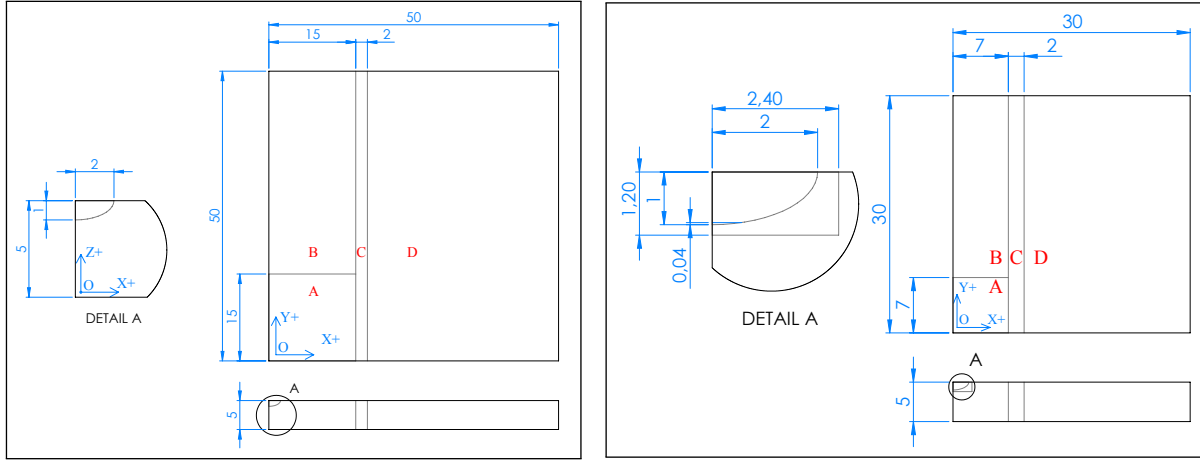
(a) FE model for extended source
(b) FE model for separation source

Figure 5.3: Geometry of FE models

The outer dimensions of the model are chosen such, to allow for a reflection free period which is long enough to allow for the passing of the first few waves at 15 mm. Based on the signals of the PLB simulations, a time window of 15 μs is selected. An approximate speed of $c_L = 5.9$ mm/μs is used for the longitudinal wave. Considering a travel distance of 50 mm to the outer edge, and 35 mm back to the sensor, an arrival time of 14.7 μs can be calculated, which is sufficient.

MESH

A total of four main sections can be distinguished in the models, indicated by the letters A–D in Figure 5.3a. Section A contains the source model and is the area of highest interest. A fine mesh is used in this section, with element edge lengths of 0.1 mm. Section B is meshed with elements using the same dimension in the xz-plane, but the length in y direction is stretched to 0.25 mm. Section C has a transitional mesh, which enlarges the element sizes for the last section, in which a structured mesh with element lengths of 0.5 mm is used. The reason this type of refinement strategy is chosen, is to allow for a semi-fine area in section B, in which signals can be obtained with reasonable signal quality. Also, a three dimensional refinement technique for non-structured meshes is not supported for hexagonal meshes in Abaqus, inciting the need for the presented solution.

Whereas section A has a structured mesh for the point source model, this is not the case for the model with the extended source, since the geometry of the crack needs to be modelled. For each simulated crack depth, a crack with a width/ depth ratio of 4 is chosen. One column of elements is removed from the crack area as a simplified way to model the opening of the crack, making the span of the crack in y direction a total of 0.2 mm.

OUTPUT

Outputs of the models will be a grid of nodes at both the top and bottom of the plane, containing one in every four nodes. This grids with 0.2 mm node spacing will be used to obtain the displacements in z direction, as has been described in Section 3.2.3.

SOURCE DEPTHS

Crack depths are measured from the top of the plate $(x, y, z) = (0, 0, 5)$ [mm], to the crack tip. Depths of 0 mm,1 mm,2 mm are simulated using the point source. Results for crack depths of 3 mm, 4 mm and 5 mm are generated from these results, because of the symmetry in the $z = 2.5$ mm plane.

The extended model was simulated for 1 mm, 2 mm, 3 mm, 4 mm. At a crack depth of 0 mm the point and extended models are identical, so the extended source will not be separately simulated for a crack depth of 0 mm. A crack depth of 5 mm is assumed to be inherently different, since it is the transition between a surface and a through crack, and is not considered in this thesis.

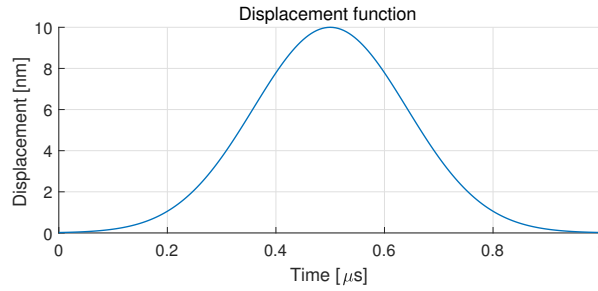$$\delta(t) = \exp\left(-\left((t - 0.5\,T_0)\,\frac{5}{T_0}\right)^2\right) \cdot 10^{-5}\,\text{mm} \qquad (5.1)$$

Figure 5.4: Excitation function

SOURCE FUNCTION

The point and extended source models use a similar implementation. The nodes which are used for excitation, shown in Figures 5.2a and 5.2b, are displaced along the y-direction according to the function described in Equation (5.1). The main simulations for the point and extended sources are performed using a total time duration of $T_0 = 1\,\mu s$, based on the findings in [6]. To be able to observe the effect of a varying T_0 value, point source simulations are also performed using T_0 values of $0.5\,\mu s$ and $2\,\mu s$. The maximum displacement value for all functions is set to an arbitrary value of $1 \times 10^{-5}\,\text{mm}$.

Since hourglassing was observed, which will be described in Section 5.2.4, four displacement nodes (one element) are used instead of a single node.

5.2.3. MODEL OF SEPARATION SOURCE

The modelling of the separation source is somewhat more complicated than that of the point and extended source. The source has been simplified to a certain extend, but is based on the separation source which is described in Section 2.4. The source described by [19] monitors stresses in a certain crack plane, releasing the nodal connections in which failure occurs according to certain criteria. In this thesis it is simplified in the extend that released nodal connections are chosen arbitrarily, to globally match what would be the case in reality.

The global dimensions of the model are given in Figure 5.3b, the section in which the source is located is shown in Figure 5.5. The $x = 0$ plane is subject to x-symmetry ($U_x, R_y, R_z = 0$). The $y = 0$ plane is subject to y-symmetry ($U_y, R_x, R_z = 0$), excluding the crack geometry. Rigid body motion in z direction is prevented by restricting z motion in $(x, y, z) = (30, 30, 0)\,[\text{mm}]$.

PRE-LOAD STEP

The first simulation step is a static step, using Abaqus/Implicit. The model is pre-loaded by a displacement in positive y-direction, applied to the $y = 30\,\text{mm}$ surface. The crack is opened, as shown in Figure 5.5b.

INTERMEDIATE STEP

Following the static pre-load step, the solution needs to be transferred to a dynamic step, in which the actual AE will be simulated. Initial simulations showed that during this transition from Abaqus/Implicit to Abaqus/-Explicit, some differences in the static solution are introduced, which result in unwanted AE waves. In order to prevent this, an intermediate step with mass damping is used, damping out the unwanted AE.

RELEASE STEP

The final simulation step starts with the preloaded model in Abaqus/Explicit. The fatigue crack growth process is now simulated by extending the crack surface with an additional area. This arbitrarily chosen area is shown in Figure 5.5a by the green line at the bottom of the crack. The y-symmetry condition in this area is released. The new crack surface will rapidly accelerate due to the applied pre-stress and elastic properties of the material, generation the AE waves in the process.

LIMITATIONS

The first step in Abaqus/Implicit uses bigger elements than the two following dynamic simulations, since the first step is computationally more intensive. The displacements resulting from the static simulations are transferred to the finer mesh of the second simulation using the *submobel* boundary condition. The way this transfer is done by Abaqus, turned out to be the greatest limit on the possible number of elements. For an
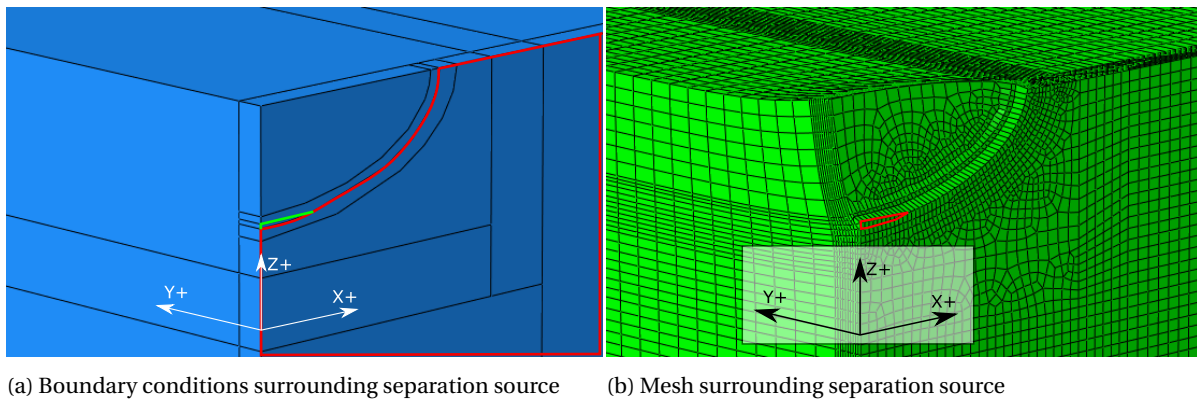
(a) Boundary conditions surrounding separation source   (b) Mesh surrounding separation source

Figure 5.5: Separation source

Table 5.1: Hourglass investigation cases

Case	Load nodes	HG control
1	1	Enhanced
2	1	Viscous
3	1	Enhanced, time scale=0.5
4	4	Enhanced
5	4	Viscous
6	1	Tetrahedron mesh

unknown reason, at some point in the process, a great amount of memory is needed for a short amount of time, for which no backup memory in the form of hard disk space can be used.

To avoid using this method, a script has been written in MATLAB to extract the nodal displacements from the static simulation, and one by one apply them to the transition simulation. Although this process was successful for small models, when it was applied to larger models it became very slow, up to the point where it was not usable. In the end the submodelling method was used, with the limitation on the mesh size.

MESH
The geometry of the used models is shown in Figure 5.3b. The same mesh refinement strategy is used, as was described for the models using the point and extended source. Mesh sizes for section A are 0.15 mm×0.15 mm, increasing the y-edge length to 0.25 mm in section B. Section D has a structured mesh with element lengths of 0.5 mm. Elements surrounding the crack geometry are further decreased in size to combat hourglassing. The total size of the model is 30 mm × 30 mm × 30 mm. Since the fine meshed area is smaller than for the other models, the history output plane has also been reduced. Simulations with crack depths of 0.5 mm, 1 mm and 2 mm are simulated. Increasing the crack depth further was not possible due to the increased area for which a fine mesh was needed.

5.2.4. HOURGLASSING
After the first point source simulations, it became obvious that hourglassing was occurring in the simulations, an effect that has been discussed in Section 3.2.2. This led to investigation in order to minimize this effect. Several element types and hourglass-preventing options in Abaqus/Explicit have been explored, and are summarized in Table 5.1. In all cases an element size of 0.1 mm has been used. The *Load nodes* column refers to the number of nodes which are displaced.

The *enhanced* hourglass control option in Abaqus offers a stiffness based solution for the hourglassing. The *viscous* option, as the name suggest, adds viscosity to prevent the mode. Furthermore it is attempted to use multiple nodes instead of one for the displacement. Also a decrease in timestep is attempted. Lastly, a linear tetrahedron mesh is used, since hourglassing cannot occur using this element.

RESULTS
Figure 5.6a shows the obtained signals at 5 mm distance of the source. Figure 5.6b shows the nodal displacements at 10 μs of the top surface edge at $x = 0$. Clear distortions can be seen for cases 1, 3 and 4. Cases 2

(a) Displacement in z-direction vs. time

(b) Displacement in z-direction vs. location on y-axis
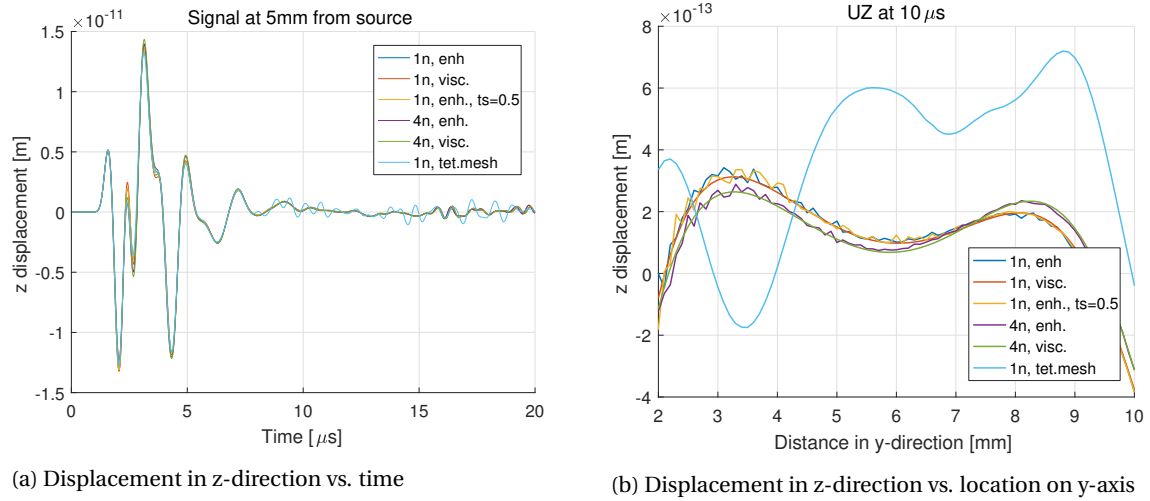
Figure 5.6: Hourglas investigation for Point source

(a) Simulated signals

(b) Coherence with es=0.075 mm signal
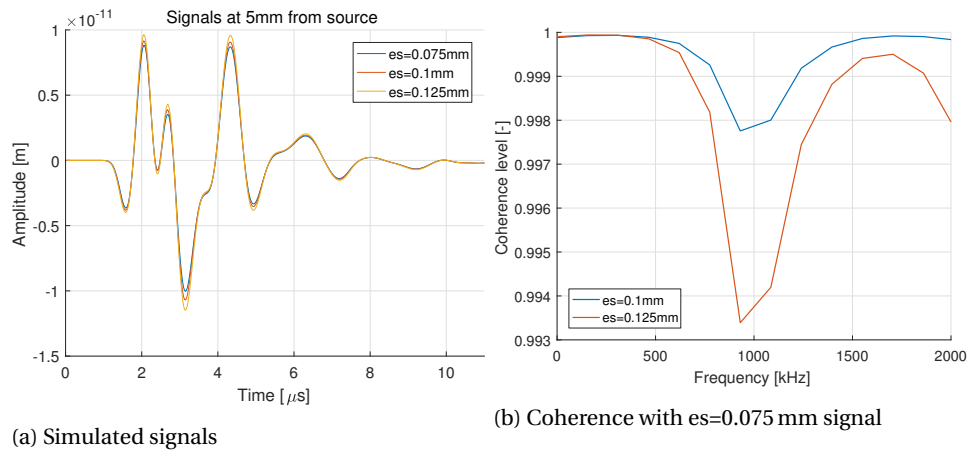
Figure 5.7: Convergence check of Point Source model

and 5, which use a viscous hourglass prevention method seem to perform better in this regard. The tetrahedron mesh used in case 6 also does not show hourglassing, but does show a different solution. The viscous hourglass control method was selected for the fatigue simulations in this chapter, using four nodes for the excitation.

5.2.5. CONVERGENCE CHECK

In order to verify that a sufficiently small mesh size is used to accurately simulate the sources, a convergence check is performed. Bandpass filtered signals of the point source simulation at 5 mm are investigated. The signals are plotted in Figure 5.7a. Mesh sizes of 0.125 mm, 0.1 mm and 0.075 mm are investigated. The coherence of the former two with the latter one have been plotted in Figure 5.7b. Minimum coherence values of 99.3 % and 99.8 % have been found respectively for decreases in mesh size with factors 1.67 and 1.33. The used mesh size of 0.1 mm is deemed sufficient.

Since the separation source simulations are performed with the smallest elements that can be managed, a convergence check with an even finer mesh is not possible. This must be kept in mind during the evaluation of their results.

5.3. RESULTS

The results of the performed simulations are discussed here.

5.3.1. POINT SOURCE

Signals obtained from the point source simulations with a source duration of 1 µs have been plotted in Figures 5.8a and 5.8b. These figures contain the unfiltered signals at a single node and the filtered signals which are obtained using the sensor area. Both sets are obtained at the top surface of the plate at *y*=5 mm. Results of sensors at 10 mm and 13 mm, as well as simulation results of source duration values of 0.5 µs and 2 µs have been shown in Appendix B.1. CW transforms of some of these signals have also been shown there.

(a) Unfiltered signals   (b) Filtered signals
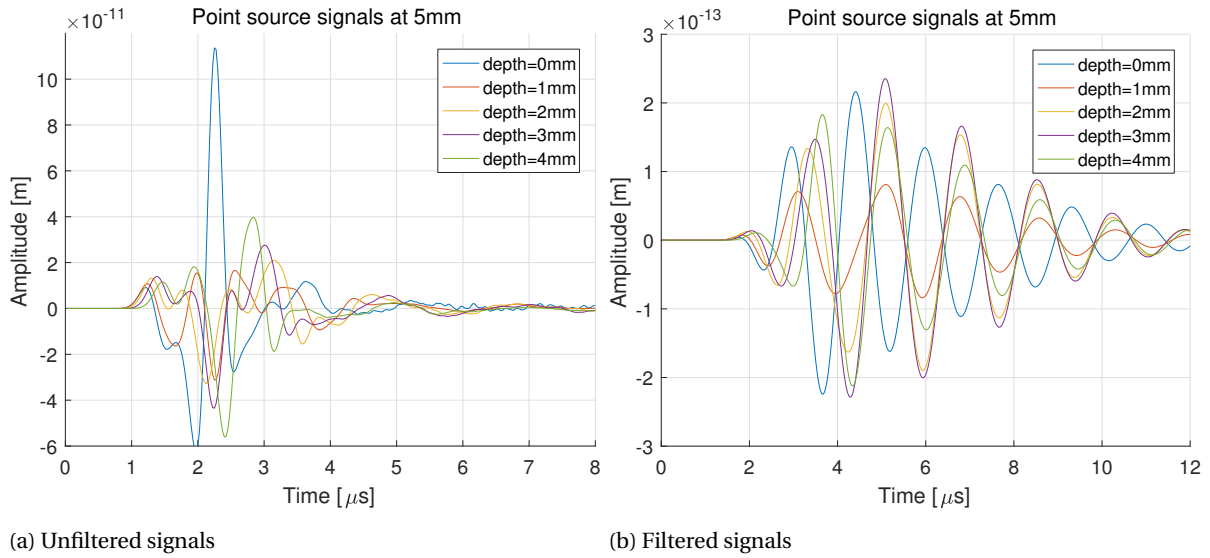
Figure 5.8: Signals of Point Source at different depths, at 5 mm travel distance

5.3.2. EXTENDED

Signals obtaind from the extended source simulations have been shown in Figure 5.9. Figure 5.9a shows the unfiltered results obtained from a single node at the top surface of the plate at *y*=5 mm. Figure 5.9b shows the results of the same location, but filtered and obtained using the sensor area integration. For the 0 mm source depth signal, the point source simulation is used.

(a) Unfiltered signals   (b) Filtered signals

Figure 5.9: Signals of Extended Source at different depths, at 5 mm travel distance

5.3.3. SEPARATION SOURCE

Figure 5.10a shows the 100 kHz highpass filtered signals obtained from the separation source simulations. The highpass filter is applied to filter out an unwanted low frequency wave, resulting from the simulation method. The unfiltered signals are shown in Figure B.9.

Figure 5.10b shows the signals using the same highpass filter, but in this case the signals are obtained using the sensor diameter. This demonstrates that the waves with a wave length much smaller than the sensor diameter are not picked up by it.

Figure 5.10c shows the signals which are obtained by the sensor diameter, and are filtered by the sensor response filter.

Although the general behaviour of AE can be analized using this source funtion, the waves obtained using the separation source are deemed unreliable for time picking and localization purposes. This conclusion is made based on the fact that a convergence study could not be performed. The low frequency wave resulting from the used simulation method is also preventing successful localization. This will be elaborated on in a later section.

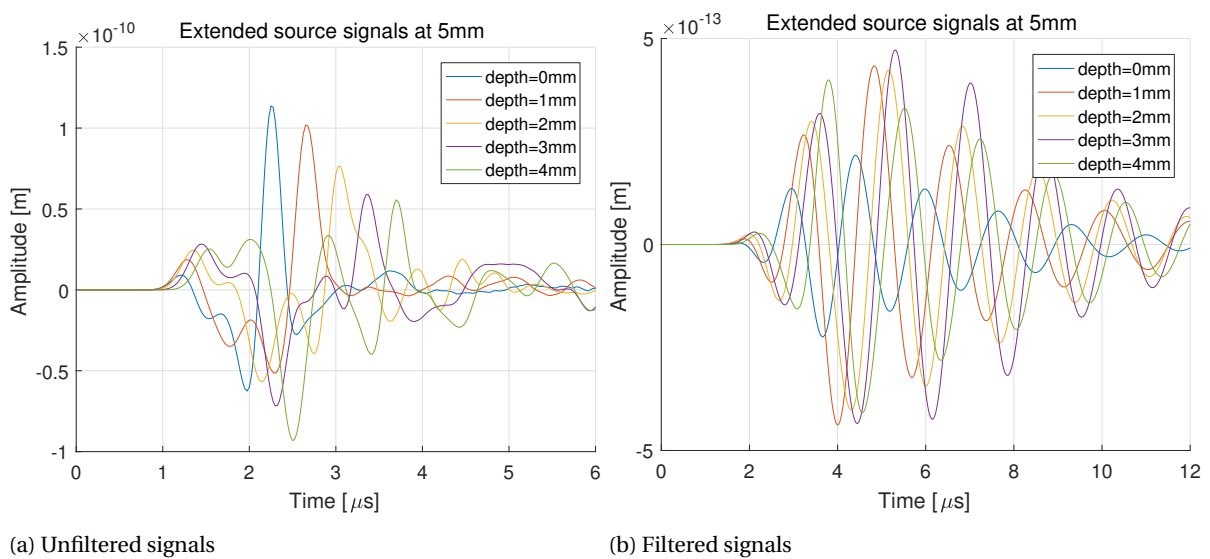(a) Highpass filtered signals   (b) Highpass filtered signals, obtained from sensor area   (c) Sensor filtered signals
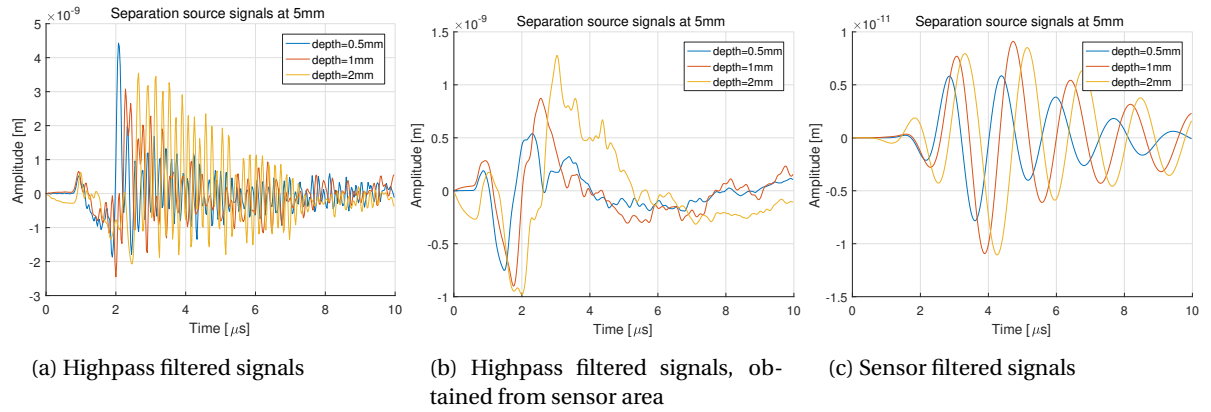
Figure 5.10: Signals of Separation Source at different depths, at 5 mm travel distance

(a) Highpass filtered signal obtained from single node   (b) Highpass filtered signal, obtained from sensor area
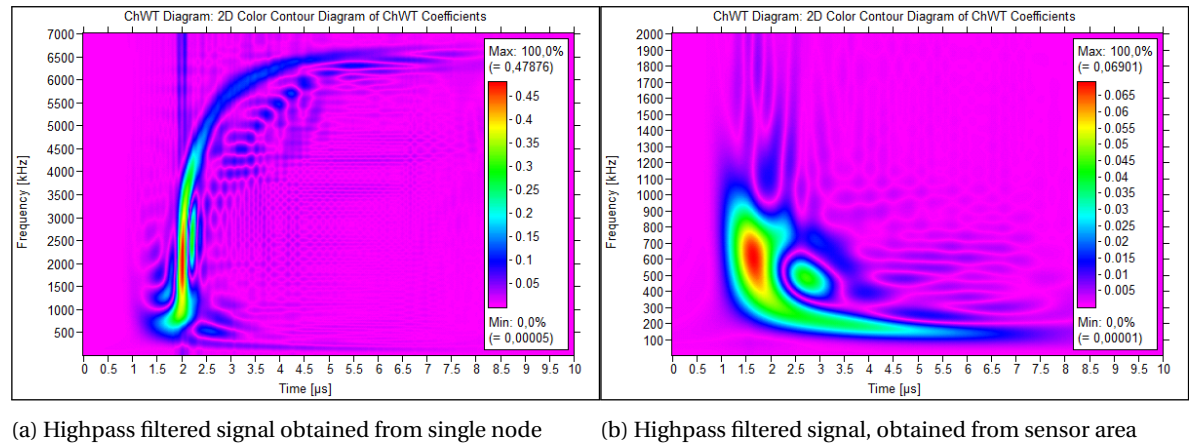
Figure 5.11: Choi-Williams transform of separation source signals at 5 mm distance, 0.5 mm source depth

5.3.4. SOURCE COMPARISON

Figure 5.12 shows the signals of simulation of point source (1 μs), extended source, and separation source, at source depths of 0 mm, 1 mm, 2 mm, 3 mm and 4 mm. The signals have been normalized with respect to their maximum amplitude, to better compare them.

Looking at the global wave forms, it can be concluded that no great differences are present, other than different wave lengths. It should be noted however that in Figure 5.12c, the arrival of the separation source is far earlier than the other two sources. This wave is due to the transition between the damped and undamped simulation step, and should be disregarded.

Source time variation Frequency components of the unfiltered signals resulting from source depths of 2 mm have been shown in Figure 5.13 for all three investigated point source duration values and the extended source. Looking at the point sources with increasing excitation duration (Figures 5.13a to 5.13c), it can be seen that the frequency decreases. This is to be expected, since with an increasing duration, the frequency of the source itself decreases, decreasing the frequency of the resulting waves with it. The 1 µs point source frequency signature (Figure 5.13b) is very similar to that of the 1 µs extended source (Figure 5.13d). It is however slightly higher, and shorter in duration.

Signals generated by the varying T_0 values of the point source simulations have been shown in Figure 5.14.

5.3.5. WAVE TYPES

The wave types that occur in the plate have been investigated. In order to better be able to visualize them, two dimensional simulations have been performed, for the point and external sources. Figure 5.15 shows the Von Mises equivalent stress in two points in time for the point source at 0 mm source depth. Von Mises equivalent stress has been chosen for the fact that it shows both the longitudinal (pressure) and transverse (shear) waves, in all directions.

In Figure 5.15a, it can be clearly seen that the longitudinal waves have travelled further than the transverse waves, due to their vast speed difference. A head wave can also be clearly distinguished. This wave travels along the surface with a velocity equal to the pressure wave. Along its way, it casts a slower transverse wave into the body.

Another type of wave is observable in Figure 5.15b. The Rayleigh surface wave, which travels along the surface with the velocity which is comparable to the transverse wave, still contains a significant amount of energy after the first 7.5 µs have passed. In the simulations of the point source at greater depths (depth≠ 0 mm), this Rayleigh wave was present in a far smaller extend. This is due to the fact that the point source does not contain a free surface for the wave to travel over from the source location to the surface of the plate. In all simulations of the extended source however, the Rayleigh wave was present, since the model of the extended source does have this free surface.

(a) Time = 3 µs

(b) Time = 7.5 µs
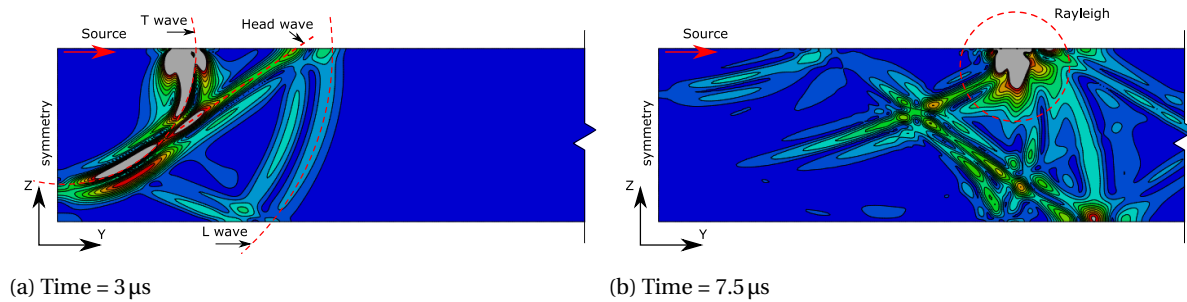
Figure 5.15: Von Mises stress contours in 10 mm steel plate

(a) Depth = 0 mm

(b) Depth = 1 mm

(c) Depth = 2 mm

(d) Depth = 3 mm

(e) Depth = 4 mm

Figure 5.12: Comparison of fatigue source models

(a) CW of point source 0.5 μs

(b) CW of point source 1 μs

(c) CW of point source 2 μs

(d) CW of extended source 1 μs
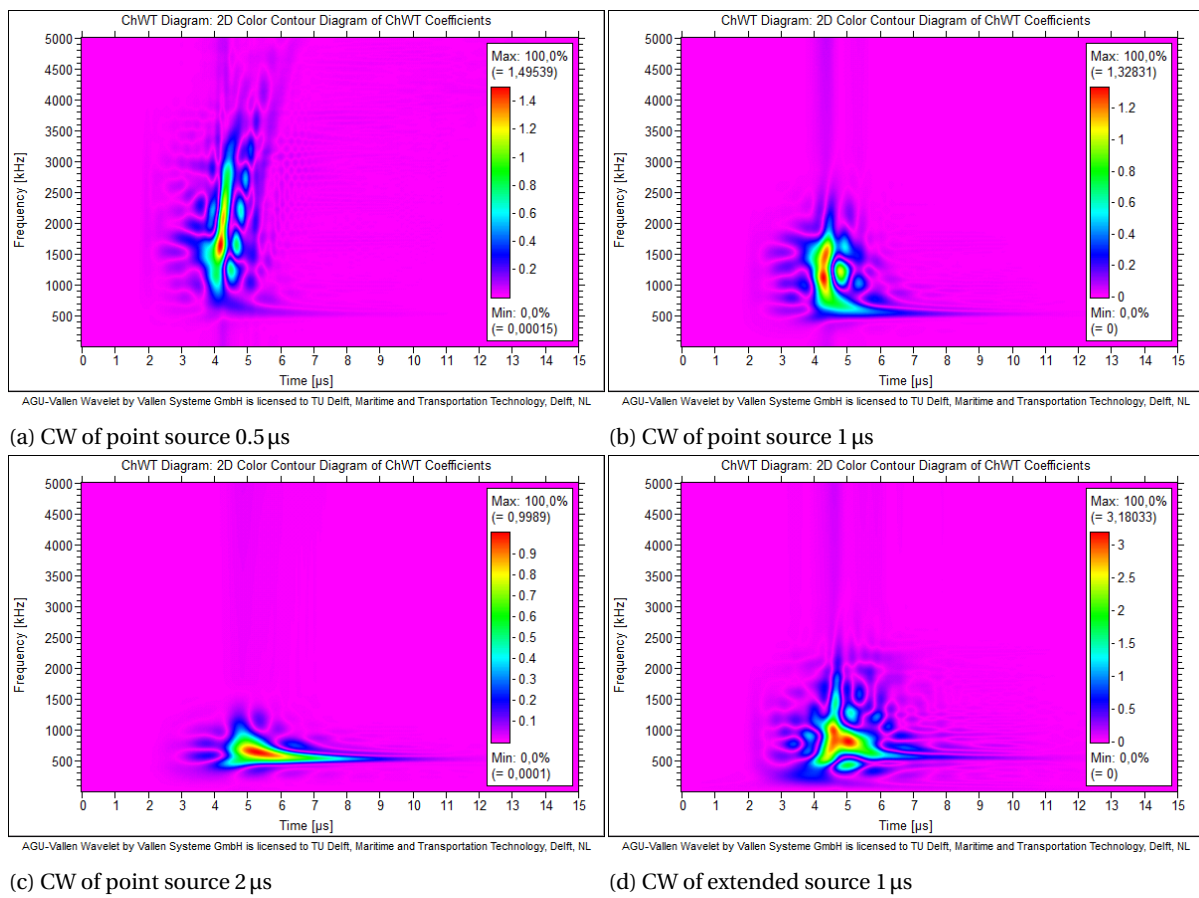
Figure 5.13: Frequency comparison between point sources and extended source at depth=2 mm and 10 mm sensor distance

(a) Unfiltered signals, obtained by single node

(b) Filtered signels, obtained by sensor area
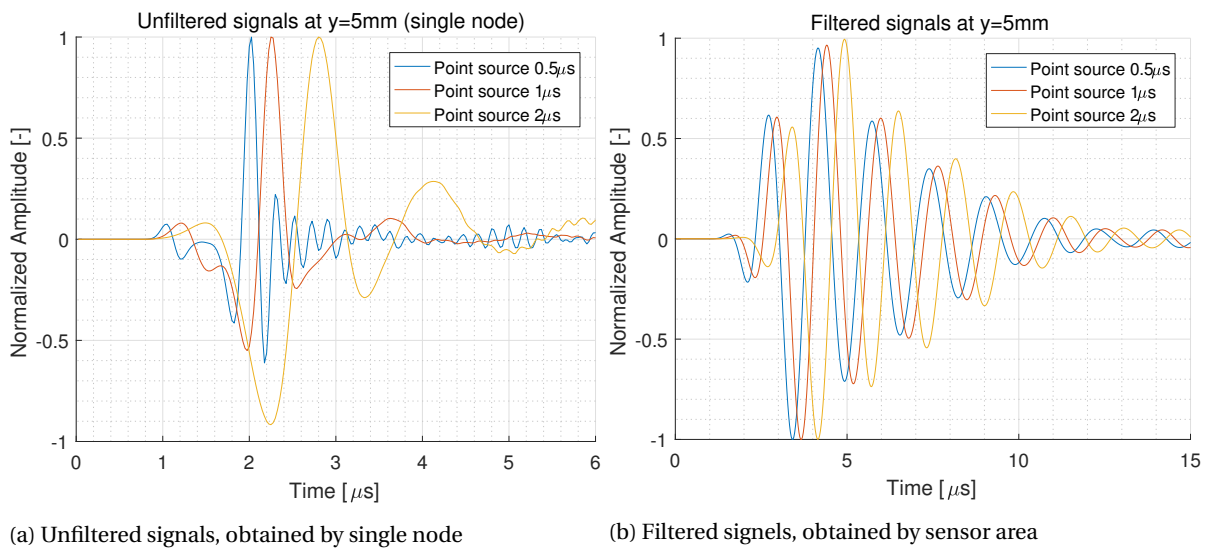
Figure 5.14: Comparison signals of varying point source duration, at y=5 mm and depth=0 mm

5.3.6. PROPAGATION ANGLE

Unlike during the case of PLB simulation, wave formation by fatigue crack growth is not axi-symmetric, so waves in different directions may vary. During localization of an AE source, sensors are placed in varying angles around the source, so the difference between the signals they pick up is relevant. **move figure here**

SIGNALS

To investigate this, signals of the three source functions, obtained at five different angles (α), ranging from 0° to 90°, are plotted in Figure 5.16. A source depth of 1 mm has been used for all sources. The sensors have been filtered with the 100 kHz–1000 kHz bandpass filter and the sensor response filter, but have been obtained with just a single node, to prevent pollution from different angles. Mentioned angles α are measured on the surface of the plate, between the propagation direction and the yz plane. This means a signals with direction $\alpha = 0°$ travel in y-direction, and signals with $\alpha = 90°$ travel in x-direction.

WAVE AMPLITUDE

All three source models agree on the fact that amplitude decreases as angle α increases. Figure 5.17a shows the normalized amplitude decay over α, at 5 mm sensor distance.

WAVE SPEED

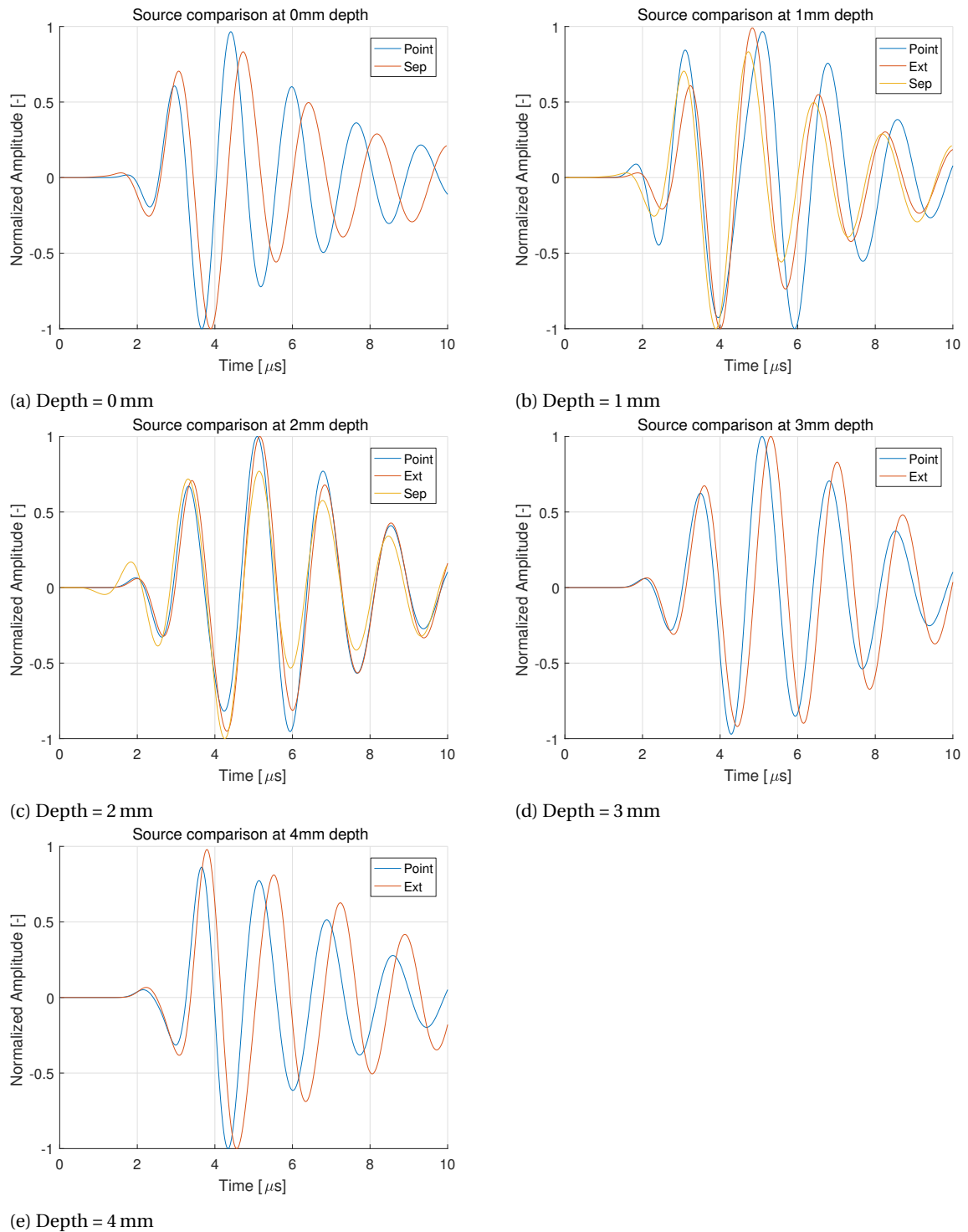Travel speeds in different directions are of interest for time picking purposes. Figure 5.17b shows the arrival time of the first peaks. Again, all source agree on the issue, stating that TOA values of the peaks decrease with increasing α values.

The only value that deviates from this conclusion is the value of the point source at $\alpha = 90°$. This is due to the fact that the signal exhibits a different form than the other signals.

(a) Point source signals at 5mm   (b) Extended source signals at 5mm   (c) Separation source signals at 5mm
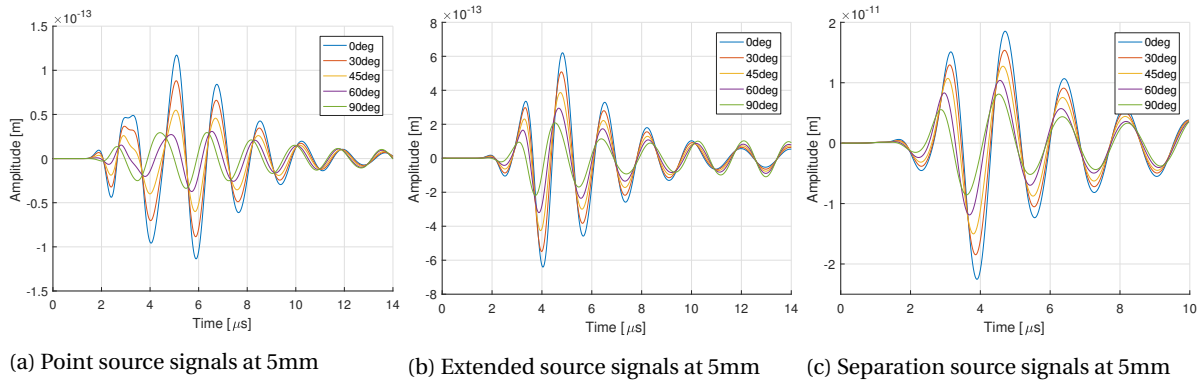
Figure 5.16: Signals at 5 mm for varying propagation angles

(a) Maximum amplitudes   (b) TOA values for first peak

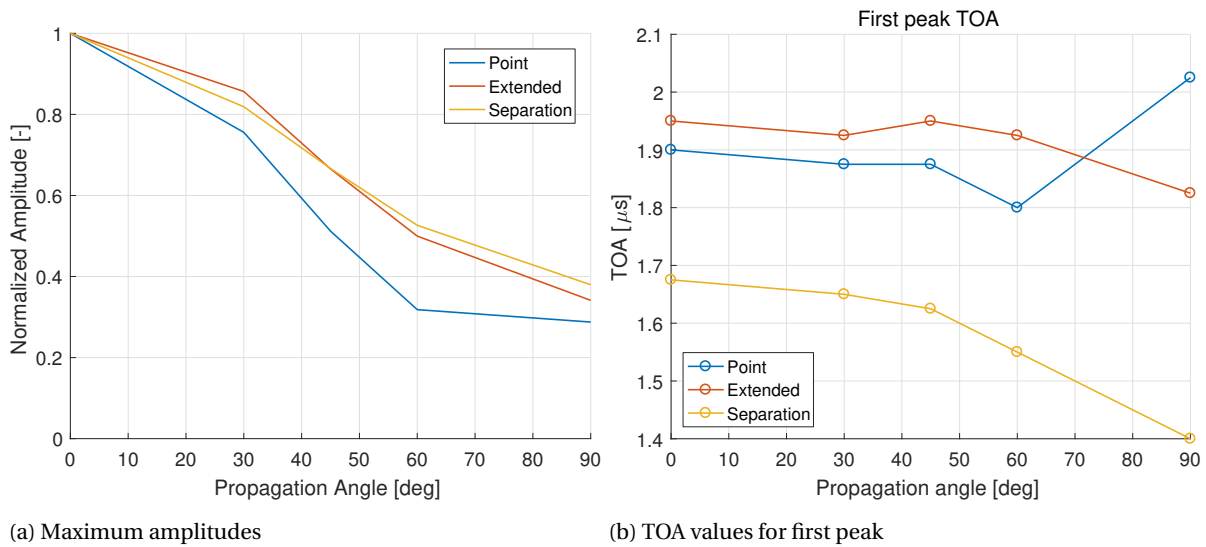Figure 5.17: Maximum amplitudes and TOA of first peaks for signals at 5 mm in varying propagation angles

5.4. TIME PICKING AND LOCALIZATION

In this section it will be investigated what level of localization accuracy can be accomplished for the simulated source models.

5.4.1. NOISE LEVEL

The noise that is encountered during AE monitoring of fatigue cracks will very likely be much higher than during the PLB experiments. This has been learned the hard way during this project, as was described in Section 5.1. A comparable noise level was encountered during AE monitoring of a fatigue test of the TS, by a uniaxial fatigue testing machine in the department of the Aerospace faculty of Delft University of Technology. The Hexapod, which will be used to load the TS specimen, is expected to produce a much lower noise level, due to the differences in the loading mechanism. The exact noise amplitude will however not be known, until the machine is running, and the first AE recordings are performed.

Time picking is highly dependent on the level of noise that is present in the signals. For localization purposes in this chapter, and Chapter 6, the following is taken into account:

- No noise is introduced in the signal itself. The use of random noise is averted to be able to form conclusions based on the actual fatigue AE behaviour. The effect of noise on the signal should be investigated in a separate study.

- The minimum threshold value is chosen at an arbitrary value. This is done to prevent usage of an unrealistically low value. The value of this minimum amplitude threshold is based on signals encountered during fatigue testing reported in [26].

5.4.2. SPEED

During localization of PLB's the sensors lay in plane with the source. Wave speed could easily be calculated using two sensors in a straight line with the PLB. The distance between these to sensors was divided by the TDOA. The obtained speed was used for localization. Localization using this *surface speed* is less effective when the source does not lie in the same plane as the sensors, which is the case during fatigue. The surface speed of a certain characteristic might deviate from the speed it travels *through* the material.

To further explain this effect, Figure 5.18 is used. Suppose the AE source lies at the crack tip in point A, for which the depth *a* is unknown. For the sake of this example, the TOA of the signal will be determined by an infinitely small amplitude threshold crossing. This effectively results in a TOA related to the arrival of the first longitudinal wave, traveling at a constant theoretical speed of approximately $c_L \approx 5.9 \, \text{mm/µs}$. For simplicity is will be assumed that the waves travel in equal speed and amplitude in all directions. The surface speed calculated using these two sensors will be $\frac{dy}{TOA_2 - TOA_1}$. Since the travel direction does not lie in line with the two sensors, a different speed will be calculated than the actual speed of the longitudinal stress wave. Although most TOA characteristics do not have such a distinctive travel speed through the material, since they are the result of multiple factors, a comparable effect may be assumed for those. It can be concluded that even in this ideal case, this method will not result in a correct wave travel speed. It might however be used as a useful approximation.

LOCATION SPECIFIC SPEED

Apart from the determination of surface speed, here a second way of speed determination is proposed which makes use of the fatigue crack growth AE simulations. This method takes the TOA of a certain signal characteristic (threshold crossing, peak, HC, etc), and compares its values at one sensor location for several source depths. For each depth this will result in a TOA and an euclidean distance. Using the different data points, a mean speed can be determined for that particular characteristic.

An example has been shown in Figure 5.19 for source depths of 0, 1, 2, 3 and 4 mm. A sensor surface distance of 5 mm is used, resulting in a 5 mm minimum, and a $\sqrt{5^2 + 4^2} \approx 6.4 \, \text{mm}$ maximum euclidean distance. Using this data, a mean speed (dashed line) is determined, which can used for localization.

This method of speed determination will be referred to as *location specific* speed, since it varies not with crack depth, but does with sensor location. The effectiveness of this speed determination will be investigated.
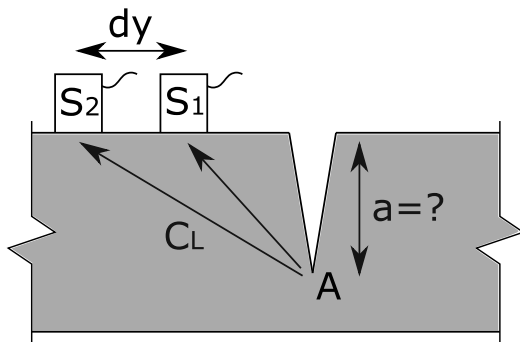
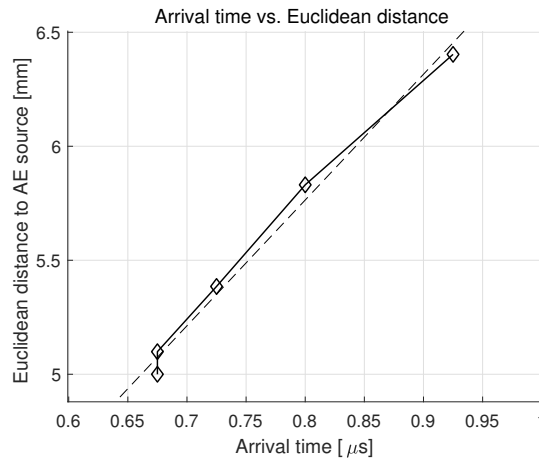Figure 5.18: Visualization of speed determination by two sensors

Figure 5.19: TOA of different source depths at single sensor location
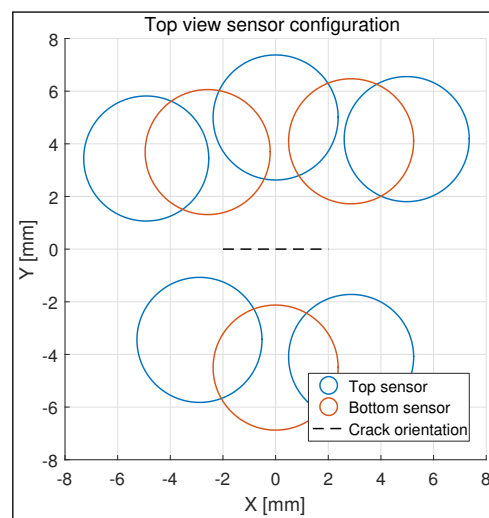
Figure 5.20: Sensor configuration for fatigue AE source localization

5.4.3. LOCALIZATION ACCURACY
Here will be investigated whether the AE sources can be localized with sufficient accuracy.

SENSOR CONFIGURATION
In order to do this, a certain sensor setup is used to test the fatigue source simulations. The setup makes use of five sensors on top, and three on the bottom of the plate, at a distance of roughly 5 mm. These sensor distances are slightly varied in order to replicate a more realistic configuration. Just like in the PLB localization, the assumption is made that the sensor locations are exactly known. In reality, this will not be the case, certainly not when sensors on both sides of the plate are used, which makes it very hard to measure the relative distances. The sensor arrangement is shown in Figure 5.20.

WAVE SPEED DETERMINATION
First, the location specific speeds of the sources are determined. The signals which are used for this are shown in the left hand graphs of Figure B.12 in Appendix B.1, along with the chosen amplitude threshold, the TOA of threshold crossings (Thr), first peaks (peak), Hinkley criterion (HC) and Baer & Kradolfer (BK). The right hand graphs in the same figure plot the picked TOA's against the Euclidean norm of the distance between the sensor and the source, as well as the best fit for a linear speed determination, as has been described in Section 5.4.2. The threshold is chosen such, that the first peak is avoided, realistically this wave might be too low in amplitude to pick up for every sensor.

Now the location specific speeds have been determined, the signals which are picked up at by the sensors are generated. Apart from the eight sensors shown in Figure 5.20, a ninth sensor is used at (x,y) = (0,10)mm

at the top surface of the plate. Together with sensor # 1 at (x,y) = (0,5)mm, this sensor is used to determine a realistically obtainable surface speed. This sensor has not been used for the determination of the LUCY value.

Figures B.13 to B.16 show the generated signals, with an indication of their TOA's. In some cases there is a double threshold visible, this is done to avoid picking a wrong TOA for the signal of sensor # 9, which determines the surface speed. Again, effort is made to not pick the first wave, and also not to pick a peak which just barely crosses the threshold. When such TOA's are picked, this would consist of luck (or bad luck), which cannot be consistently reproduced for different sensor setups. The avoiding of the threshold values according to the here mentioned criteria, is deemed realistically possible, although this might involve human judgment for each signal.

LOCALIZATION RESULTS OF POINT AND EXTENDED SOURCES

Now that we have determined the wave speeds c, TOA values t_a, sensor locations S, the most likely source location can be determined by finding the location with the lowest LUCY value (Equations (2.18) and (2.19)). The resulting localization errors are plotted in Figure 5.21. The error is determined by the euclidean distance between the simulated source coordinate, and the calculated source coordinate.

The first conclusion that can be drawn is that with both the use of surface speed and location specific speed the HC function performs less stable than the threshold and first peak time pick criteria. Furthermore, localization using the localization specific speed seems to be more accurate than when the surface speed is used. Generally it can be stated that for all investigated source functions, usage location specific speed leads to a localization error of approximately 0.4 mm. For the surface speed this is roughly 0.6 mm.

5.5. CONCLUSIONS

Unfortunately, the experimental effort yielded no useful signals to be used for the verification of the source models. For this reason three source models have been simulated, which have all been evaluated. The point and extended sources proved more reliable in terms of convergence and cleanliness of the signal. The simulation of the separation source was not without obstacles, and was not deemed a complete success. The signals simulated with the separation source have, along with the other two source models, been used to investigate global behaviour of AE, but not for localization.

The localization of the point and extended source have been successfully carried out, resulting in errors of approximately 0.6 mm when surface speed is used, and 0.4 mm when the newly proposed location specific speed is used. Time picking was most effectively using threshold and peak characteristics, rather than the HC. BK and MA did not result in useful results. the AIC picker was not used.

The resulting accuracy is within the set goal of 1 mm. It should be noted that only a single sensor configuration was used, while other configurations might prove more useful. The locations of the sensors were exactly known however, which is not the case in actual test, which decreases the localization error. Also, a good signal to noise ratio has been assumed.

(a) Point source 0.5 μs, surface speed

(b) Point source 0.5 μs, location specific speed

(c) Point source 1 μs, surface speed

(d) Point source 1 μs, location specific speed

(e) Point source 2 μs, surface speed

(f) Point source 2 μs, location specific speed

(g) Extended source, surface speed
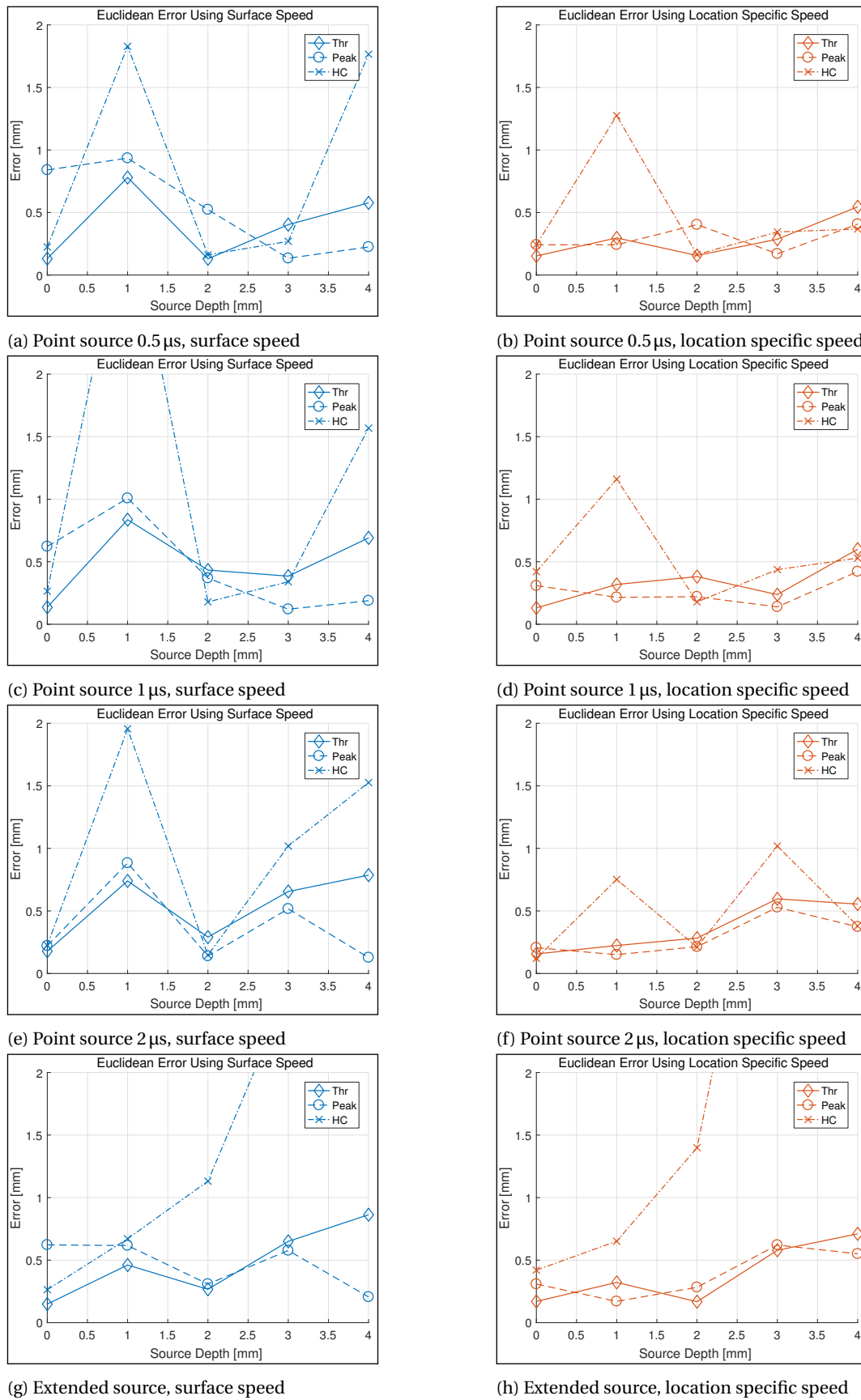

(h) Extended source, location specific speed

Figure 5.21: Euclidean norm of location error for the several source functions

6

INFLUENCE OF LOCAL GEOMETRY

In this chapter the effect of complex geometry near the AE source is investigated. Fatigue is a very common phenomenon near welds. Material properties change due to the heat introduction during welding, making it more susceptible to fatigue. The change in geometry also introduces stress concentrations. The 4D-Fatigue JIP initially investigates two types of specimens: the *Tubular Specimen* and *Bar Specimen*. For the simulation in this chapter the tubular specimen (TS) is selected, due to its likeliness with a plate, albeit a curved plate with welded on flanges. The goal of this chapter is to investigate the effect the reflections of the geometry have on the possibility of crack front localization. In order to simplify the FE model, the crack growth will be simulated using a point source, without modelling the crack itself. An impression of the TS is shown in Figure 6.1, fatigue will be investigated near the flanges in the middle of the specimen.

6.1. FINITE ELEMENT MODELS
The investigation of the effect of flanges will be done using two different models: one with, and one without the flanges. Deviating from the previous chapters where two symmetry planes could be used, here only a single symmetry plane can be used due to the flange at one side of the crack. This, along with the fact that the thickness of the specimen is twice as big, places serious limitations on the possible mesh size. It is even further limited by the fact that the interest of these simulations lie not only with the localization of the source, but also the possible waves reflecting from the flange. Because of this, the model boundaries should be far enough from the source to allow for reflections of the flange, before reflections from the boundaries arrive.

GEOMETRY
The geometry of the used model is shown in Figure 6.2. The free boundaries in positive and negative y direction are located at 50 mm, as is the radial distance of the boundary in positive x direction. Assuming a sensor distance of 5 mm, the waves have to travel 50 mm to, and 45 mm back from the boundaries, resulting in a total edge-reflection travel distance of 95 mm. Assuming an approximate longitudinal and transverse wave speed of $c_L = 5.9\,\mathrm{mm/\mu s}$ and $c_T = 3.2\,\mathrm{mm/\mu s}$ respectively, these reflections will arrive at 16.1 μs and 29.7 μs. Since
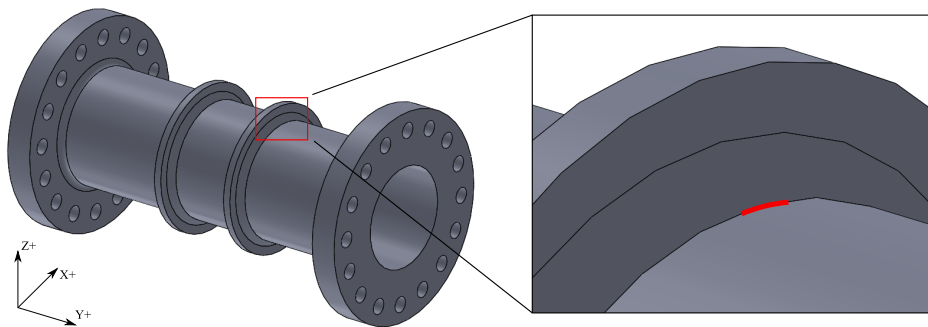

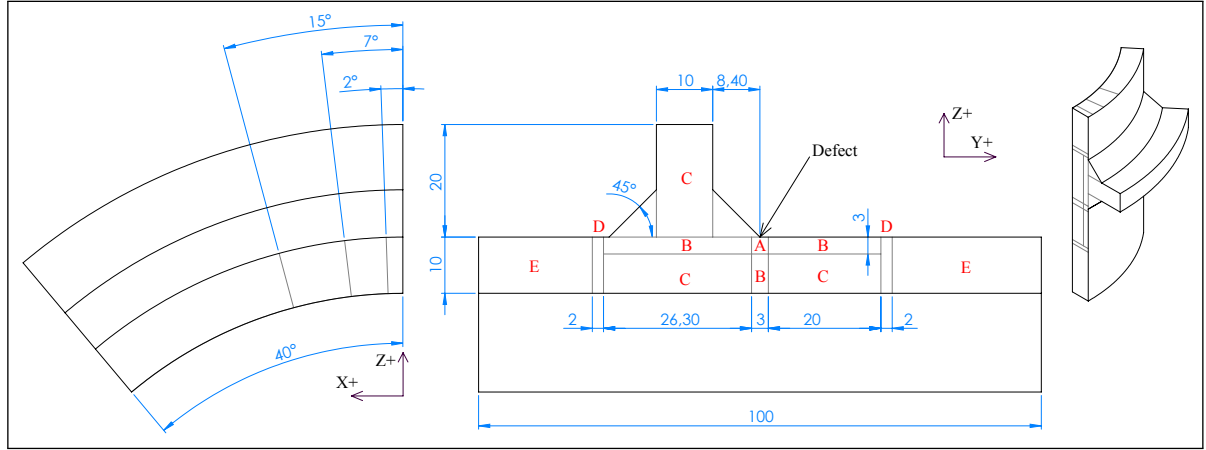Figure 6.1: Tubular specimen and location of defect

59

Figure 6.2: FE model geometry

the longitudinal wave contains a significant amount less energy, the latter mentioned time will be used as an indication for the end time of the simulations.

MESH

The section view in Figure 6.2 indicates the mesh sizes used in that particular plane by the letters A to E. Element lengths of 0.125 mm × 0.125 mm are used at the AE source (section A), propagating to the left, right and bottom (sections B) using lengths of 0.25 mm × 0.125 mm. The two areas connecting these three sections, as well as the flange section (sections C) have a mesh size of 0.25 mm × 0.25 mm. Traveling further outward, two transition areas (sections D) enlarge the mesh to a height of 0.4 mm, so the outer two areas (sections E) can use sizes of 0.4 mm × 0.4 mm. This section cut is revolved around the centre of the TS, using element extrusion lengths of 0.125 mm, 0.25 mm, 0.4 mm and 1 mm, in the sections until 2°, 7°, 15° and 40° respectively, as seen in the left view of Figure 6.2. As the source is modelled deeper into to the specimen, the area of 3 mm × 3 mm (section A) containing the finest mesh size, is moving along with the source.

SOURCE MODEL

The source model used for the simulations is the point source with a duration of 1 µs, as described in Chapter 5. Usage of the separation source was not possible, since the model is too large in size. As has been described, the TS model can not be reduced in size in order to accommodate the usage of this source. The extended source was also abandoned, since the modeling of the crack surface would involve a far more complicated model and mesh refinement technique.

For the TS model, source depths of 0 mm to 10 mm, with steps of 1 mm, are simulated. The flangeless TS model (TSFl) is only simulated at 0 mm and 2 mm. A source depth of 0 mm was found to be the case most susceptible to high amplitude reflections from the flange. The TSFl source depth of 2 mm was simulated as extra comparison.

MATERIAL PROPERTIES

The same material properties have been used for the TS simulations as in the previous chapters, the values of which are listed in Table 4.1. The TS is fabricated from a solid piece of steel, so weld material and a heat affected zone are not actually present. In this chapter, when the reference is made to a 'weld', the weld *geometry* is what will be referred to.

6.2. RESULTS

6.2.1. SIGNALS

Resulting signals of the simulations are plotted in Figures 6.3 and 6.4, the first of which contains the unfiltered signals at the outer surface, at a sensor distance of 5 mm. The second mentioned figure shows the same results, but filtered with the 100 kHz – 1000 kHz bandpass filter, the sensor response filter and the sensor surface area.

Comparing these signals with the point source signals shown in Chapter 5, one aspect is worth mentioning. The amplitude dip at the source depths 1 mm and 2 mm, which is more clearly observable in Figure 6.5.
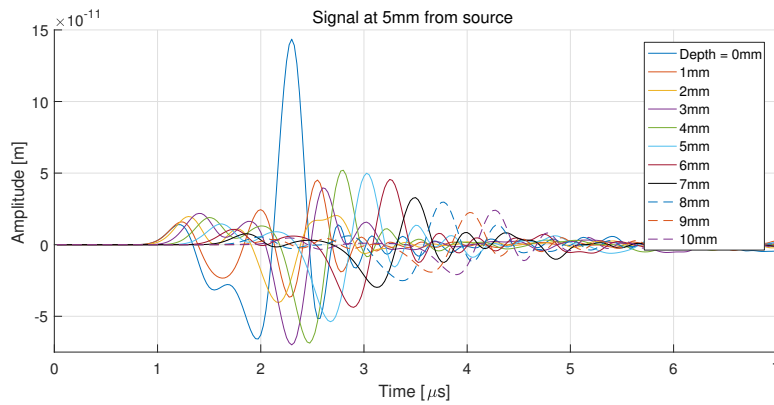
Figure 6.3: Unfiltered signals at 5 mm distance on outer surface
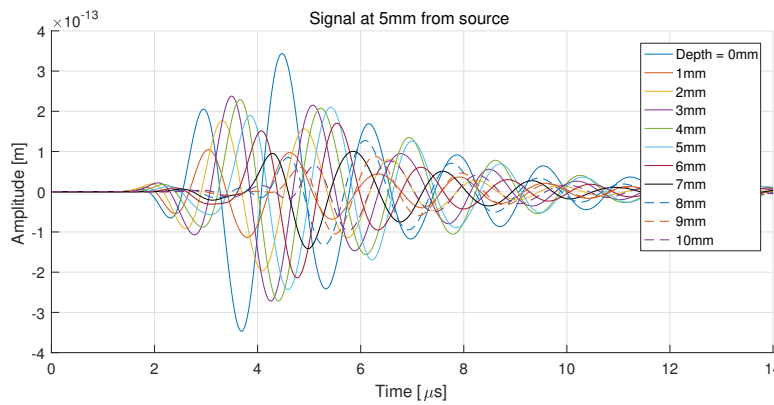
Figure 6.4: Filtered signals at 5 mm distance on outer surface

This figure shows the maximum amplitudes of the signals shown in Figure 6.4, as well as the signals obtained from the same simulations with a sensor on the inner surface. A clear dip in amplitude can be seen at source depths of 1 mm and 2 mm. This dip was also seen in the 5 mm plate, but only when using the point source, and not at the extended or separation source. The amplitude decrease is regarded as an effect of the used source model, and not as a physical phenomenon. What actually is happening here, is not a sharp decrease in amplitude for the 1 mm and 2 mm source depths, but a increase of amplitude for the 0 mm source depth simulation, since in this case a Rayleigh wave can travel over the surface, increasing the amplitude at the outer surface.
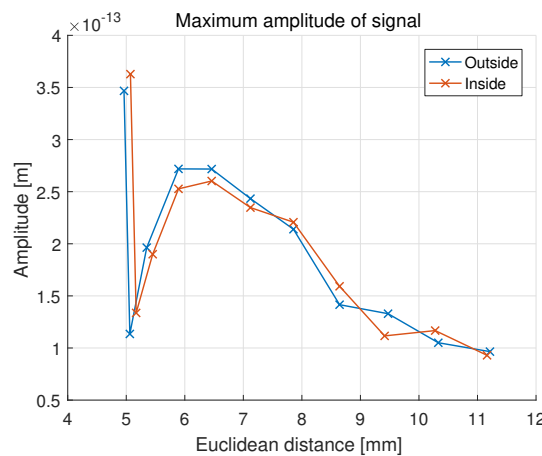
Figure 6.5: Maximum amplitudes of signals at 5 mm on outer surface

6.2.2. EFFECT OF FLANGE

The main question to be answered for the TS, is whether the reflections will have a significant effect on the accuracy of the localization of the AE source. In order to do this, Figure 6.6 shows the signals of sensors located on the inner surface at $y = \pm 5$ mm for the TS and TSFl model. Since the TSFl model has a symmetry plane around the $y = 0$ plane, only a single signal is shown.

Filtered signals   Looking at the filtered signals in Figure 6.6a, two notable differences can be seen between the TS and TSFl signals. Firstly, the amplitudes are somewhat different, which is mostly notable at the first arriving waves. The underlying reason for this will be discussed later on. Secondly, at around 15 μs there are waves present in the TS signals, while not in the TSFl signal. The most likely explanation is that these are reflections arriving from the flange, since the models are identical in every way but the flange.

Unfiltered signals   The same waves are shown in Figure 6.6b, except these are the unfiltered versions. Although these signals are unfiltered, they are obtained using integration of the sensor area, in order to better be able to link them to the Von Mises plots later on. In this plot the difference in amplitude between the TS and TSFl simulations, which was mentioned earlier, is also observed, but is better noticeable over the whole duration of the first wave passing, which in turn is much shorter. The hypothesis for this difference is as follows. Due to the presence of the flange, there no longer is a symmetry at the $y = 0$ plane. Since the excitation is done by a displacement rather than a force, more energy is introduced in the negative y direction than in the positive y direction. The asymmetry in this stress distribution results in an asymmetric wave generation.

The supposed reflections from the flange are less pronounced, but clearly noticeable in this plot, from approximately 13 μs and onward. Additional to these reflections, a slight amplitude difference can be seen from 7.5 μs and onward, although this is less clear than the aforementioned reflections at 13 μs.

VON MISES STRESS CONTOURS

To verify the origin of these supposed reflections, and to gain further knowledge of the behaviour of stress waves in the TS, the Von Mises equivalent stress is is plotted for the $x = 0$ plane. The resulting contours are shown in Figure 6.7. Likely locations for sensors are indicated by the grey rectangles, the bottom two of which indicate the sensors referred to when Figure 6.6 was discussed. The sensors are shown to be able to link them to the signals in Figure 6.6b. When relating the stress plots to the signals, the unfiltered signals in Figure 6.6b will be referred to, rather than the filtered signals in Figure 6.6a, since the shown stress contours are unfiltered as well, and because the filtering is accompanied by a phase shift. The stress magnitudes are varied in each plot, in order to maximize visibility of the waves, rather than to display the correct magnitude.

2 μs Looking at Figure 6.7a, the two wave fronts which are expected can indeed be observed. The yellow line indicates the longitudinal wave, which travels at a higher speed than the transverse wave, indicated by the magenta line. The bulk of the first longitudinal wave is just about to hit the bottom sensors, which is in line with the signals in Figure 6.6b. The bulk of the transverse wave is almost hitting the centre of the outer surface sensor, this signal is shown by the first line in Figure 6.3, which confirms this state.

3 μs The first reflection of the longitudinal wave has hit the bottom surface of the plate. This reflection is expected to consist of both a new longitudinal and transverse wave. Judging from the speed of the wave which can be distinguished in the plot, the bulk of the energy has been converted in the latter wave type. In this figure a special type of wave can also be observed. At both fronts, at the surface of the specimen, a stress wave can be seen ranging from the longitudinal wave, diagonally down to the transverse wave. At the surface this wave propagates with the speed of the longitudinal wave, but slows down when propagating in the body. These are the properties of a head wave, described in Section 2.1. Slightly observable is also the effect of the bigger wave components traveling to the upper left and lower right, which relates to the difference in amplitudes between the initial signals at the $y+$ and $y-$ sensors at the inner surface.

4 μs A small reflection can be seen in the corner between the flange body and the weld. When the longitudinal wave passes this point, a sudden change of resistance (or impedance) is encountered, resulting in this reflection. As was seen in the reflection at 3 μs, most of the energy has been converted to transverse waves. At this point in time, the bulk of the wave is at the inner $y-$ sensor, while the wave with greater energy is only half way the inner $y+$ sensor. This relates to the signals shown in Figure 6.6b.
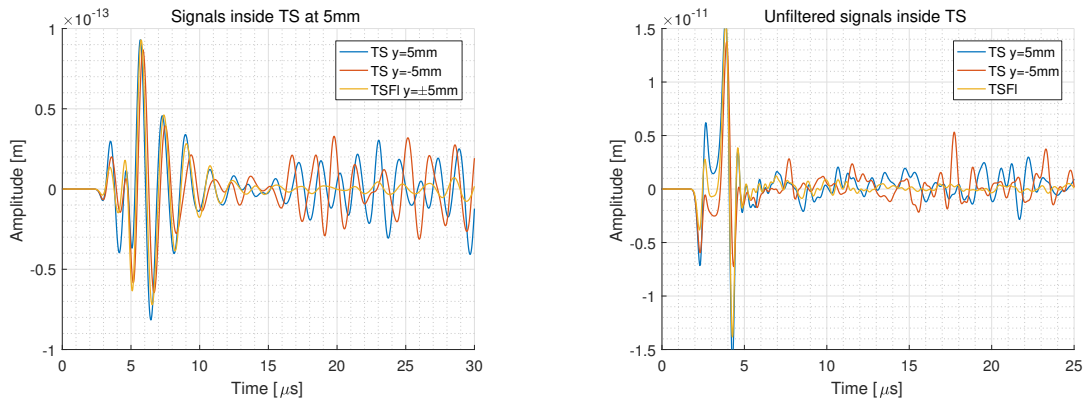
(a) Filtered signals

(b) Unfiltered signals

Figure 6.6: Comparison of filtered signals with and without flange

(a) t = 2 μs

(b) t = 3 μs

(c) t = 4 μs

(d) t = 5 μs

(e) t = 6 μs

(f) t = 7 μs

(g) t = 8 μs

(h) t = 9 μs

(i) t = 10 μs
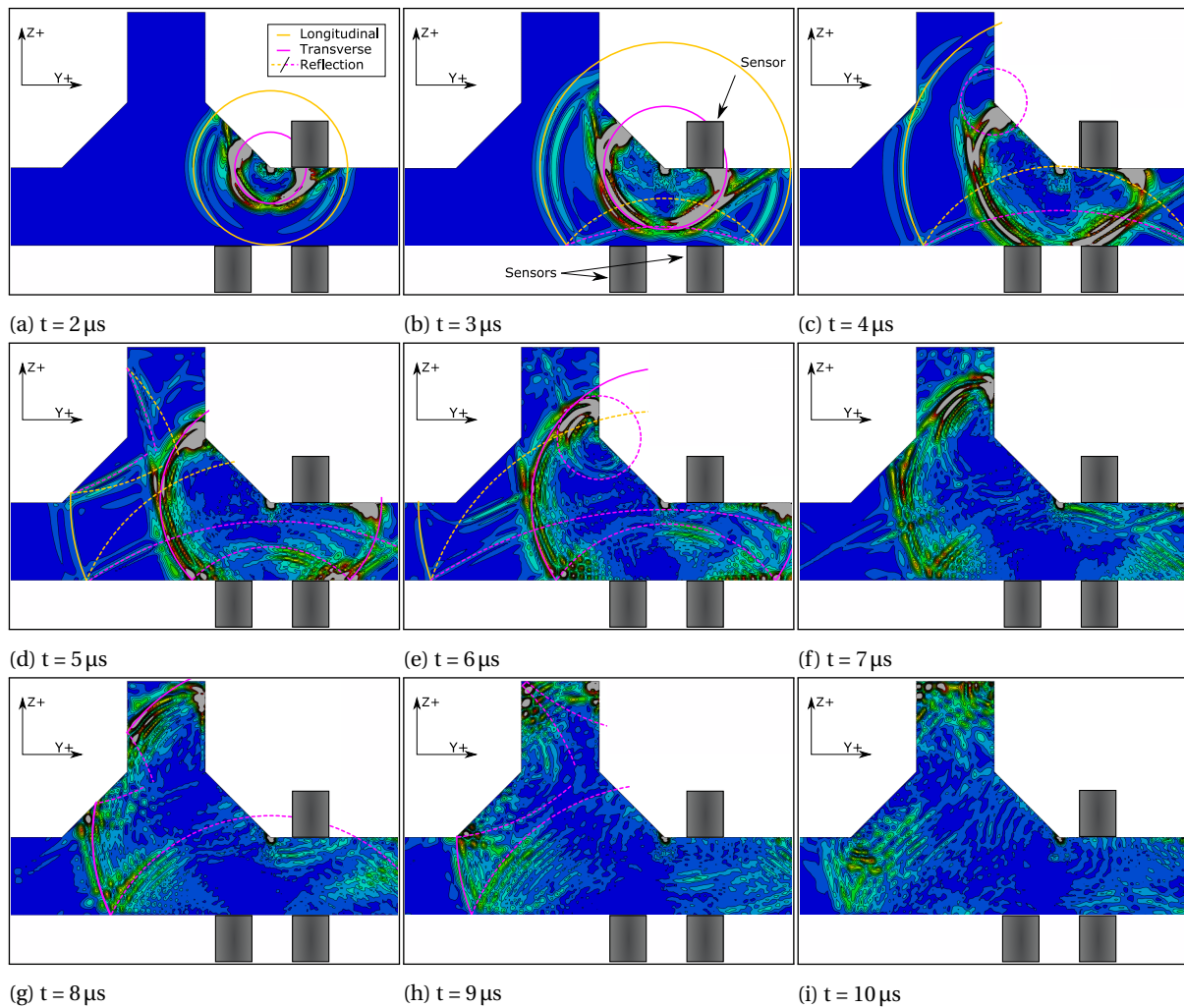
Figure 6.7: Von Mises equivalent stress contours at 2 μs to 10 μs

5 μs The first reflections of the opposite weld surface are visible. As was the case before, this longitudional wave has transformed in a transverse wave.

6 μs Now the transverse wave has passed the flang/weld corner, a new reflection can be seen, similar to the one observed at 4 μs.

7 μs In this point in time, it can be seen that there is a significant amount of energy, which travelled over the surface of the weld, to the surface of the flange. This is most likely a Rayleigh surface wave.

8 μs The bulk of the transverse wave has reached the outer edge of the flange. Some reflections are returning from the weld on the opposite side.

9 μs Reflections of weld surface are better distinguishable. The reflection of the outer flange surface is lacking behind however. This is due to the fact that the dashed line is considering a straight travel path, while in reality the wave needed to travel around the geometry of the weld.

10 μs Energy returning from the outer flange surface is somewhat better observable.

The analysis of the Von Mises plots showed that they are relatable to the shown signals in Figure 6.6b, and behave like was expected. A notable mention being the reflection due to the passing of a corner. Based on this information, three reflection paths have been determined, shown in Figure 6.8. Path 1 is the wave that travels to the opposite weld surface and gets reflected. Path 2 travels over the surface of the weld and flange, before it is reflected back over the surface of the flange, and through the body, to the bottom sensor. Path 3 derives from the same original wave as the reflection of path 2, but gets reflected at the first encountered corner. Paths 1 and 2 have an approximate length of 43 mm, whereas path 3 has a travel length of 30.5 mm. Reflections following path 3 arrive earlier, but are also expected to be of lower amplitude.

Using the approximate speeds of $c_L = 5.9$ mm/μs and $c_T = 3.2$ mm/μs, the arrival times in Table 6.1 can be calculated. To anticipate for the possibility of longitudinal waves reflecting back as transverse waves, the travel distance is split up to a) the distance to the reflecting boundary, and b) the distance it travels back. The TOA values in the column named 'Long./Tranv.' use speed c_L for the former, and speed c_T for the latter.

From Table 6.1 it can be concluded that the first reflections arriving at the sensors arriving as soon as 5.2 μs. The amplitude of these reflections are however negligible, since these are the longitudinal reflections of longitudinal waves. These kind of reflections have barely been observed in the Von Mises plots. The reflections of longitudinal waves returning as transverse waves arrive as soon as 7.8 μs. This seems to match with the data shown in Figure 6.6b, since a slight difference in amplitude can be observed between the TS and TSFl data. The bulk of of the reflected waves should however originate from the transverse wave reflections. According to Table 6.1 these should not arrive earlier than 9.5 μs, although the biggest of these reflections is expected to travel along path 1 and 2, arriving from 13.4 μs. This is is consistent with the observed reflections in Figure 6.6b.

Since the first possible reflections arrive at 5.2 μs, which is after the waves have passed as seen in Figure 6.6b, it can be concluded that reflections do not have an effect on crack front localization in the TS.

Table 6.1: Travel distances and arrival times of reflections

Path	Distance [mm]		Calculated TOA [μs]		
#	To edge	From edge	Long.	Long./Transv.	Transv.
1	20.2	22.8	7.3	10.5	13.4
2	23.5	30.3	9.1	13.5	16.8
3	11.9	18.7	5.2	7.8	9.5

6.2.3. TIME PICKING AND LOCALIZATION

One of the main goals in this thesis is to determine the possibility of fatigue crack growth AE source localization. This has been investigated using multiple source functions in a 5 mm in Chapter 5. This section will use a single eight-sensor setup to determine what degree of accuracy can be achieved using the sensor setup shown in Figure 6.9. Since the TS is used as a subject, the sensor location possibilities are limited by the weld geometry and flange at one side of the crack. Using a sensor setup with only sensors on the outer surface is out of the question, since only three sensors can be positioned at a ~5 mm distance. To obtain sensible results, five bottom sensors are used in addition to the mentioned surface sensors.
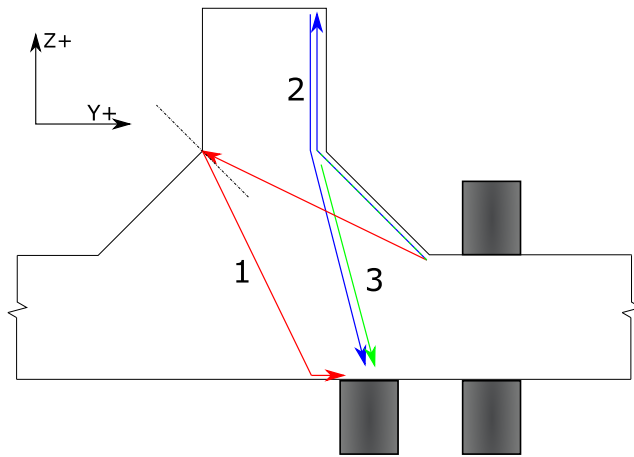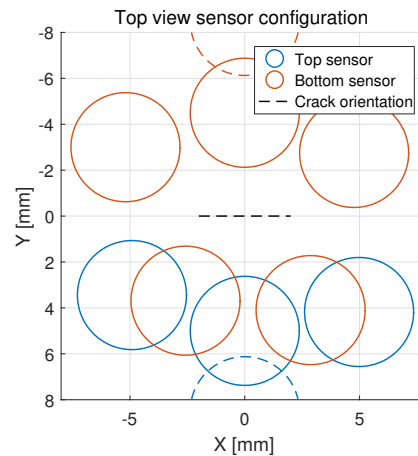
Figure 6.8: Most likely reflection paths

Figure 6.9: Sensor locations on tubular specimen

It could be considered to use additional sensors on the sloped weld surface, Figure 6.7 indicate there is a wave traveling over that surface which is comparable to the wave traveling the outer surface. This choice is averted, since the determination of relative sensor distances is even more complicated when this kind of setup is used.

LOCATION SPECIFIC SPEED
The concept of location specific speed, introduced in Chapter 5, is also investigated for the TS.

Low threshold   Firstly, in order to demonstrate the potential accuracy of localization, an unrealistically low threshold value of 1×10^{-18} m (a signal to noise ratio of 108 dB) has been used to obtain a set of TOA values of high quality. The LUCY values are used to determine the most likely source location, and the resulting errors have been plotted in Figure 6.11b. The localization method using the threshold value reproduces the source location with a mean error of roughly 0.2 mm.

Realistic threshold   Secondly, more realistic values are used. The signals to determine the location specific peed have been shown in Figure 6.10a, and the picked TOA's have been plotted in Figure 6.10b. The signals have been obtained by a sensor at 5 mm surface distance, at the outer surface of the specimen. Figure 6.11a shows the resulting errors for the investigated TOA values, recorded by sensors at locations shown in Figure 6.9. Observing the threshold TOA's, a clear separation can be seen between the 7.8 mm and 8.6 mm (source depths 6 mm and 7 mm respectively). This indicates the quality of the calculated speed will be lower than is desirable. The fact that this separation in picked values is present in the TS, but not the previously investigated 5 mm plate, can be explained by the fact that the TS body thickness is twice that of the plate. The signals thus need to travel further, decreasing their amplitude by spreading of the energy. If a same threshold value is used, it will pick up different waves between the sensors nearby and further away. The same effect can be observed for the *first peak* characteristic. The related localization errors, shown in Figure 6.11a mostly show values just below 1 mm. The *peak* localization slightly outperforms the *threshold* localization.

The TOA values determined using the HC are developing in a more linear fashion, as is the maximum amplitude criterion (MA). The MA time picker has not been used for the 5 mm plate, since it does not perform well in the first few source depths, as can be seen in Figure 6.10b. At greater depths, it does seem to stabilize, so its use for localization for the TS is investigated. Unlike what was the case at the 5 mm plate, the HC localization generates better results than the threshold and peak localization.

Percentual Threshold   In order to combat the supposed problem of bad threshold picking, another way of threshold picking is used. This method does not use a certain fixed amplitude value, but calculates it based on a certain fraction of the maximum amplitude. This *percentual threshold* method is investigated at fractions of 0.1, 0.2, 0.25, 0.3, 0.4, 0.5, 0.6 and 0.8 of the maximum amplitude value of every individual signal. The determined TOA values have been plotted in Figure 6.12a.
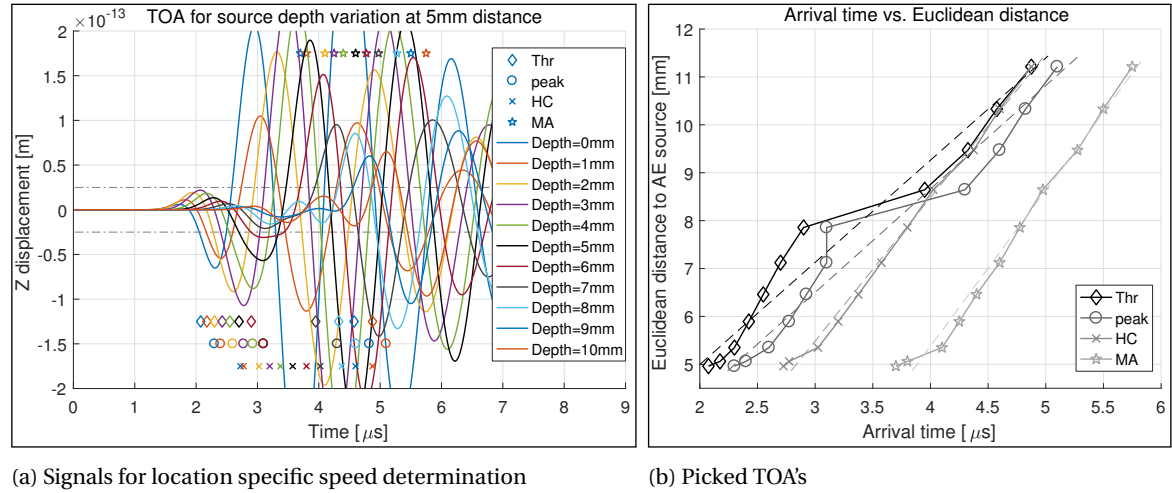
(a) Signals for location specific speed determination

(b) Picked TOA's

Figure 6.10: Signals and TOA's for varying source depths in TS at 5 mm sensor distance

(a) Localization results

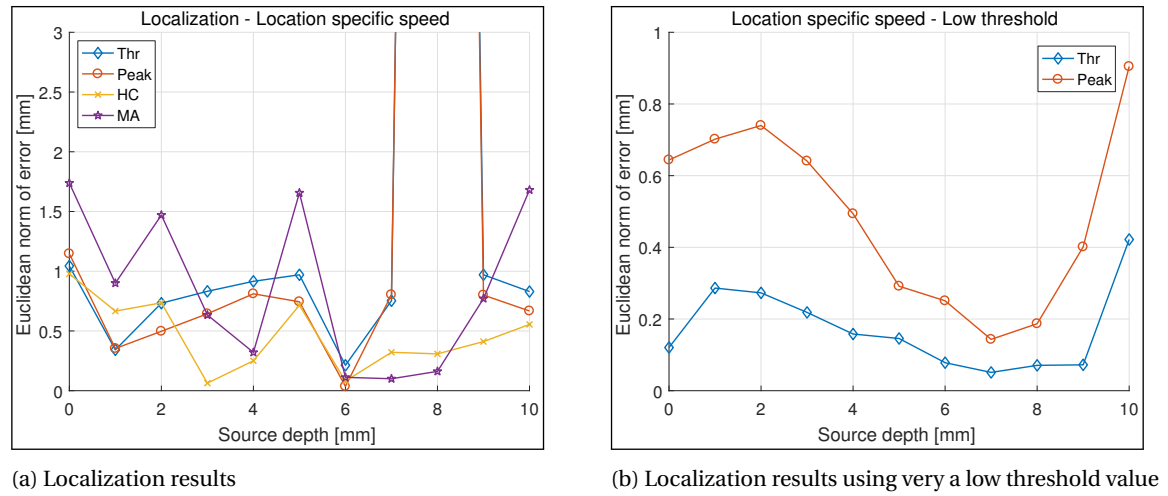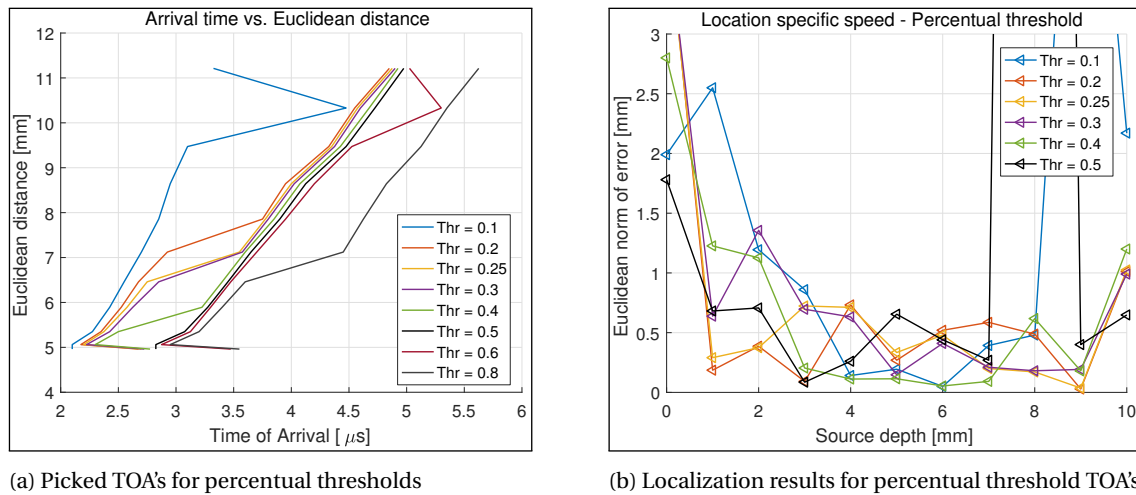(b) Localization results using very a low threshold value

Figure 6.11: Localization results using location specific speed

Looking at the localization errors, is can be concluded that most of the percentual thresholds generate reasonably good results in at source depth of 2 mm to 8 mm. The remaining source depths close to both surfaces are less well localized. This may be due to the fact that the waves originating from these two outermost cases still have too great of a difference in resulting signals at differences in travel distance, which is partly due to the Rayleigh wave which is present in these situations.
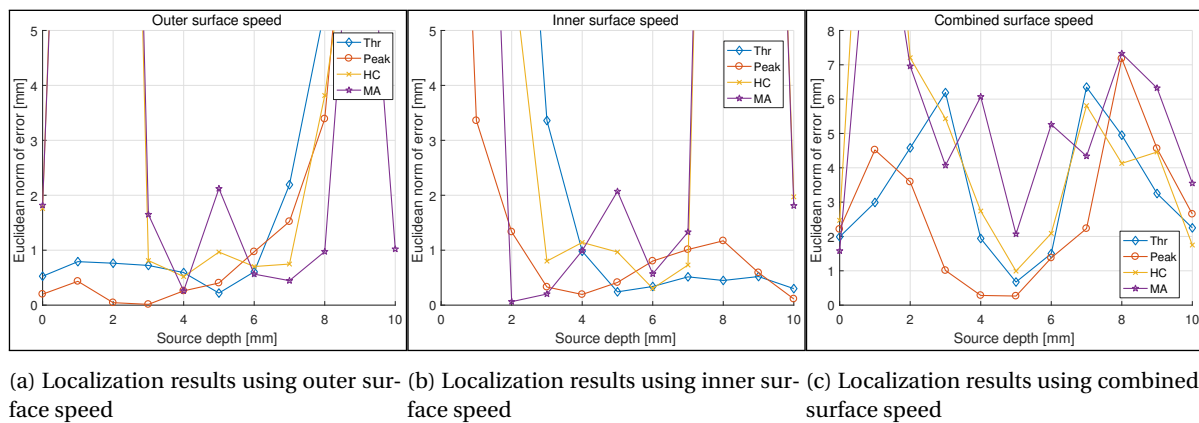
SURFACE SPEED

The use of surface speed, which is determined by two sensors in a straight line from the source, is investigated here. As has been mentioned, the differences between the signals at the outer and inner surface of the TS are quite significant for some source depth simulations. To anticipate for this, three different ways to determine the surface speed are used, namely (1) outer surface speed, (2) inner surface speed, (3) combined surface speed. The first two of which speak for themselves, the speeds used for the localization are determined by two sensors on the outer surface and inner surface respectively. The sensor locations are at $y = 8.5$ mm for the outer surface case, and $y = -8.5$ mm for the inner surface case, as is shown by the dashed lines in Figure 6.9. The fact that the two sensors for each case would in real life have overlap, which is not physically possible, is due to the fact that the output of simulations was set up for a smaller area than to allow for two sensors in row with each other. The third case, the *combined* surface speed, is a combination of the first two cases. The surface speeds are determined on both the outer and inner surface. When the LUCY value is calculated, range values for sensors on the inner and outer surface will be calculated using the corresponding surface speeds.

(a) Picked TOA's for percentual thresholds   (b) Localization results for percentual threshold TOA's

Figure 6.12: Localization results using location specific speed and percentual threshold

(a) Localization results using outer sur-   (b) Localization results using inner sur-   (c) Localization results using combined
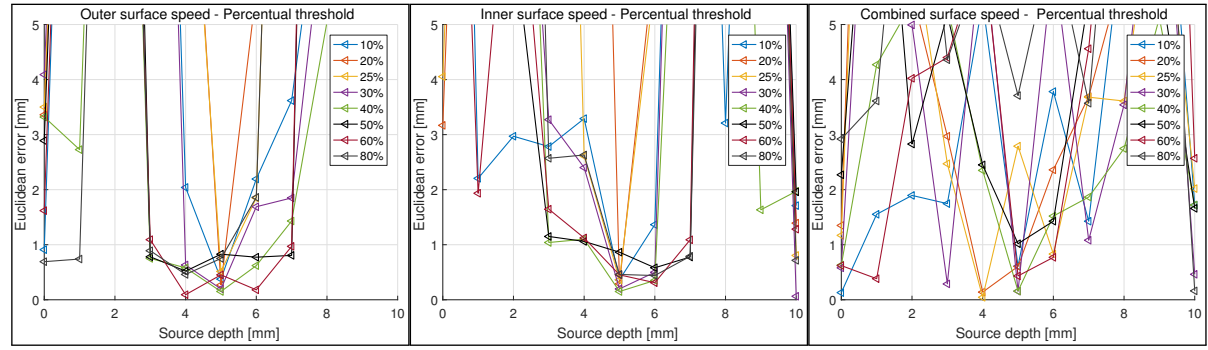face speed   face speed   surface speed

Figure 6.13: Localization results using surface speeds

Figures 6.13a to 6.13c show the localization errors using the surface speeds determined by method 1, 2 and 3 respectively. It should be noted that the threshold that was used here, is the very low value which was also used in Figure 6.11b. Reasonable results could not be obtained using a fixed value, due to the vastly varying wave amplitudes. Instead, percentual thresholds are used, for which the results are shown in Figure 6.14.

Although the low amplitude threshold and peak localization result look promising, that can not be said about any of the other results. Looking at the former mentioned values, it can be seen that the localization is good for AE sources originating near that surface, while decreasing at source depths which travel further away from it. This is to be expected, since the determined speed is closer to the actual value, as has been explained in Section 5.4.2 with the help of Figure 5.18.

The combined surface speeds localization, the results of which are shown in Figure 6.13c, seems to be unsuccessful. Rather than combining the good aspects of the inner and outer surface speeds, it seems that the inaccuracy of speed determination from source further away seems to dominate. Rather than to combine the two speeds, it would be more reasonable to use the outer surface speeds for the initial crack depths, while using the inner surface speeds when the crack depth is determined to have passed the halfway through the material.

When the percentual thresholds are used for localization, this does not result in usable values. When inner and outer surface speeds are used (Figures 6.14a and 6.14b), a comparable effect is seen as during the location specific speed localization. Near the innermost and outermost source locations the accuracy is very bad, while the middle source locations are lower than 1 mm. For the combined surface speed (Figure 6.14), the results are unusable, which is in with the findings in Figure 6.13c.

(a) Localization results using outer surface speed and percentual thresholds

(b) Localization results using inner surface speed and percentual thresholds

(c) Localization results using combined surface speed and percentual thresholds

Figure 6.14: Localization results using surface speeds and percentual thresholds

6.3. CONCLUSIONS

One of the fatigue source models investigated in Chapter 5 has been used in a model of the TS. Due to the size of the model, the mesh size near the source was increased slightly, while the mesh size further away was increased even further. Due to the size of the model, and the computational load this is accompanied with, only the point source model has been used. Simulations with source depths of 0 mm to 10 mm, with steps of 1 mm, have been performed.

The behaviour of the stress waves have been investigated closely. Although the first reflections arrive at 5.2 μs, the amplitude of these reflections are negligible. When the VS600–Z2 sensor simulation is used, the first significant reflections are observed at 13 μs. The initial wave will have passed, so this does not have an effect of the time picking or localization of the AE source.

Localization has been performed for the fatigue source, using location specific and surface speeds. The location specific method was able to locate almost all sources with an error of less than 1 mm. This is less accurate than was the case with the 5 mm plate. The surface speed was less accurate. Only when using a very low threshold value, which can not be used in experimental conditions, the source could be located using the surface speed.

7

CONCLUSIONS AND RECOMMENDATIONS

7.1. CONCLUSIONS

The goal of the thesis, as stated in Section 1.4, was to successfully use the FE method to gain knowledge on waves near a fatigue crack front, and determine the accuracy of localization of this crack front. This chapter will first report on the conclusions of the FE modelling, AE wave behaviour and localization, after which recommendations will given to improve on the results of this thesis.

7.1.1. FINITE ELEMENT MODELLING

In order to achieve the thesis goals, first a reliable way of simulating AE in steel specimens had to be obtained.

PLB AND SIGNAL PROCESSING SIMULATION

The acoustic emission which is generated by a pencil lead break on a 5 mm thick steel plate was the subject of the first series of simulations. Several source functions have been investigated, after which an exponential function with a duration of 2.25 µs has been selected. A sensor model, using the displacement perpendicular to the plate surface, has been used to extract the the generated stress waves, to be used as input for further signal processing. A peaking IIR filter in combination with a highpass Butterworth filter is applied to the signals, in order to simulate the frequency response of the VS600-Z2 sensor. This resulted in very similar signals as the signals which were experimentally obtained, when observed in the 100 kHz–1000 kHz range. This confirmed that the finite element modelling technique and sensor response simulation were accurate.

Using Abaqus/Explicit, a mesh with a maximum element length of 0.125 mm was used in the region where signals were obtained, and a mesh size of 0.5 mm in the zone of low interest. The mesh size was reduced near the PLB source, in order to accommodate multiple elements in the loaded surface. Linear, reduced integration, hexagonal elements were used.

FATIGUE CRACK GROWTH

Using the established simulation method, AE which is formed during fatigue crack growth in a 5 mm steel plate is simulated. These simulations could not be verified by experimental data, since the fatigue experiments did not yield satisfactory signals for this purpose. Three source models which are described in literature were investigated: a *point*, *extended* and *separation* source.

The *point* and *extended* simulations were performed with source depths over the full range of the plate thickness. Due to hardware limitations, the *separation* source simulations could only be performed for a smaller plate dimension, and only until a depth of $a = 2$ mm.

Due to the fact that only a single element is displaced to induce the AE, the FE elements need to be smaller than what was the case with the PLB simulations, in order to prevent hourglassing. Element lengths of 0.1 mm were used.

Fatigue crack growth AE has also been simulated in the TS. Due to hardware limitations only the point source has been used. Since no AE signals in the TS were obtained, these simulated signals could not be verified either.

7.1.2. AE WAVE BEHAVIOUR

The goal of the thesis was to investigate AE behaviour, in relation to time picking and localization.

WAVES TYPES
Lamb, Rayleigh and head waves are were expected to be encountered in close proximity to the AE source.

Lamb waves   The PLB simulations have produced signals up to a travel distance of 70 mm. At 15 mm a separation can be observed between the symmetric and anti-symmetric waves. The former propagating with a higher speed than the latter. As is expected, the sensors pick up less S0 energy than A0 energy.

Rayleigh waves   During simulations of the fatigue sources, Rayleigh surface waves were encountered when the source was located at a free surface. This was the case for the point source at both plate surfaces, and for all simulations of the extended source, since this source model contains a crack surface. The Rayleigh wave travelled with a speed approximately equal to the transverse wave.

Head waves   Another surface wave that was encountered was the head wave. This wave was not only present in the simulations at which the source was located at a free surface, which was the case with the Rayleigh waves. This wave propagated along the surface with the speed of a longitudinal wave, casting a wave into the body with the speed of a transverse wave.

CRACK DEPTH
Analysis of the results of the extended source showed that the when a crack is present in the material, this has an effect on the time picking. The presence of the crack allows for a Rayleigh wave to travel over its surface. This results in a different arrival time for this Rayleigh wave, then for the straight traveling transverse wave, which travels at approximately the same speed. This difference in TOA will change with increasing crack depth. Section 7.1.3 describes how this effect is taken into account during localization of the crack tip.

REFLECTIONS
For the geometry of the TS, the arrival time of wave reflections at a potential sensor locations were investigated. The first reflections were found to arrive at 5.2 μs, the amplitude of these first reflections were however negligible. The first observable reflections arrived at 13 μs, which is at a point in time where they do not influence time picking of the initial wave. Behaviour of the waves inside the body of the specimen has been investigated using Von Mises equivalent stress. The waves observed in the Von Mises plots were linked to the signals obtained with a virtual sensor, and were found to match.

PROPAGATION ANGLE
It was found that the angular location of the sensor, with respect to the source orientation, was of significance for the time picking characteristics of the signals. Consider $\alpha = 0°$ at a straight line perpendicular to the crack, and $\alpha = 90°$ in a straight line extending the crack. With an increasing angle α, the amplitude decreased significantly, with an amplitude decrease of 30 % at 45 degrees. Travel speed on the other hand, seemed to increase with an increase angle α. At propagation angles up to $\alpha = 45°$, the arrival time of the signal were approximately equal. Increasing α further however, resulted in a lower arrival time, with differences up to 0.28 μs at $\alpha = 90°$ for the separation source.

The decrease in amplitude is a potential problem for localization of the crack tip, since the signal to noise ratio will decrease. The change in speed is also deterring the localization accuracy, since currently a single speed is used for all sensors.

DISTANCE
The distance of the sensors have two effects on the signal. The first, and most intuitive, is the fact that the signal decreases in amplitude. This attenuation is due to the spreading of the wave through the body. The second effect is that the travel speeds of time picking characteristics vary slightly over distance. This is due to the fact that these characteristics are not only dependent on a single speed, but the speed of longitudional and transverse, as well as geometry and frequency components. This variation is speed leads to a lower localization accuracy, since the localization algorithm is based on constant travel speeds.

7.1.3. TIME PICKING AND LOCALIZATION
The final goal of the 4D-Fatigue JIP with respect to AE monitoring, is to accurately determine the crack depth. Here the localization accuracy of the simulated AE sources will be reviewed.

DEPTH AND LOCATION SPECIFIC SPEED

It has been concluded that AE sources inside the specimen body at non-zero crack depth, produce waves that travel through the body and waves that travel over the surface. For the calculation of the LUCY value, a single wave travel speed per signal is necessary to determine the range difference with other sensors. Two problems are encountered here:

1. The Rayleigh wave that travels over the surface of the crack travels a non-linear path, making the localization more complicated.

2. The longitudinal and transverse waves that travel through the body do not lie in line with the sensors. When a surface travel speed is determined using two sensors, this speed will deviate from the actual wave speeds.

To circumvent these problems, a new way of wave speed determination is proposed. Location specific speed, which is obtained by simulation, is not an actual speed through the material, but an approximated speed determined by multiple simulations. This method makes use of simulations of several source depths, plotting the TOA of a certain signal characteristic versus the traveled distance up to that point. A fixed sensor location is used. The location specific speed is determined by the slope of a linear fitted line through these points. This method does rely on a linear development of the TOA vs. the euclidean distance, while this is not always the case.

LOCALIZATION ACCURACY

Pencil lead breaks   PLB localization was performed using three sensors at ranges of ~5 mm and ~9 mm. In these ranges errors of approximately 0.1 mm and 0.2 mm were encountered. These inaccuracies can be fully attributed to slight variations in travel speed of the used signal characteristics, since sensor locations are exactly known, and the sensors lie in plane with the source.

Fatigue crack growth AE   Two methods have been used to determine the wave travel speed for localization of the fatigue crack growth AE sources: conventional *surface* speed, and *location specific* speed determination.

In the 5 mm plate, localization was performed for point sources of several time lengths, and for the an extended source model. Using the surface speed, a localization of approximately 0.6 mm was accomplished. The location specific speed was able to achieve an accuracy of 0.4 mm.

For the TS, only the point source was used for localization. Using the surface speed, no reliable source location could be found when realistic threshold values were assumed. The location specific speed was more successful, being able to achieve localization with an error of less than 1 mm for most source depths.

Conditions   It should be noted that the location accuracy values are obtained by sensor locations which are exactly known, so for experimental cases some additional error should be taken account. The localization is also very dependent on the encountered noise in the signal. This noise has not been included in this thesis, although it is taken into account when selecting a threshold value.

7.2. RECOMMENDATIONS

SENSOR RESPONSE FILTER VERIFICATION

Although the PLB simulations have been carried out successfully, some caution must be exercised. Fine tuning of the sensor response filter has been carried out during the PLB simulation process, introducing the risk the used sensor response filter only works in combination with the used PLB source function. This risk is partly negated by the fact that the sensor response filter is mainly based on the frequency response of the sensors, and by the fact that the simulated signals were verified over a wide range of travel distances. It would however be preferable to verify the sensor response filter with a different plate thickness, and preferably with a different material, if this sensor response filter was to be used in future research.

FATIGUE SIGNAL VERIFICATION

Since the fatigue tests did not produce useful signals, the signals generated by the simulation have not been able to be verified. The conclusions on the localization of different source functions in the 5 mm plate did agree, which does solidify the found localization accuracy. Verification of the simulated signals would however greatly increase the effectiveness of the proposed location specific speed during localization.

LOCATION SPECIFIC SPEED

Location specific speed was found to be more effective than the surface speed, it could however still be improved on. In this thesis, the location specific speed was determined using a single sensor location, while multiple sensor locations were used for the crack front localization. The localization results could be improved on if multiple sensor locations were investigated, in order to provide a location specific speed for each used sensor in localization. Also, as has been stated, in order to use this speed determination methods in actual experimental cases, the signals obtained by the simulation should be verified by actual experimental signals.

NOISE

The investigation in this thesis was mainly done with the assumption that noise amplitude during fatigue testing is at a level at which the fatigue AE waves are clearly distinguishable. During the fatigue tests carried out in the Materials Laboratory at 3mE, this was definitely not the case. Noise poses a serious threat to successful AE monitoring. Due to the nature of the Hexapod, in which the TS will be fatigue tested, the expectations are that noise will be of much lower amplitude than was the case during the fatigue test described in Chapter 5. This should however be verified in order to be able to use the conclusions in this thesis.

LOCALIZATION ACCURACY

The level of accuracy which was found for the fatigue AE source in the TS, used a sensor locations which were known very precisely. In reality however, there will always be some uncertainty in sensor location, because the measurements of their relative distance is prone to human error. When sensors are used on both sides of a plate, these measurements are even harder to perform accurately. The effect of these sensor location inaccuracies should be investigated, in order to form a more complete conclusion on localization accuracy.

OFF-CENTRE CRACK LOCATIONS

With the limited physical memory that was available to perform FE simulations, the use of two symmetry boundary planes was necessary to be able to simulate a large enough model. The model size was necessary to prevent reflections of the boundaries to arrive at the sensor before the simulation end time. The fact that a symmetry plane was used halfway through the crack length, prevented the use simulation of off-centre AE sources. In reality, during a single fatigue crack step, nucleation occurs at multiple locations on the crack tip. The localization accuracy of these source locations has not been investigated. To gain information on the localization accuracy of these sources, simulations with only a single symmetry boundary plane, along the length of the crack, should be carried out.

PROPAGATION ANGLE VS. SPEED

It was concluded that fatigue crack growth AE waves do not propagate in an axi-symmetric fashion. More specifically, travel speeds seem to increase with an increasing propagation angle. This effect should be taken into account in order to increase the localization accuracy. The effect of speed on propagation angle should be investigated further.

SENSOR LOCATIONS

The current work has investigated localization accuracy for a single sensor setup per specimen type. In order to form a more complete conclusion on localization accuracy, more sensor configurations should be investigated.
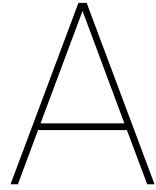
REFERENCES

[1] Abaqus 6.13-1 documentation. Dassault Systèmes, 2013.

[2] MATLAB Student, version 9.1.0 (R2016b). The MathWorks Inc., 2016. Natick, Massachusetts, United States.

[3] AKBARI, M., AND AHMADI, M. The application of acoustic emission technique to plastic deformation in low carbon steel. *Physics Procedia 3* (2010), 795–801.

[4] CHULUUNBAT, T., LU, C., KOSTRYZHEV, A., AND TIEU, K. Investigation of x70 line pipe steel fracture during single edge-notched tensile testing using acoustic emission monitoring. *Materials and Science Engineering 640* (2015), 471–479.

[5] CUADRA, J., BAXEVANAKIS, K. P., MAZZOTTI, M., BARTOLI, I., AND KONTOS, A. Energy dissipation via acoustic emission in ductile crack initiation. *International Journal of Fracture 199* (2016), 89–104.

[6] CUADRA, J., VANNIAMPARAMBIL, P. A., SERVANSKY, D., BARTOLI, I., AND KONTSOS, A. Acoustic emission source modeling using a data-driven approach. *Journal of Sound and Vibration 341* (2015), 222–236.

[7] FELIPPA, C. A. Advanced finite element methods (ASEN 6367). Dep. of Aerospace Engineering Sciences University of Colorado at Boulder, 2017. Lecture Notes, Chapter 9.

[8] GARY, J., AND HAMSTAD, M. A. On the far-field structure of waves generated by a pencil lead break on a thin plate. *Journal of Acoustic Emission 12*, 3/4 (1994), 157–170.

[9] HAMSTAD, M. A., O'GALLAGHER, A., AND GARY, J. Modeling of buride monopole and dipole sources of acoustic emission with a finite element technique. *Journal of Acoustic Emission 17* (1999), 97–110.

[10] HILL, R., FORSYTH, S. A., AND MACEY, P. Finite element modelling of ultrasound, with reference to transducers and AE waves. *Ultrasonics 42* (2004), 253–258.

[11] NAZARCHUK, Z., SKALSKYI, V., AND SERHIYENKO, O. *Acoustic Emission: Methodology and Application.* Springer, 2017.

[12] ONO, K., CHO, H., AND MATSUO, T. Transfer functions of acoustic emission sensors. *Journal of Acoustic Emission 26* (2008), 72–90.

[13] PROSSER, W. H., HAMSTAD, M. A., GARY, J., AND O'GALLAGHER, A. Reflections of AE waves in finite plates: Finite element modeling and experimental measurements. *Journal of Acoustic Emission 17(1-2)* (1999), 37–47.

[14] ROGERS, L. M. *Structural and Engineering Monitoring by Acoustic Emission Methods - Fundamentals and Applications.* Lloyd's Register, 2001.

[15] SAUSE, M. G. R., HAMSTAD, M. A., AND HORN, S. Finite element modeling of conical acoustic emission sensors and corresponding experiments. *Sensors and Actuators A: Physical 184* (2012), 64–71.

[16] SAUSE, M. G. R., HAMSTAD, M. A., AND HORN, S. Finite element modeling of Lamb wave propagation in anisotropic hybrid materials. *Composites: Part B 53* (2013), 249–257.

[17] SAUSE, M. G. R., AND HORN, S. Simulation of acoustic emission in planar carbon fiber reinforced plastic specimens. *Journal of Nondestructive Evaluation 29* (2010), 123–142.

[18] SAUSE, M. G. R., AND HORN, S. Simulation of lamb wave excitation for different elastic properties and acoustic emission source geometries. *Journal of Acoustic Emission 28* (2010), 142–154.

[19] SAUSE, M. G. R., AND RICHLER, S. Finite element modeling of cracks as acoustic emission sources. *Journal of Nondestructive Evaluation 34*, 4 (2015).

[20] SCHEEREN, B. On the validation and preparation of acoustic emission methods for fatigue analysis, 2016. Internship report. Vallen Systeme GmbH.

[21] SU, Z., AND YE, L. *Lecture notes in applied and computational mechanics: Identification of damage using Lamb waves.* Springer, 2009.

[22] VALLEN, H. Acoustic emission testing: Fundamentals, equipment, applications, 2006.

[23] VALLEN SYSTEME GMBH. *AMSY-6 System Description*, 2015.

[24] VALLEN SYSTEME GMBH. *AE-Preamplifier Data Sheet: AEP5 / AEP5H*, 2017.

[25] VALLEN SYSTEME GMBH. *AE-Sensor Data Sheet: VS600-Z2*, 2017.

[26] VANNIAMPARAMBIL, P. A., GUCLU, U., AND KONTSOS, A. Identification of crack initiation in aluminum alloys using acoustic emission. *Experimental Mechanics 55* (2015), 837–850.

APPENDICES

A

PLB Source Comparison

This appendix describes the process of selecting the most accurate source function, to portray a pencil lead break. Simulated signals, using multiple source functions, are compared to experimentally obtained signals. Several travel distances are investigated.
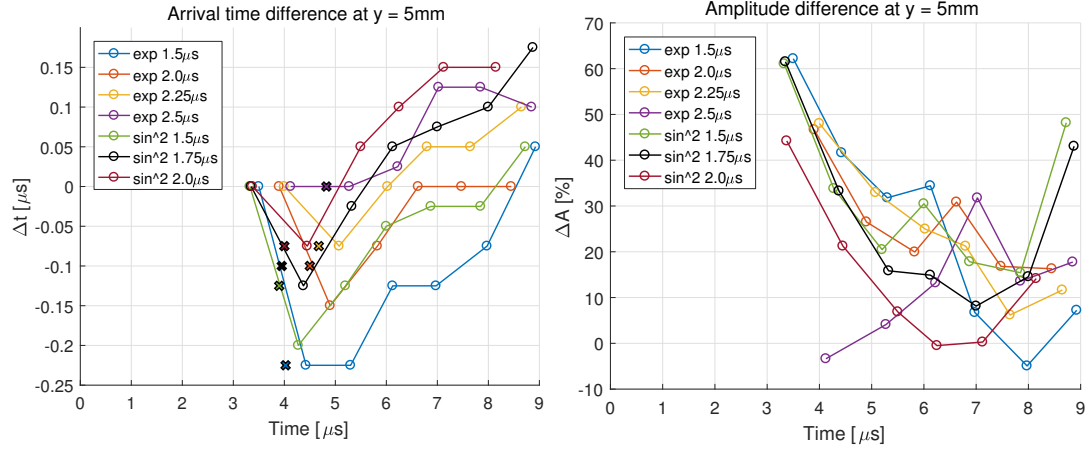
A.1. Signals at 5 mm

When comparing the global form of the simulated signals with the recorded signals, it can be concluded that all simulated signals are very similar to the recorded signals up until 9 μs. Figure 4.2a already showed that the behavior of the recorded signals became very random after this point in time, so this is to be expected. For this reason, only the part before this point is taken into account in the evaluation of the signals. One of the differences that can be noted between the *exp* sources and *sin*^{2} sources is the steeper slope and the shorter rise time of the latter, which is a closer approximation to the recorded signals. The amplitude of these first waves however, are too high.

The differences in arrival times for signals around 5 mm are shown in Figure 4.9a. The *exp* 2.25 μs source does not deviate from the recorded signal more than 0.1 μs, which is a lower value than that of the rest. The *exp* 2.5 μs source however has better arrival times for the first three peaks, along with a lower difference in time of minimum HC. The *sin*^{2} 1.5 μs source has the greatest deviation.

The differences in peak amplitudes, shown in Figure 4.9b, are best for the *exp* 2.25 μs and *exp* 2.5 μs sources. Note that the rate of change is important here, rather than the actual amplitude, since the signals are scaled to an arbitrary value.

The Choi-Williams transformations are shown in Figure A.3. The global distribution of all sources is pretty similar. It can be noted that the sources with longer rise times contain a higher low-frequency component, compared to the same source functions with a shorter rise time. The *sin*^{2} 1.5 μs source lacks most energy in the lower frequency range, which is also the case for the rest of the signals, but to a lesser degree.

(a) Difference in arrival time at 5 mm

(b) Amplitude difference at 5 mm

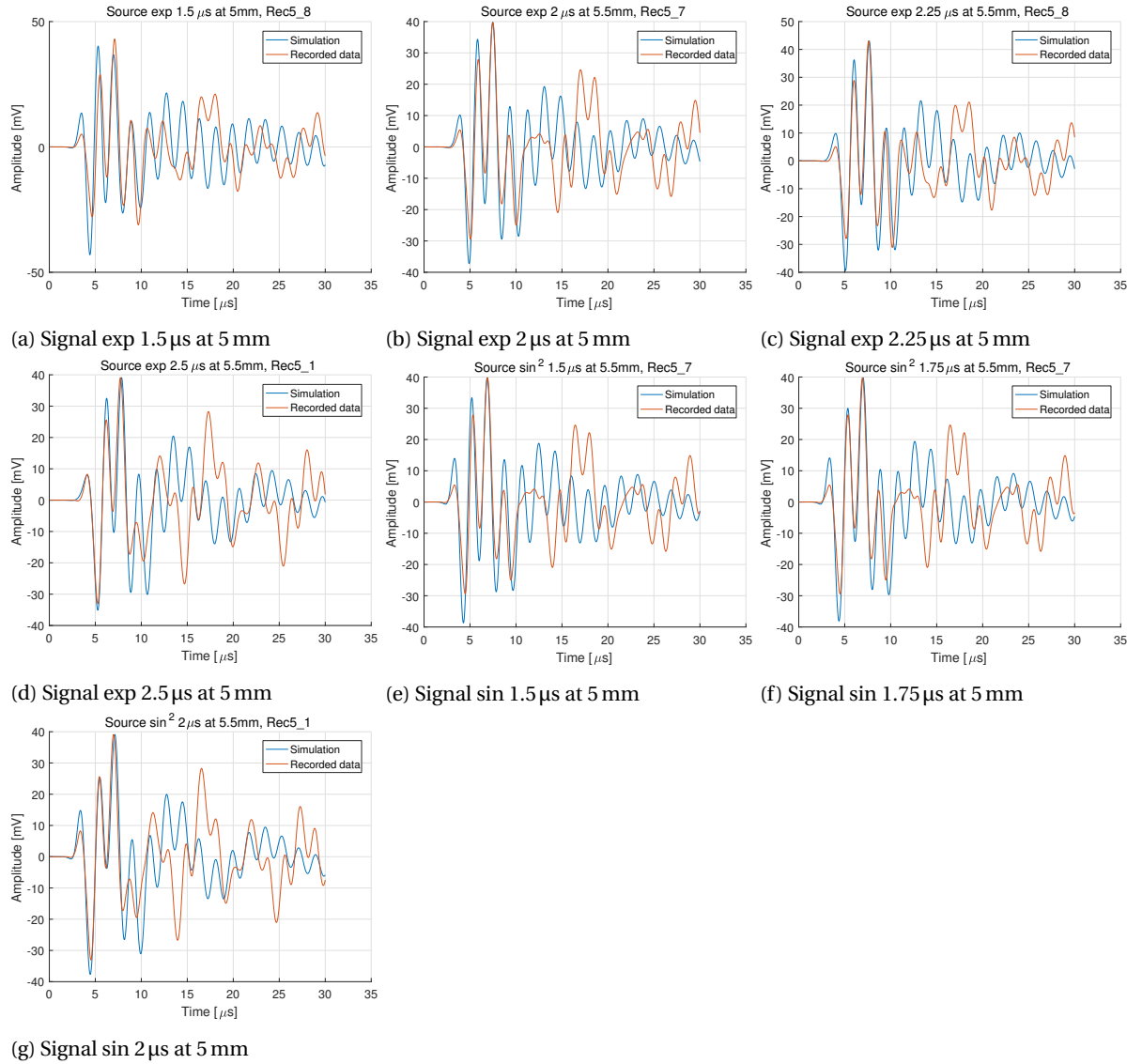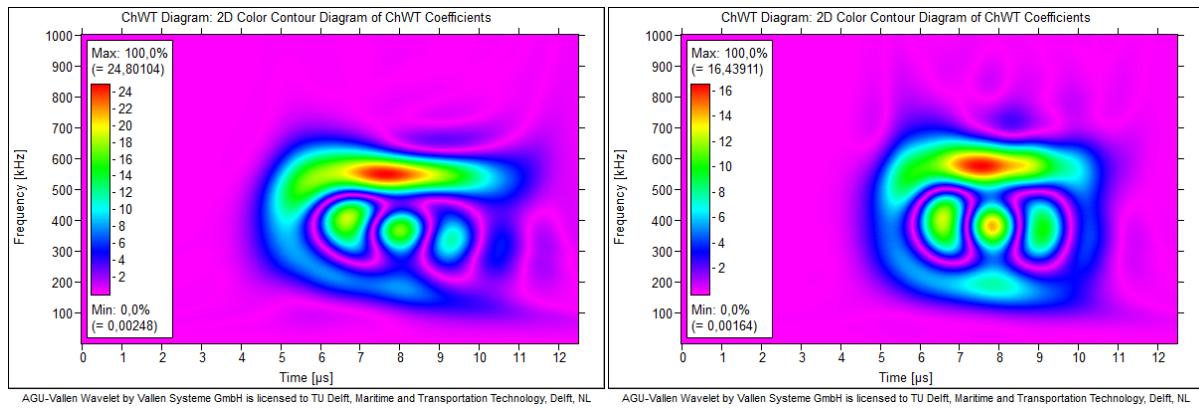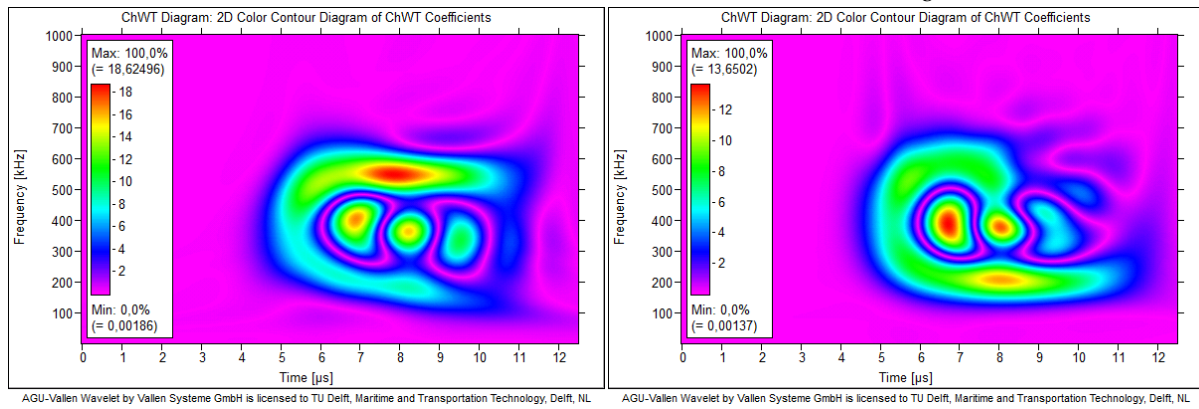Figure A.1: Source comparison at 5 mm

(a) Signal exp 1.5 μs at 5 mm

(b) Signal exp 2 μs at 5 mm

(c) Signal exp 2.25 μs at 5 mm

(d) Signal exp 2.5 μs at 5 mm

(e) Signal sin 1.5 μs at 5 mm

(f) Signal sin 1.75 μs at 5 mm

(g) Signal sin 2 μs at 5 mm

Figure A.2: Source comparison signals at 5 mm

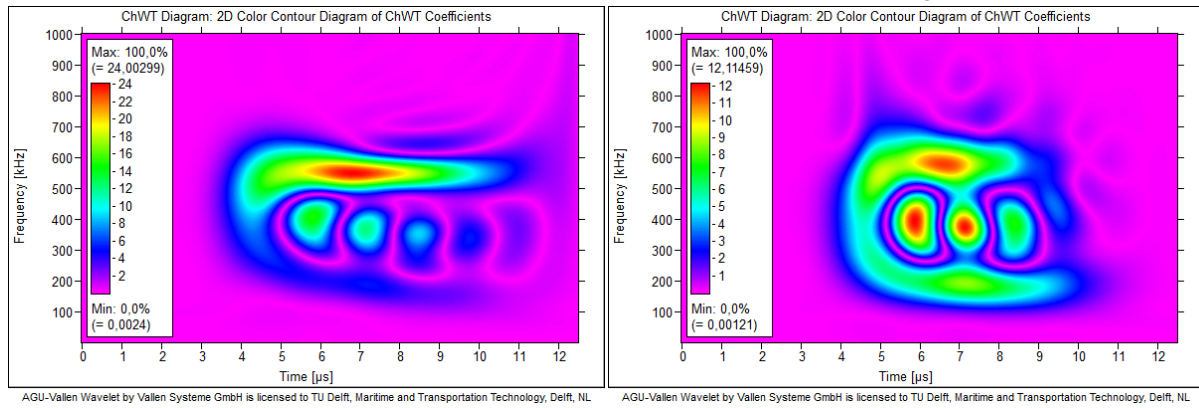(a) CW transform of source # 3
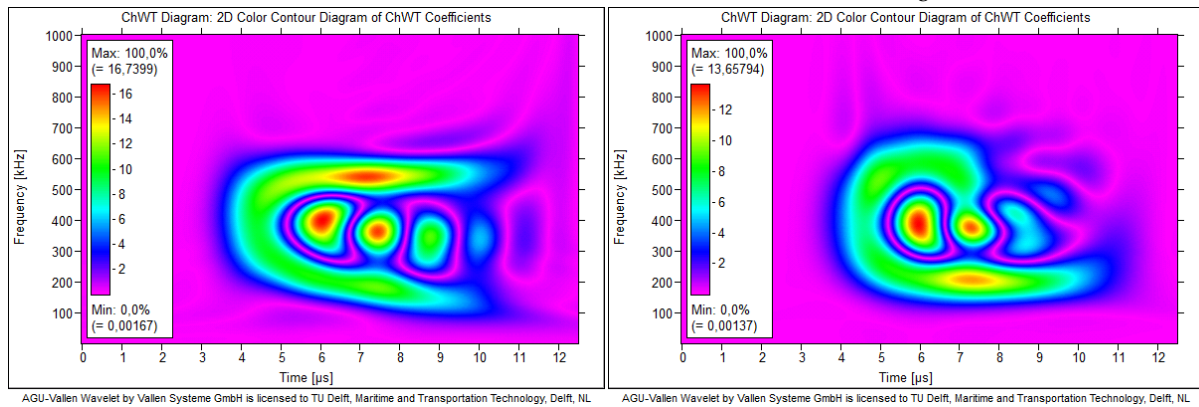
(b) CW transform of recorded signal for source # 3

(c) CW transform of source # 4

(d) CW transform of recorded signal for source # 4

(e) CW transform of source # 5

(f) CW transform of recorded signal for source # 5

(g) CW transform of source # 7

(h) CW transform of recorded signal for source # 7

Figure A.3: Choi-Williams transformations of signals at 5mm

A.2. SIGNALS AT 10 mm

Like was the case with the 5 mm signals, where the recorded signals started to deviate at 9 μs, the signals at 10 mm show the same behaviour at 15 μs. The signals will be evaluated up until that point in time. The global form of all the simulated signals, shown in Figure A.5, is generally good, however it should be noted that both considered *exp* sources do not generate the tiny first wave which can be seen in the recorded signals before 5 μs. The *sin*² 2 μs source however, lacks the second bigger wave.

Looking at the differences in arrival time, the *exp* 2.25 μs source can be seen to be the best in this regard. It is however closely followed by the *exp* 2.5 μs and *sin*² 1.5 μs sources. The *sin*² 2 μs source however, shows great differences in the arrival time of its peaks. The minimum HC is simulated very well by the *exp* sources, with a difference of 0.025 μs, and in a somewhat lesser degree by the *sin*² 1.5 μs source.

In terms of peak amplitude values, the *exp* 2.25 μs and *sin*² 1.5 μs sources perform well. The *exp* 2.5 μs source very much underestimates the second big wave, and the *sin*² 2 μs source does this in an even greater extend.

The 700 kHz and higher frequency components seem to be underestimated by all the simulated signals. This can be explained by the fact that the sensor response simulation filters attenuates this frequency range more than would be ideal, as has been described in Section 3.3.3. Furthermore the *exp* 2.5 μs and *sin*² 2 μs sources overestimate the low frequency ranges, which is contrary to what was the case with the simulated signals at 5 mm.
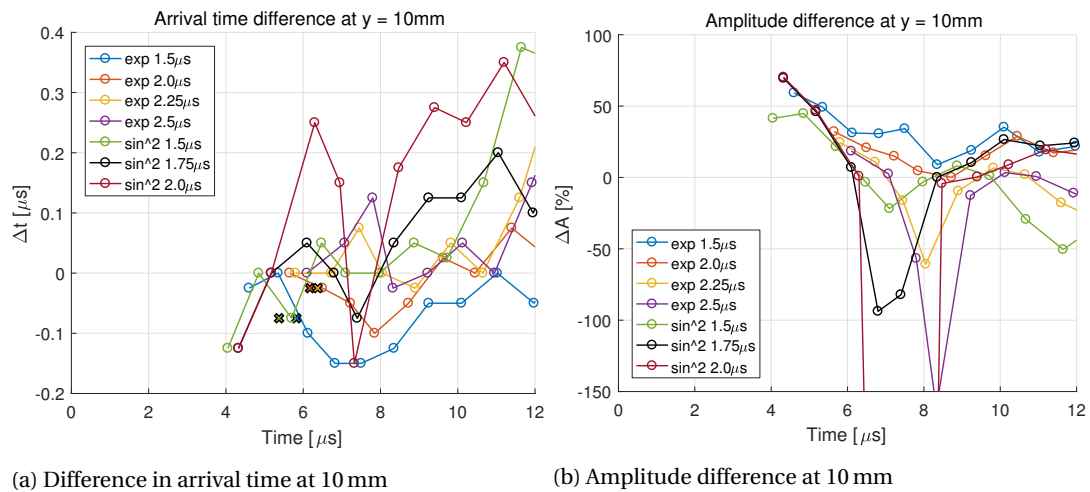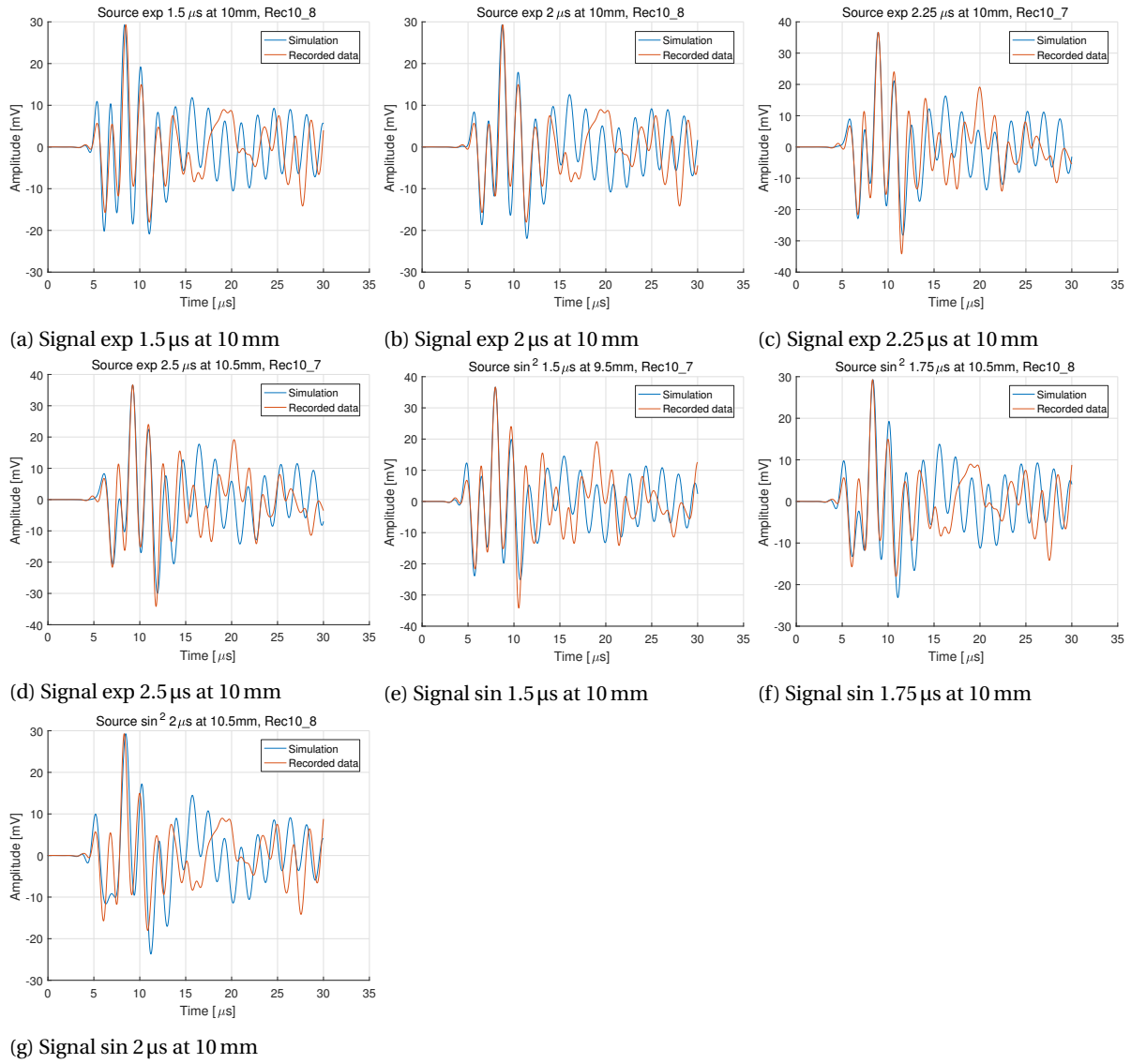

(a) Difference in arrival time at 10 mm

(b) Amplitude difference at 10 mm

Figure A.4: Source comparison at 10 mm

(a) Signal exp 1.5 µs at 10 mm

(b) Signal exp 2 µs at 10 mm

(c) Signal exp 2.25 µs at 10 mm

(d) Signal exp 2.5 µs at 10 mm

(e) Signal sin 1.5 µs at 10 mm

(f) Signal sin 1.75 µs at 10 mm

(g) Signal sin 2 µs at 10 mm

Figure A.5: Source comparison signals at 10 mm

(a) CW transform of source # 3

(b) CW transform of recorded signal for source # 3

(c) CW transform of source # 4

(d) CW transform of recorded signal for source # 4

(e) CW transform of source # 5

(f) CW transform of recorded signal for source # 5

(g) CW transform of source # 7

(h) CW transform of recorded signal for source # 7
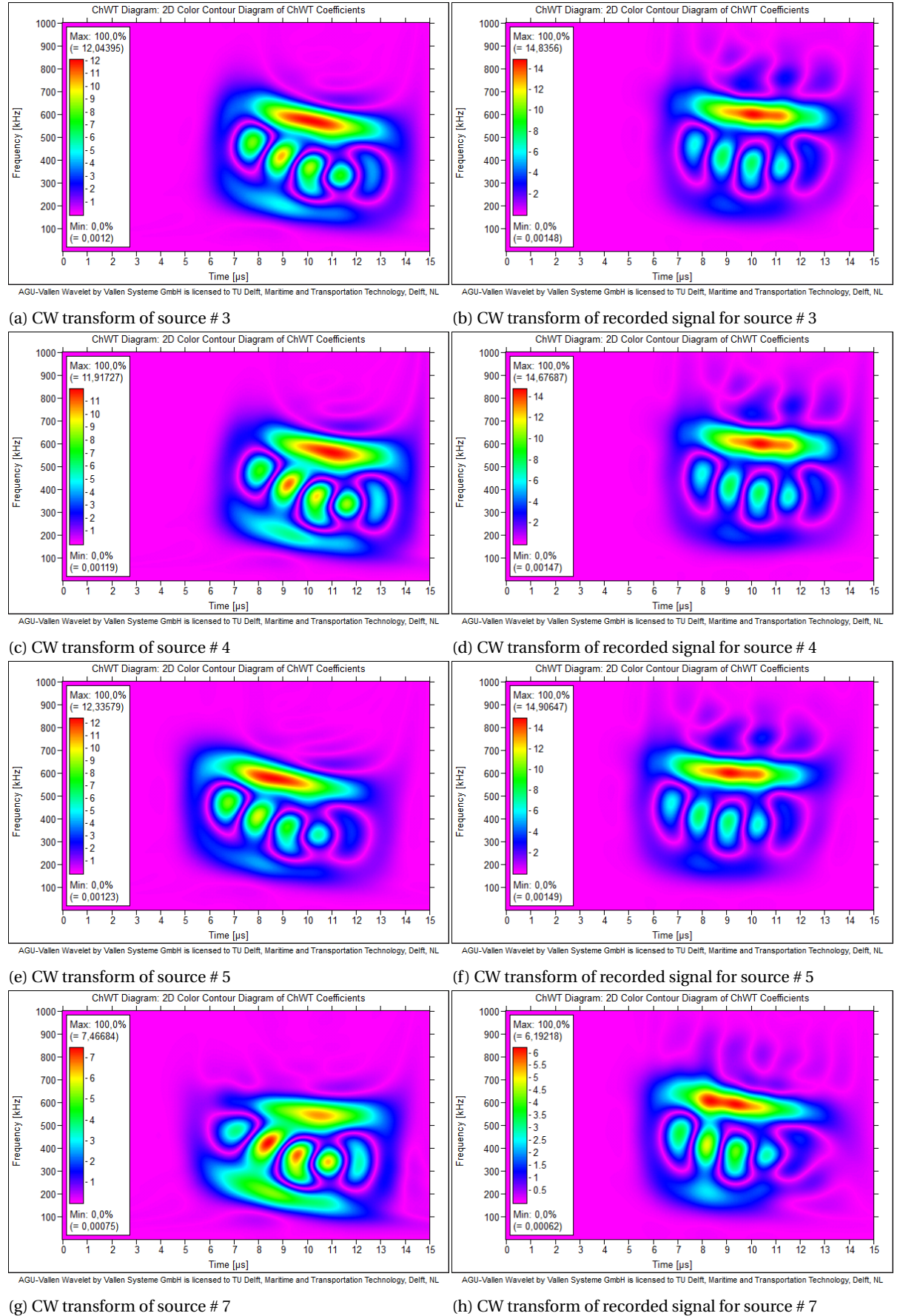
Figure A.6: Choi-Williams transformations of signals at 10mm

A.3. SIGNALS AT 30 mm

The signals will be evaluated until 20 μs, since after this time the first S0 wave mode reflections will arrive. Again, the global wave forms of all simulated signals is very similar with the recorded data, with one particular exception, which is present in all sets. In all recorded signals, a small interruption can be seen in the descent around 14 μs. None of the source functions simulate this small wave correctly, which results in the high values in Figure 4.9e and Figure 4.9f.

The arrival times of the local maxima and minima are very good for all the signals considered in Figure 4.9e, with the differences for the first six occurrences mostly staying within the ±0.1 μs boundaries. After this time, a great peak occurs for all signals, which has been discussed earlier. After this peak, the values return to the low values, again staying within differences of ±0.1 μs .

In terms of amplitude differences, the sin^2 sources seem to be the most consistent, since these exhibit the flattest slope. The frequency components in time have a good correspondence between the simulated and recorded signals. As was the case with the previous travel distances, when increasing the duration of the source function time, the bigger the low frequency component becomes, compared to the higher frequencies.
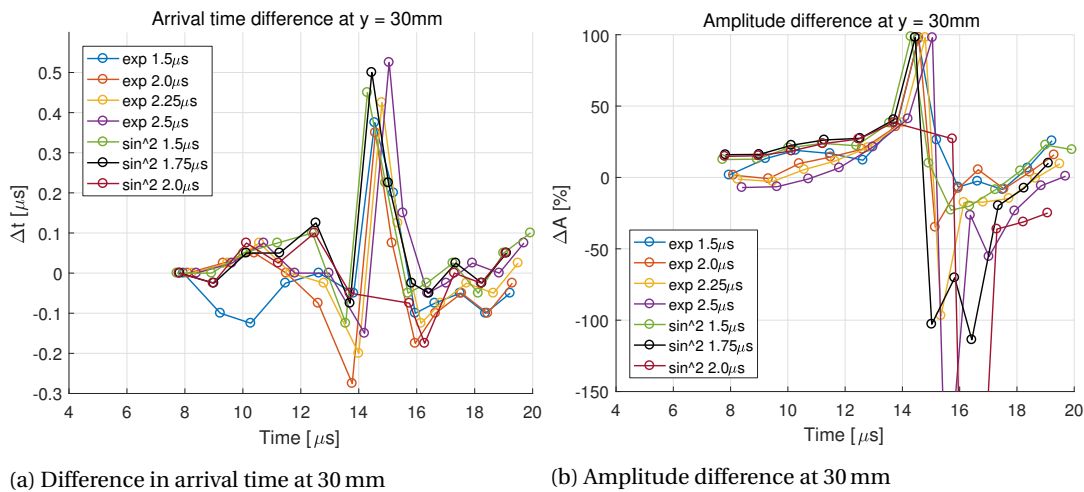

(a) Difference in arrival time at 30 mm

(b) Amplitude difference at 30 mm

Figure A.7: Source comparison at 30 mm

(a) Signal exp 1.5 µs at 30 mm

(b) Signal exp 2 µs at 30 mm

(c) Signal exp 2.25 µs at 30 mm

(d) Signal exp 2.5 µs at 30 mm

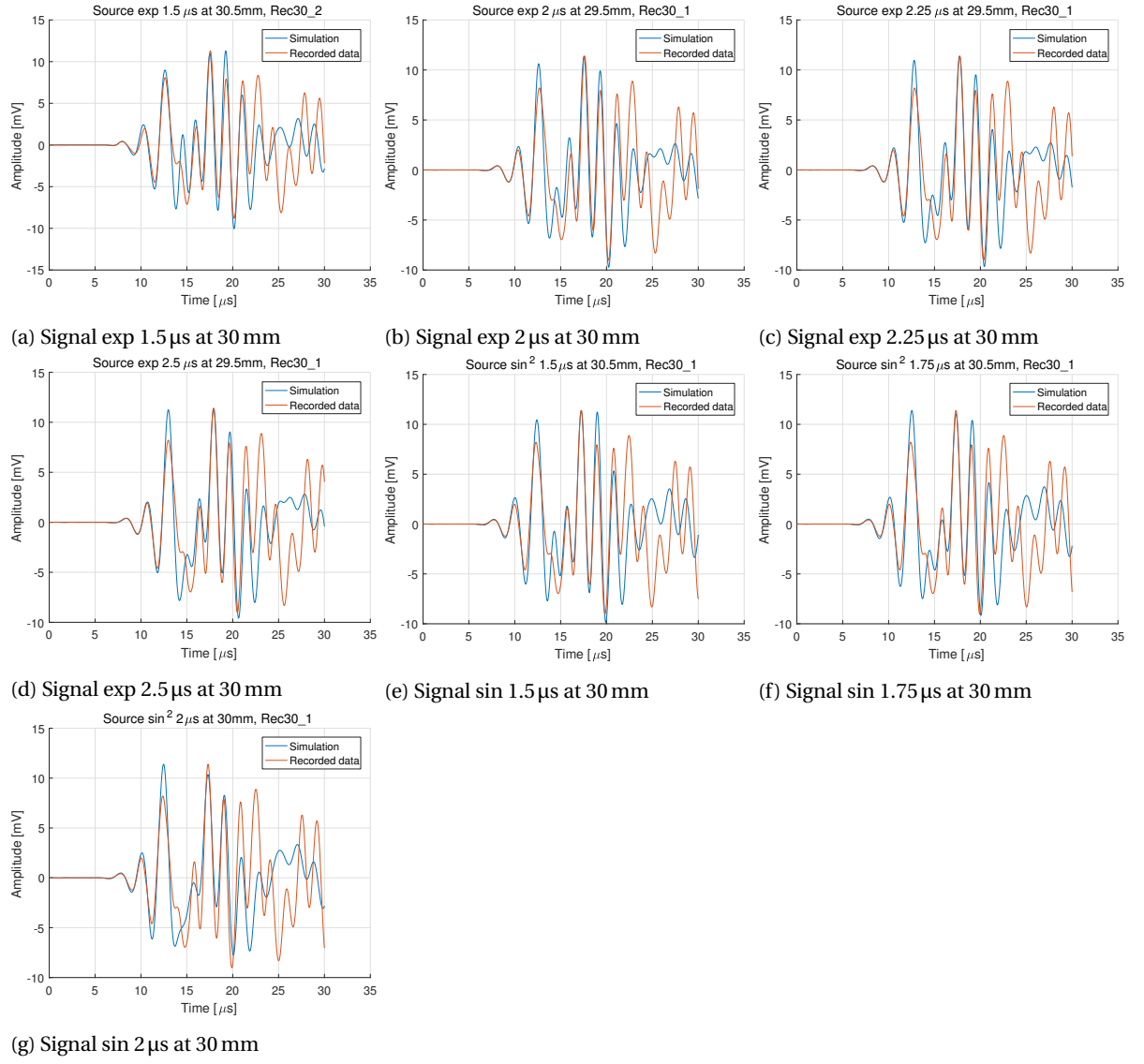(e) Signal sin 1.5 µs at 30 mm

(f) Signal sin 1.75 µs at 30 mm
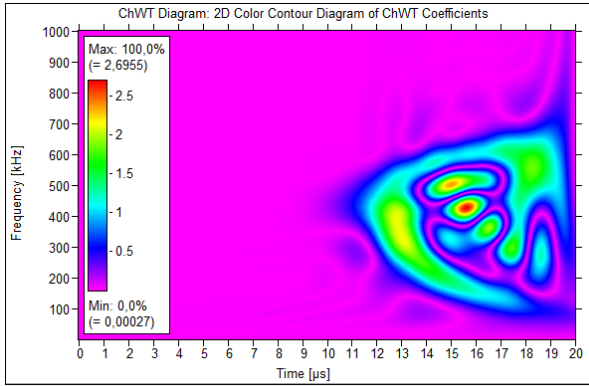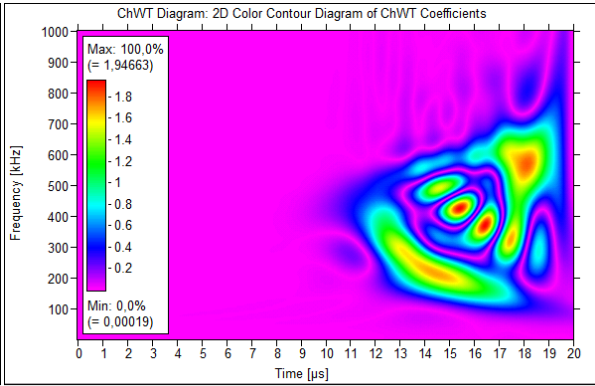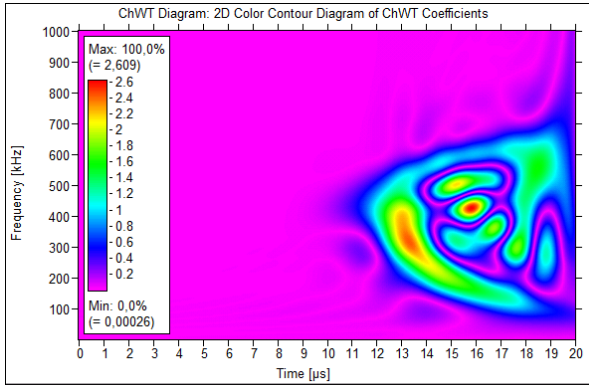
(g) Signal sin 2 µs at 30 mm
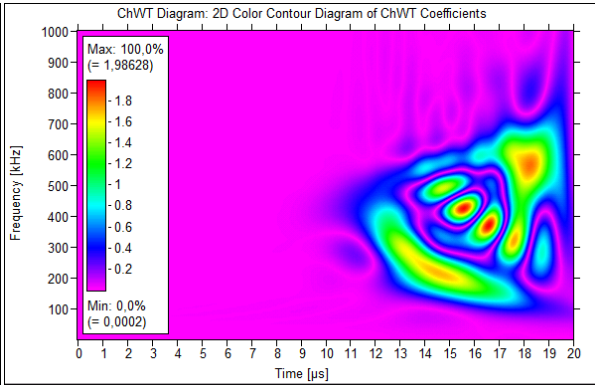
Figure A.8: Source comparison signals at 30 mm
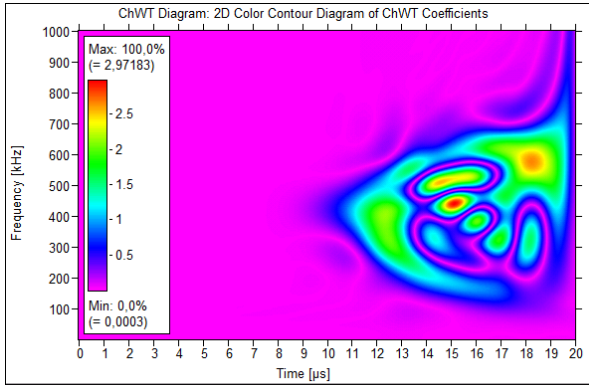
(a) CW transform of source # 3

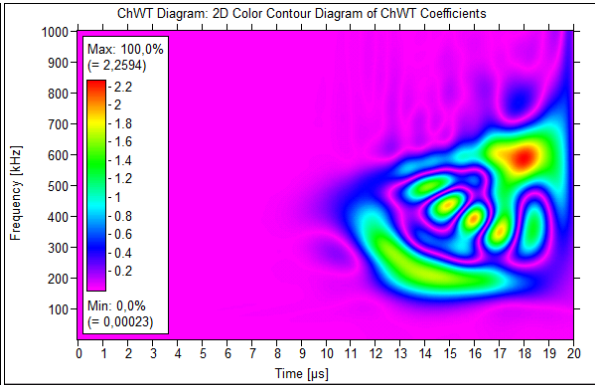(b) CW transform of recorded signal for source # 3
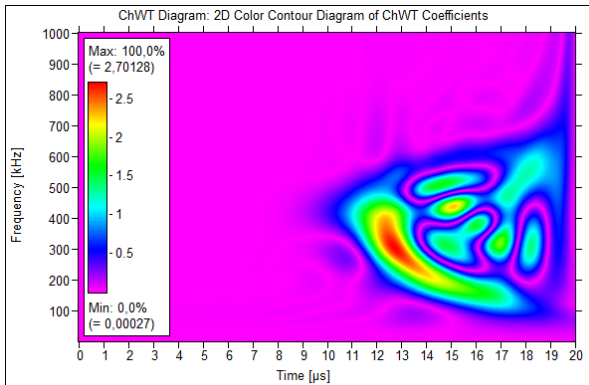

(c) CW transform of source # 4

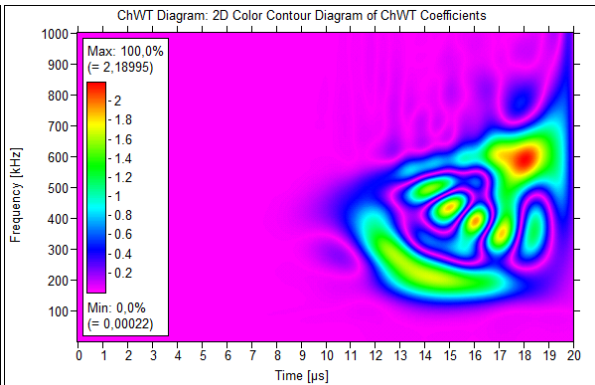(d) CW transform of recorded signal for source # 4

(e) CW transform of source # 5

(f) CW transform of recorded signal for source # 5

(g) CW transform of source # 7

(h) CW transform of recorded signal for source # 7

Figure A.9: Choi-Williams transformations of signals at 30mm

A.4. SIGNALS AT 70 mm

AE source localization will be done with sensors close. For this reason, perfect simulation of signals at 70 mm is not of high priority. It is however useful to compare these simulated signals with the recorded data, in order to verify the source model. It also verifies that the sensor response simulation filters are correct, and do not only work for the combination of a certain source function and this filter chain. In order to obtain signals without reflections at this distance, the model has been enlarged to a length L=110 mm.

The global form of the *exp* sources signals are in good accordance with the recorded signals. The *sin²* sources simulate the signals in a less satisfactory manner. This might however be because of the fact that there are only three recordings of PLB's at this distance, two of which result from a less well controlled experimental setup than that of which the previous signals do.

Differences in arrival times are significantly bigger than which was the case at shorter distances. This is to be expected, since the travel distance is bigger too. Minor differences in speed will result in a increasingly larger TOA difference with increasing travel distances. The mean difference of the waves stays around zero, which is desirable. The mean amplitudes differences, while peaks are present, also stay around the same level.

In the Choi-Williams plots, it can again be concluded that the 700 kHz frequencies and up, are underestimated by the simulations. Furthermore, the simulations underestimate the 600 kHz components.
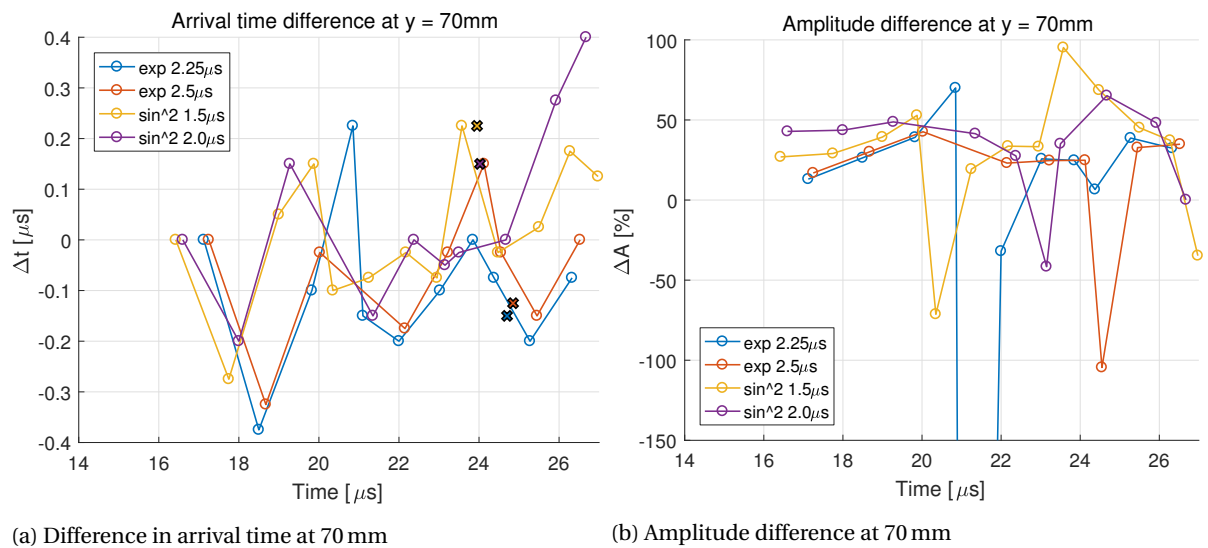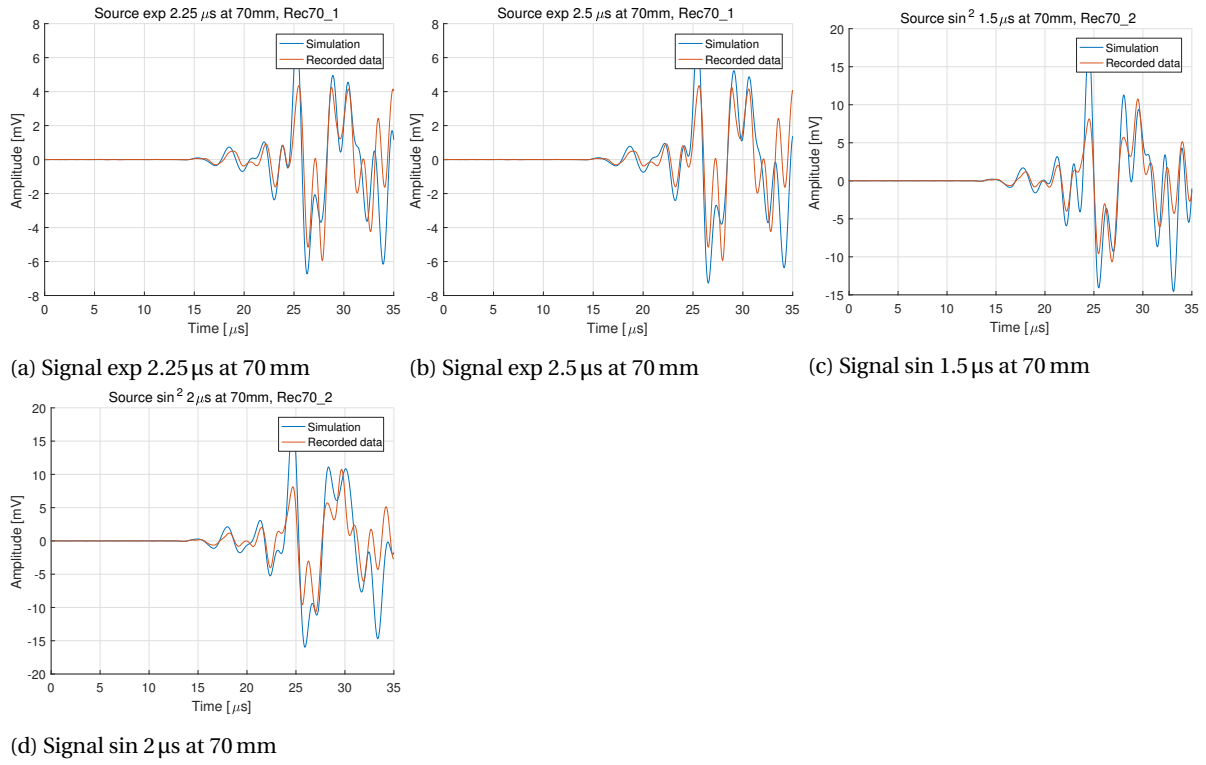

(a) Difference in arrival time at 70 mm

(b) Amplitude difference at 70 mm

Figure A.10: Source comparison at 70 mm

(a) Signal exp 2.25 μs at 70 mm

(b) Signal exp 2.5 μs at 70 mm

(c) Signal sin 1.5 μs at 70 mm

(d) Signal sin 2 μs at 70 mm

Figure A.11: Source comparison signals at 70 mm

(a) CW transform of source # 3

(b) CW transform of recorded signal for source # 3

(c) CW transform of source # 4

(d) CW transform of recorded signal for source # 4

(e) CW transform of source # 5

(f) CW transform of recorded signal for source # 5

(g) CW transform of source # 7
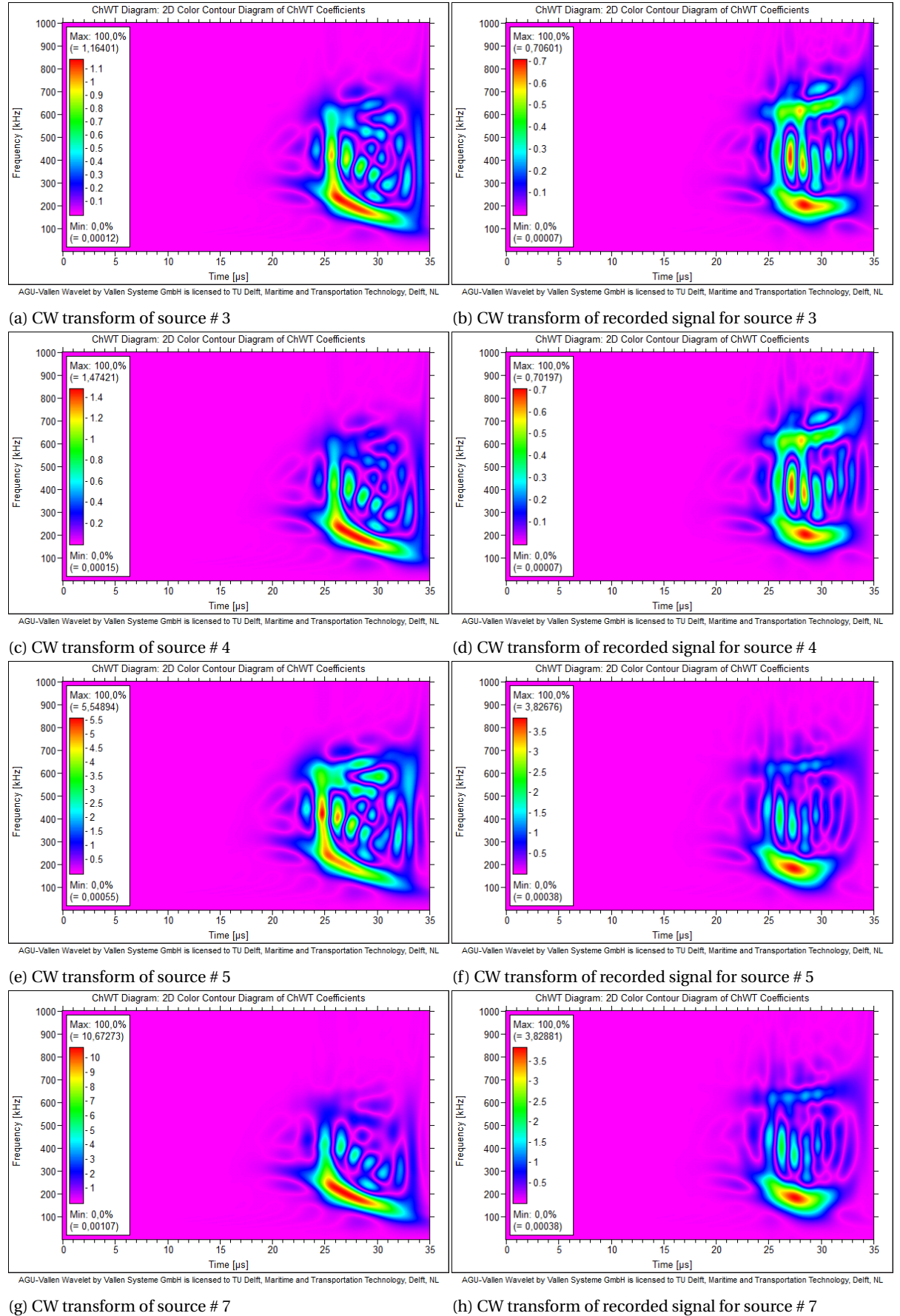
(h) CW transform of recorded signal for source # 7
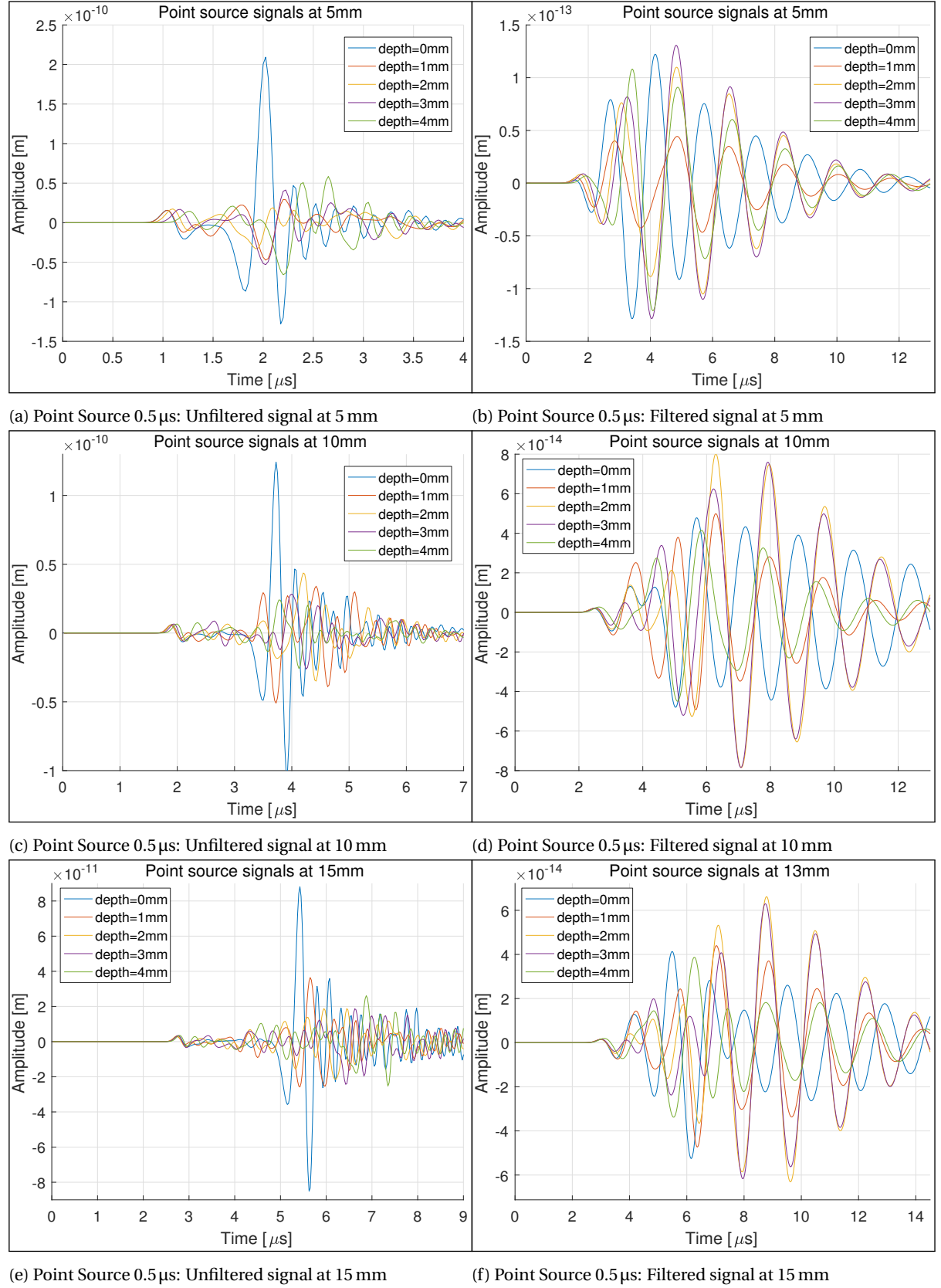
Figure A.12: CW transformations of signals at 70mm

B

FATIGUE SOURCE SIMULATION DATA

B.1. SIMULATED SIGNALS AND THEIR FREQUENCY COMPONENTS

This appendix serves to provide additional information on the obtained signals during the fatigue crack growth AE simulations, which are described in Chapter 5.

(a) Point Source 0.5 µs: Unfiltered signal at 5 mm

(b) Point Source 0.5 µs: Filtered signal at 5 mm

(c) Point Source 0.5 µs: Unfiltered signal at 10 mm

(d) Point Source 0.5 µs: Filtered signal at 10 mm

(e) Point Source 0.5 µs: Unfiltered signal at 15 mm

(f) Point Source 0.5 µs: Filtered signal at 15 mm

Figure B.1: Point Source 0.5 µs signals at several distances from source

(a) Choi-Williams transform for source depth of 0 mm

(b) Choi-Williams transform for source depth of 1 mm

(c) Choi-Williams transform for source depth of 2 mm

(d) Choi-Williams transform for source depth of 3 mm

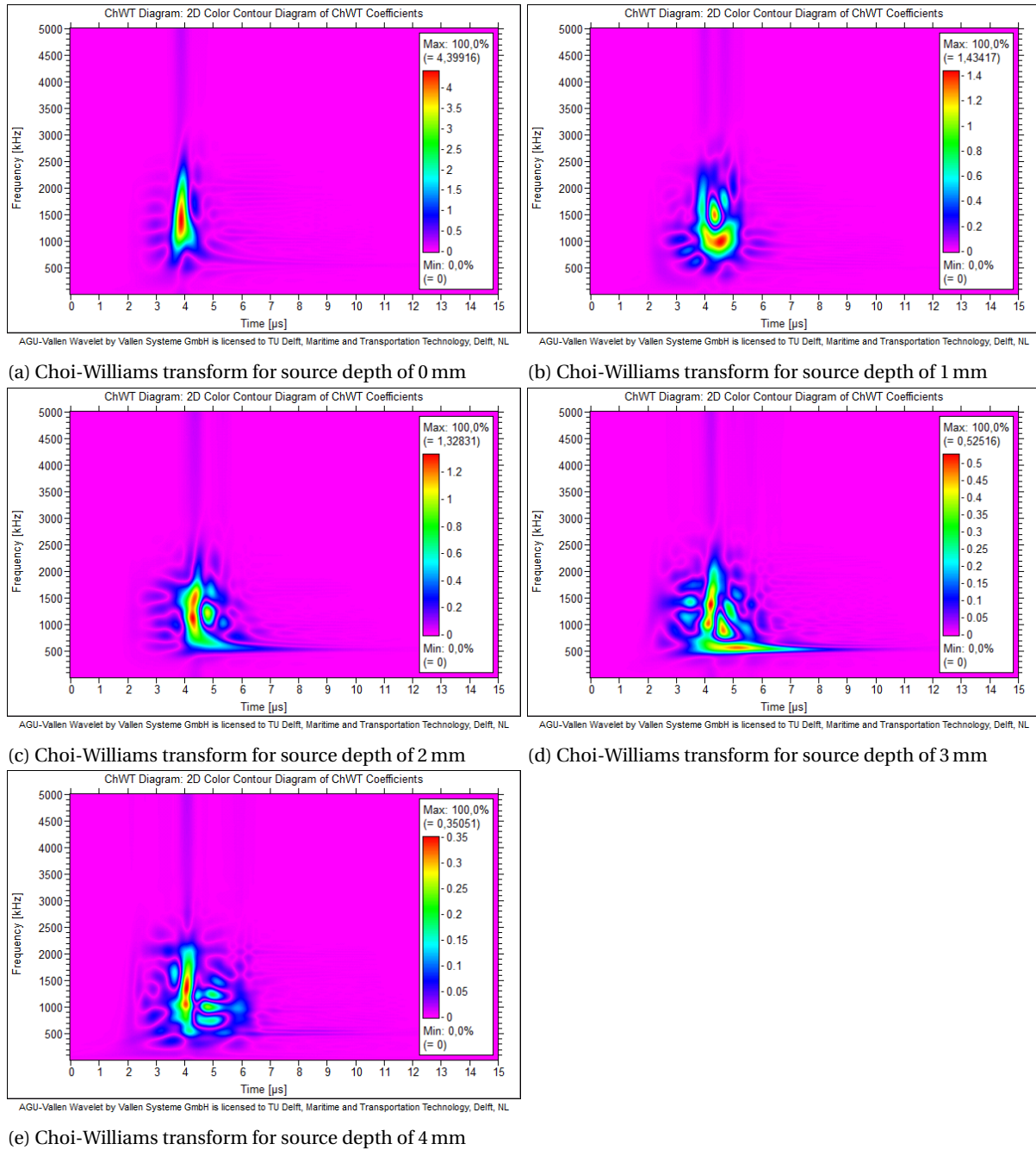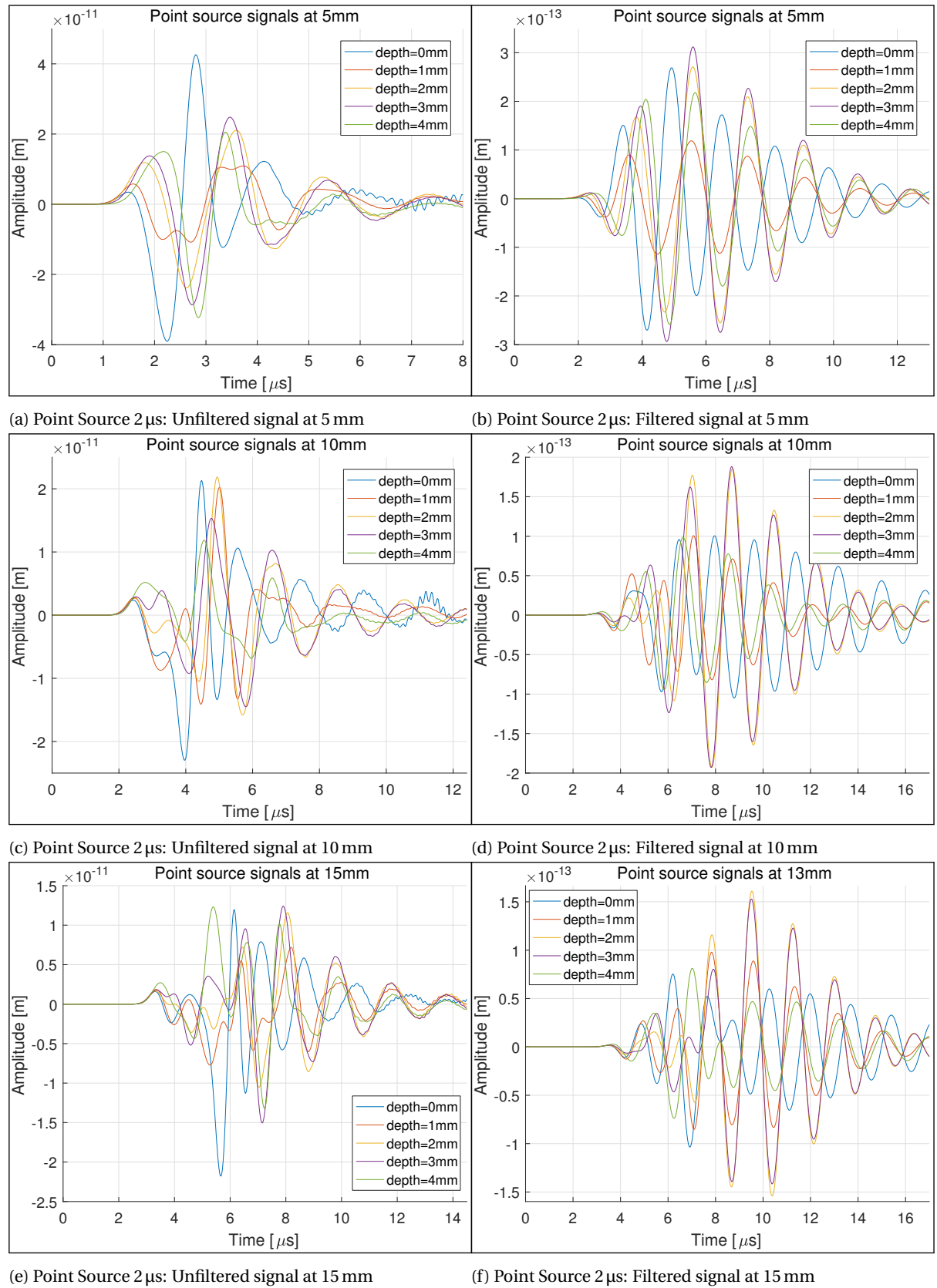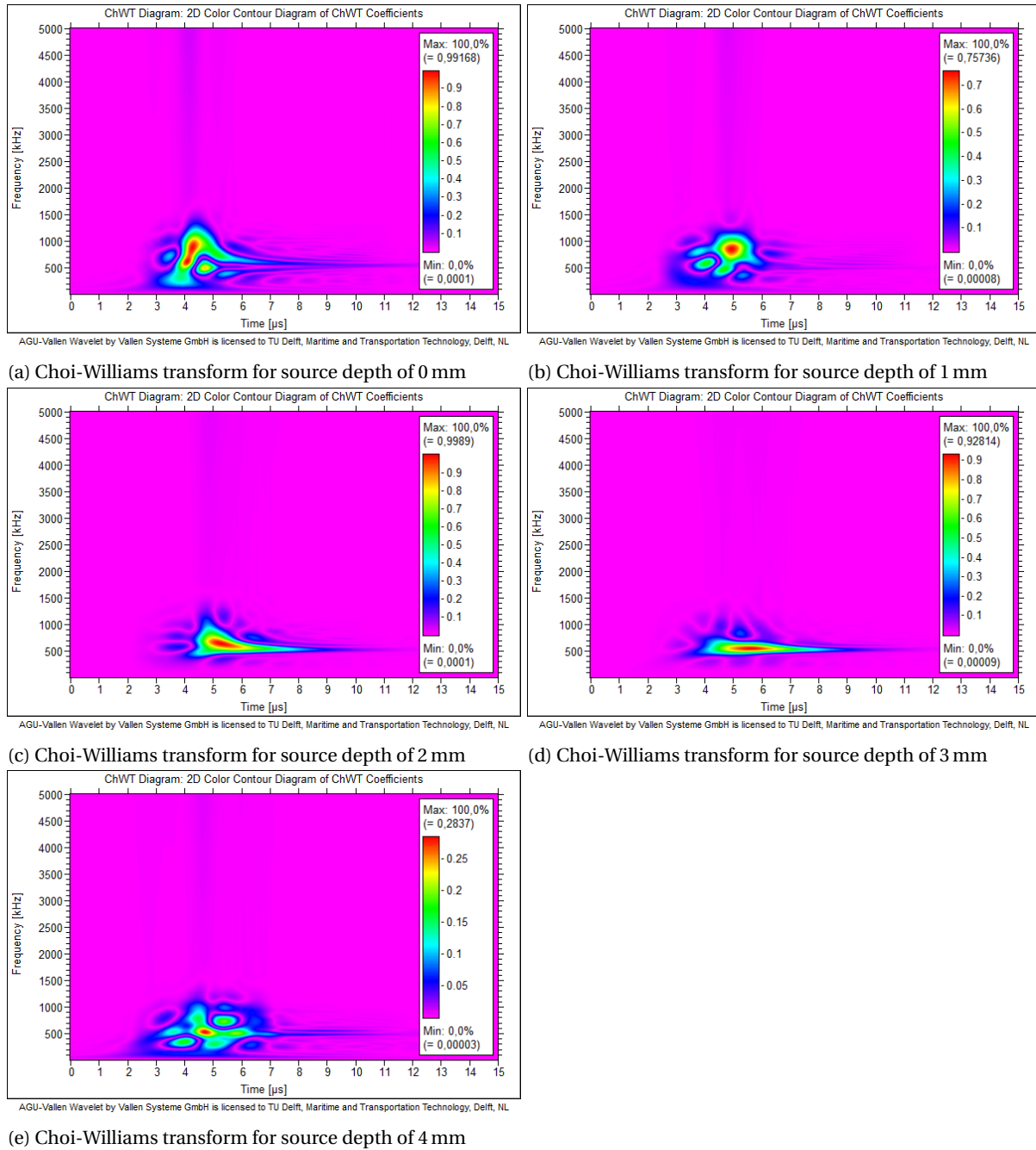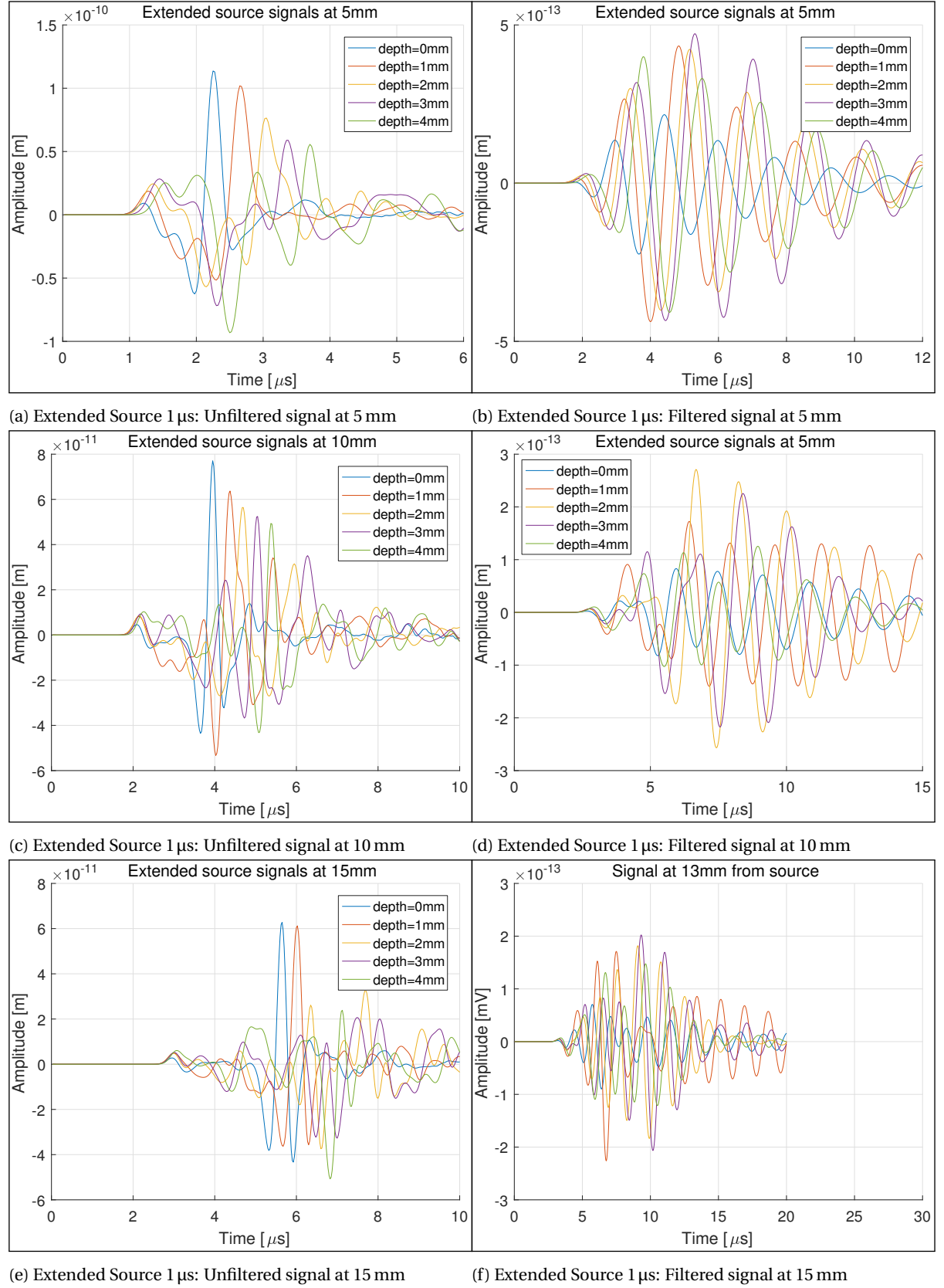(e) Choi-Williams transform for source depth of 4 mm
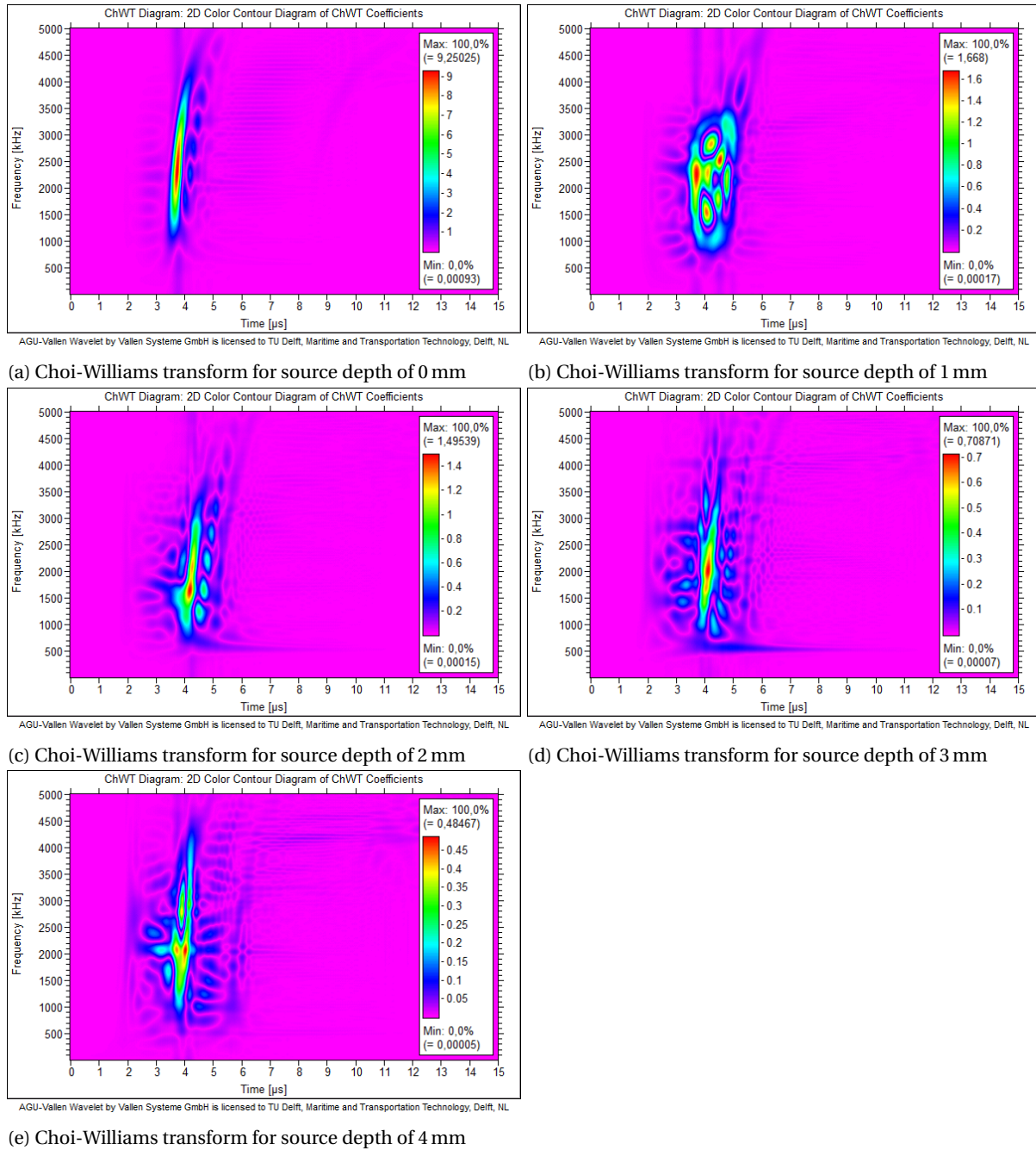
Figure B.2: CW transformations of Point Source 0.5 μs signals, at 10mm travel distance and varying depths

(a) Point Source 1 μs: Unfiltered signal at 5 mm

(b) Point Source 1 μs: Filtered signal at 5 mm

(c) Point Source 1 μs: Unfiltered signal at 10 mm

(d) Point Source 1 μs: Filtered signal at 10 mm

(e) Point Source 1 μs: Unfiltered signal at 15 mm

(f) Point Source 1 μs: Filtered signal at 15 mm

Figure B.3: Point Source 1 μs signals at several distances from source

(a) Choi-Williams transform for source depth of 0 mm

(b) Choi-Williams transform for source depth of 1 mm

(c) Choi-Williams transform for source depth of 2 mm

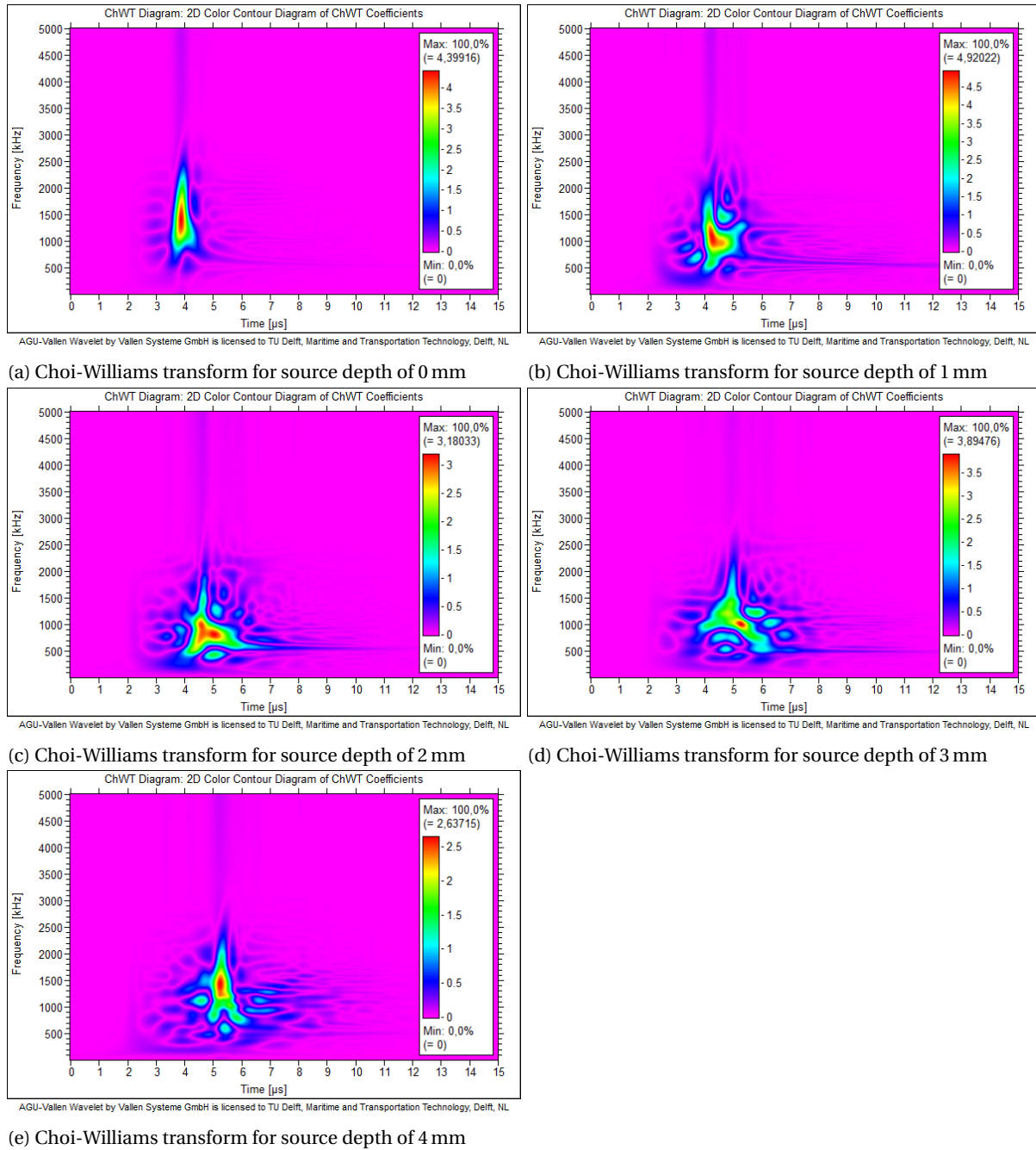(d) Choi-Williams transform for source depth of 3 mm

(e) Choi-Williams transform for source depth of 4 mm

Figure B.4: CW transformations of Point Source 1 µs signals, at 10mm travel distance and varying depths

(a) Point Source 2 µs: Unfiltered signal at 5 mm

(b) Point Source 2 µs: Filtered signal at 5 mm

(c) Point Source 2 µs: Unfiltered signal at 10 mm

(d) Point Source 2 µs: Filtered signal at 10 mm

(e) Point Source 2 µs: Unfiltered signal at 15 mm

(f) Point Source 2 µs: Filtered signal at 15 mm

Figure B.5: Point Source 2 µs signals at several distances from source

(a) Choi-Williams transform for source depth of 0 mm

(b) Choi-Williams transform for source depth of 1 mm

(c) Choi-Williams transform for source depth of 2 mm

(d) Choi-Williams transform for source depth of 3 mm

(e) Choi-Williams transform for source depth of 4 mm

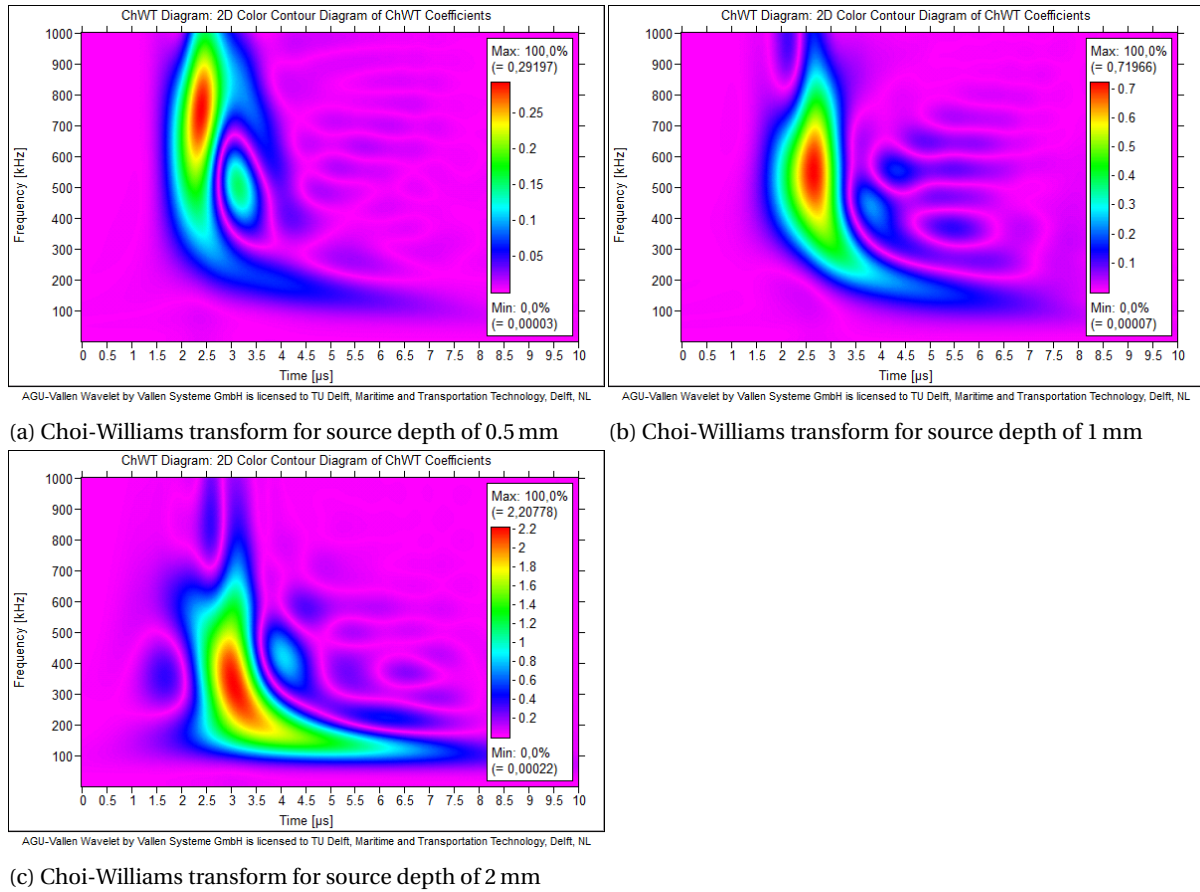Figure B.6: CW transformations of Point Source 2 μs signals, at 10mm travel distance and varying depths

(a) Extended Source 1 µs: Unfiltered signal at 5 mm

(b) Extended Source 1 µs: Filtered signal at 5 mm

(c) Extended Source 1 µs: Unfiltered signal at 10 mm

(d) Extended Source 1 µs: Filtered signal at 10 mm

(e) Extended Source 1 µs: Unfiltered signal at 15 mm

(f) Extended Source 1 µs: Filtered signal at 15 mm

Figure B.7: Extended Source 1 µs signals at several distances from source

(a) Choi-Williams transform for source depth of 0 mm

(b) Choi-Williams transform for source depth of 1 mm

(c) Choi-Williams transform for source depth of 2 mm

(d) Choi-Williams transform for source depth of 3 mm

(e) Choi-Williams transform for source depth of 4 mm

Figure B.8: CW transformations of Extended Source 1 µs signals, at 10mm travel distance and varying depths

(a) Separation Source: Unfiltered signal at 5 mm

(b) Separation Source: 100 kHz - 1000 kHz Bandpass filtered signal at 5 mm

(c) Separation Source: Filtered signal at 5 mm
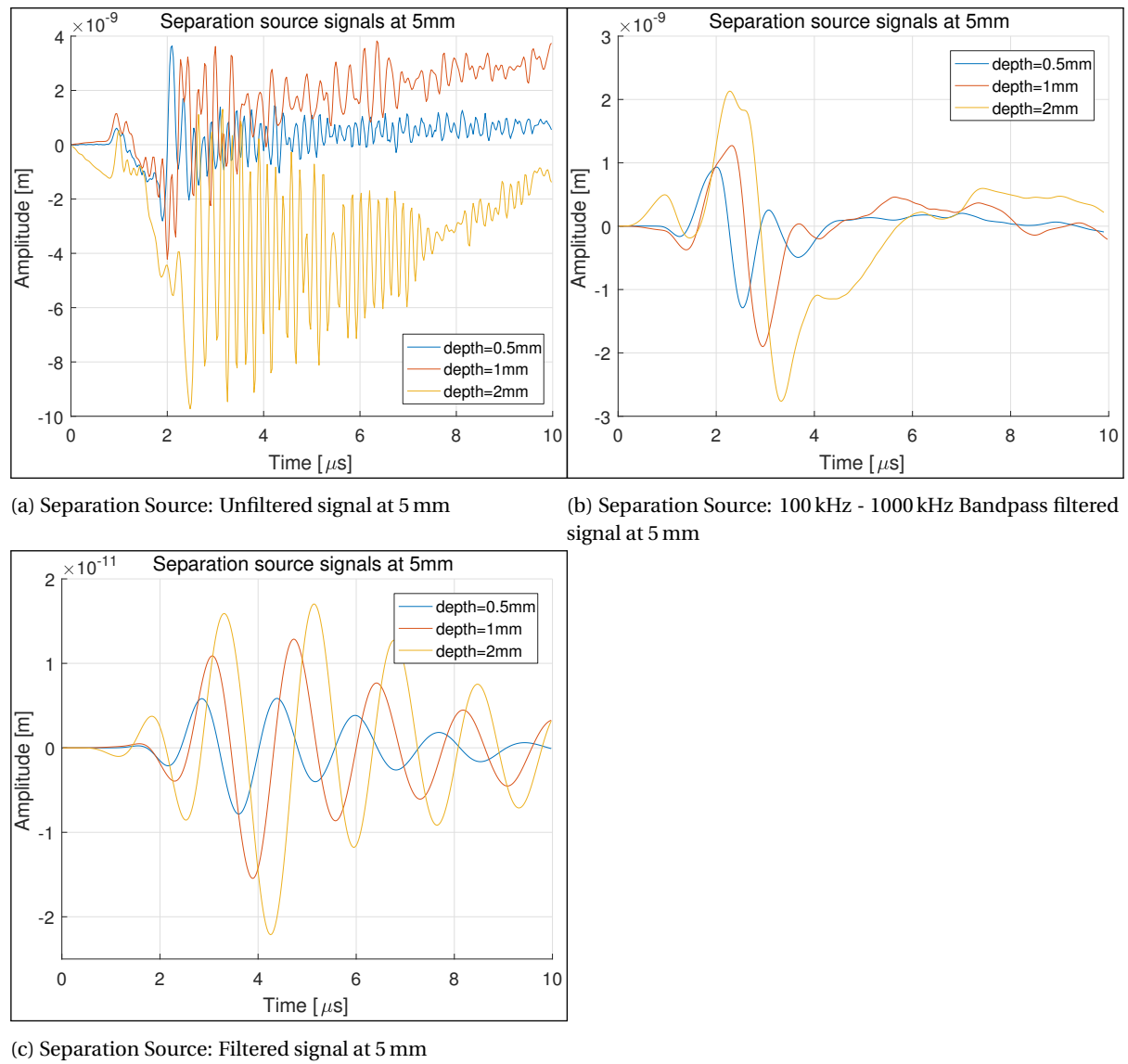
Figure B.9: Separation source signals at several distances from source

(a) Choi-Williams transform for source depth of 0.5 mm

(b) Choi-Williams transform for source depth of 1 mm

(c) Choi-Williams transform for source depth of 2 mm

Figure B.10: CW transformations of Separation Source signals, at 5mm travel distance and varying depths

(a) Signals of 0 mm source depth, 5 mm distance

(b) Signals of 0 mm source depth, 10 mm distance
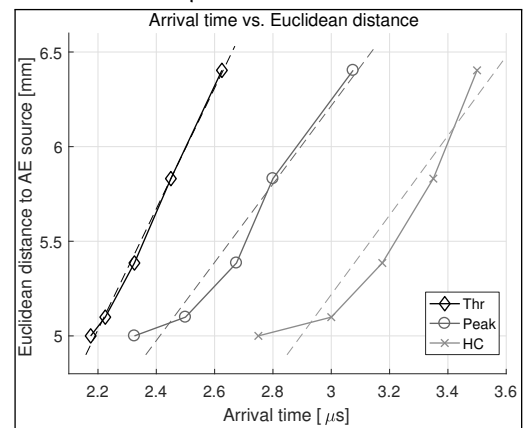

(c) Signals of 2 mm source depth, 5 mm distance
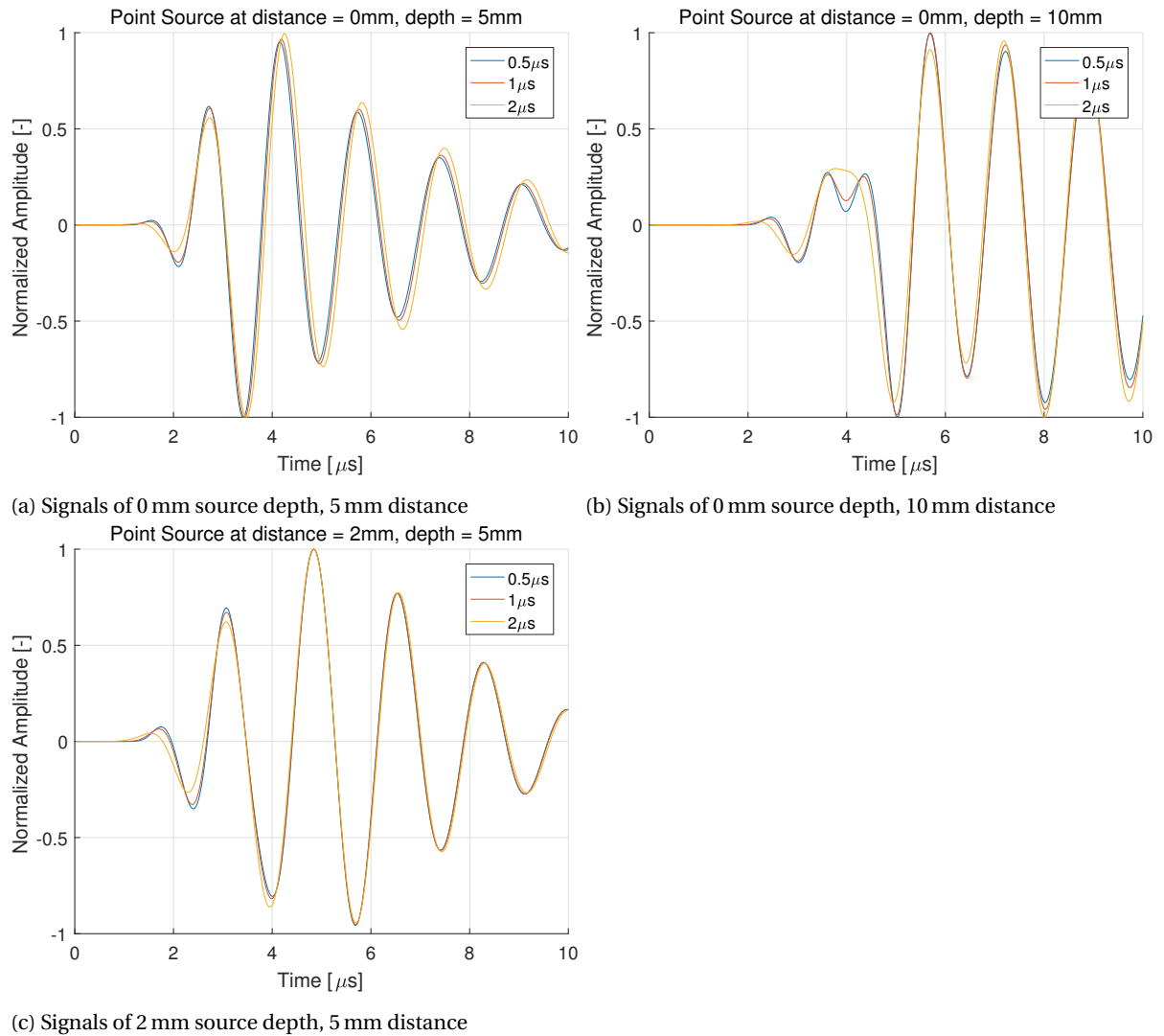
Figure B.11: Comparison of different rise times of Point sources

B.2. TIME OF ARRIVAL OF FATIGUE SOURCE SIMULATIONS
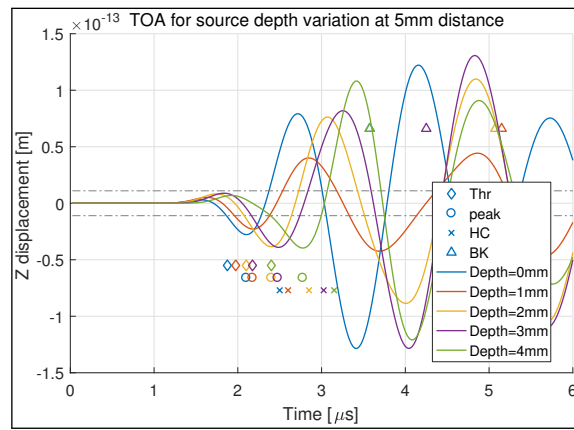
(a) Point Source 0.5 μs signals
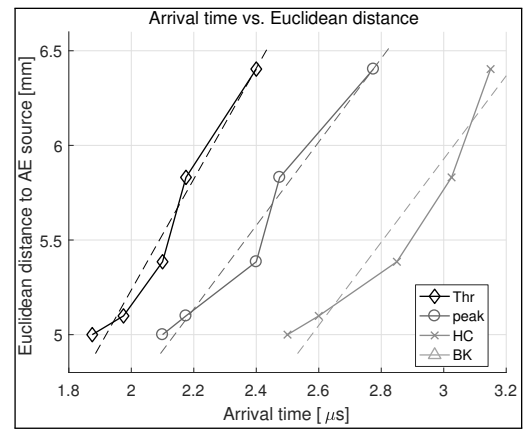
(b) Point Source 0.5 μs TOA
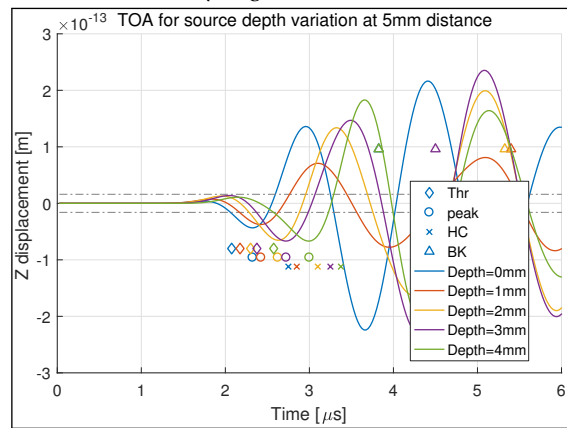
(c) Point Source 1 μs signals
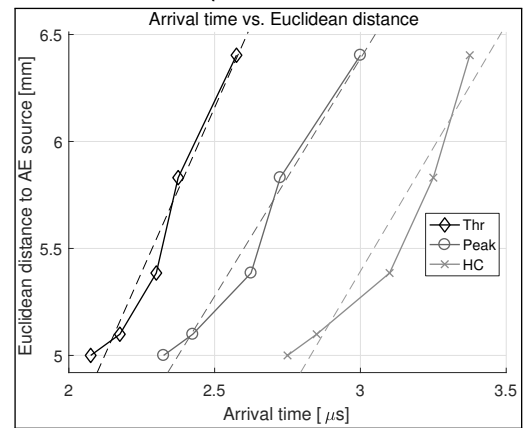
(d) Point Source 1 μs TOA
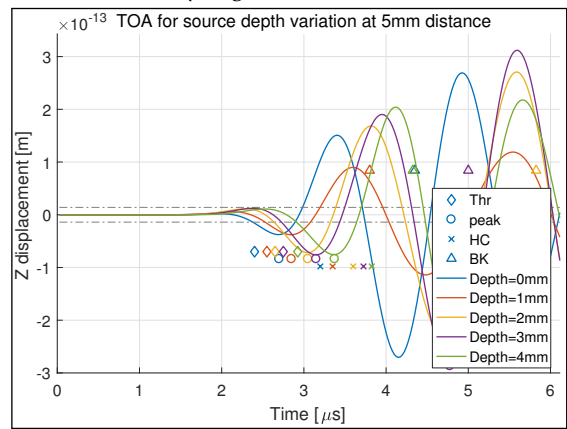
(e) Point Source 2 μs signals
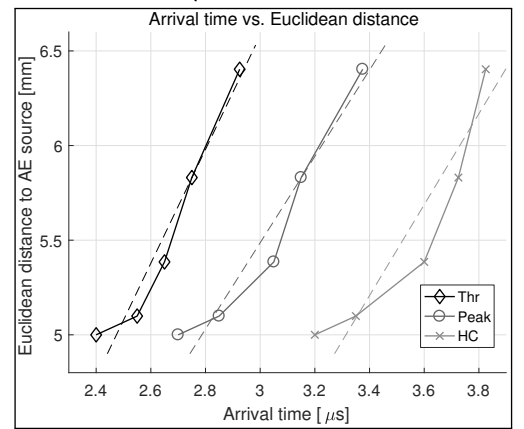
(f) Point Source 2 μs TOA
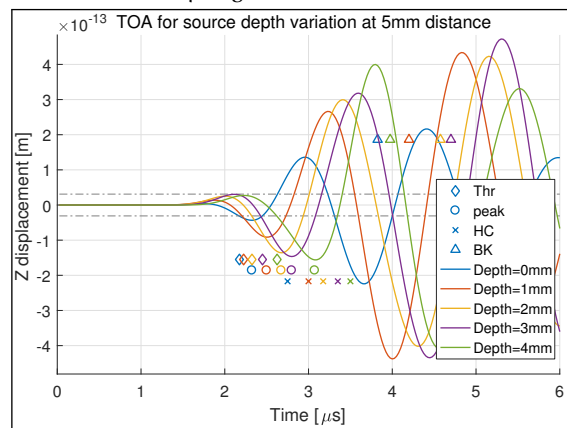
(g) Extended source signals

(h) Extended source TOA

Figure B.12: Signals and TOA's for varying source depths
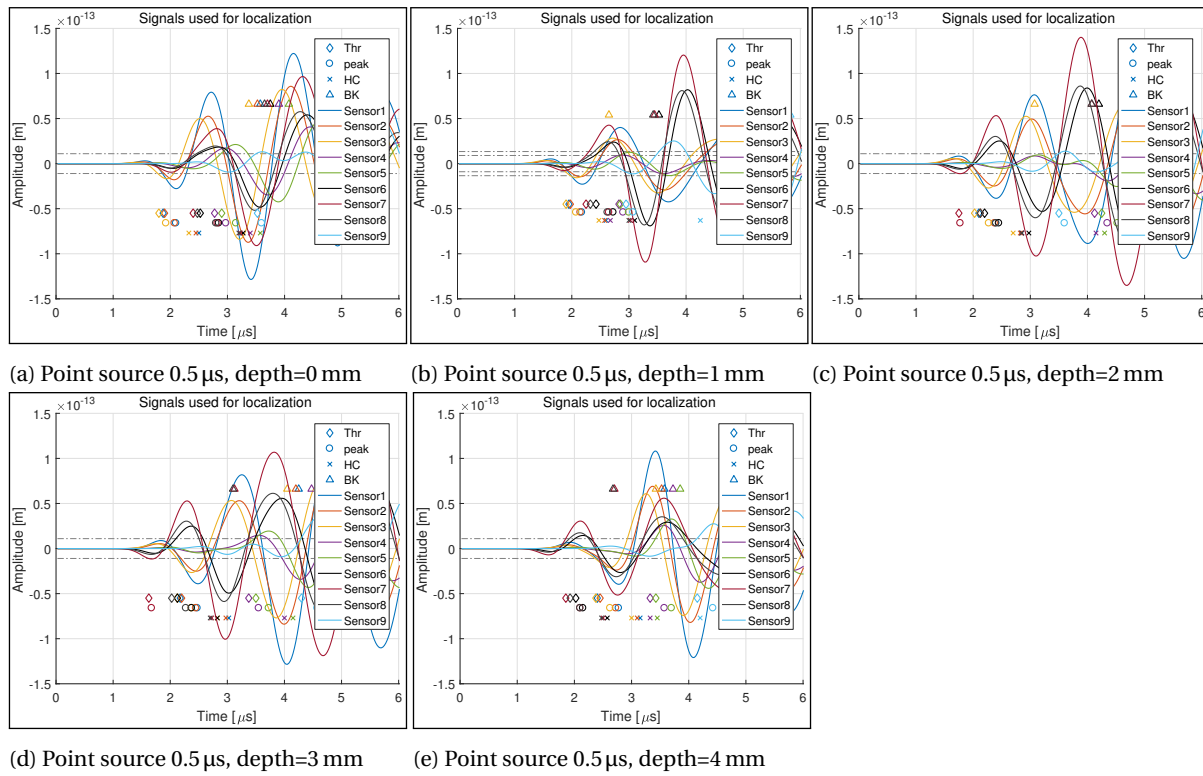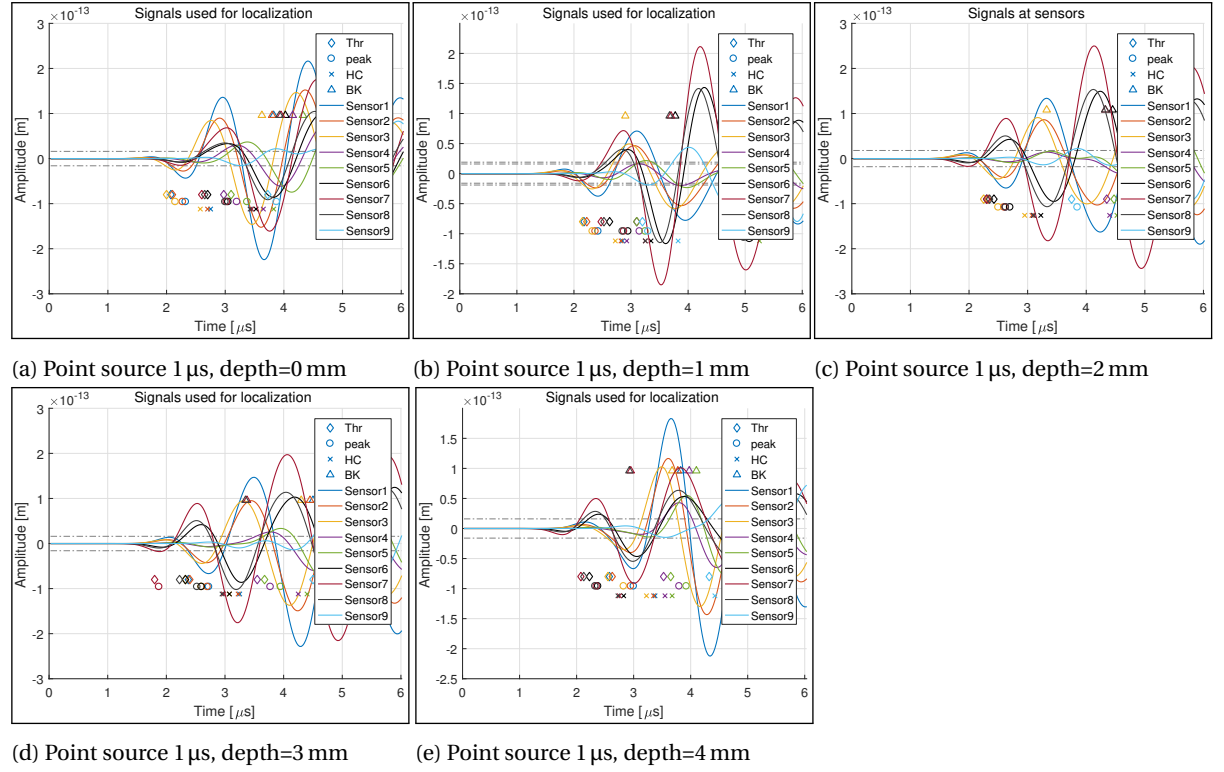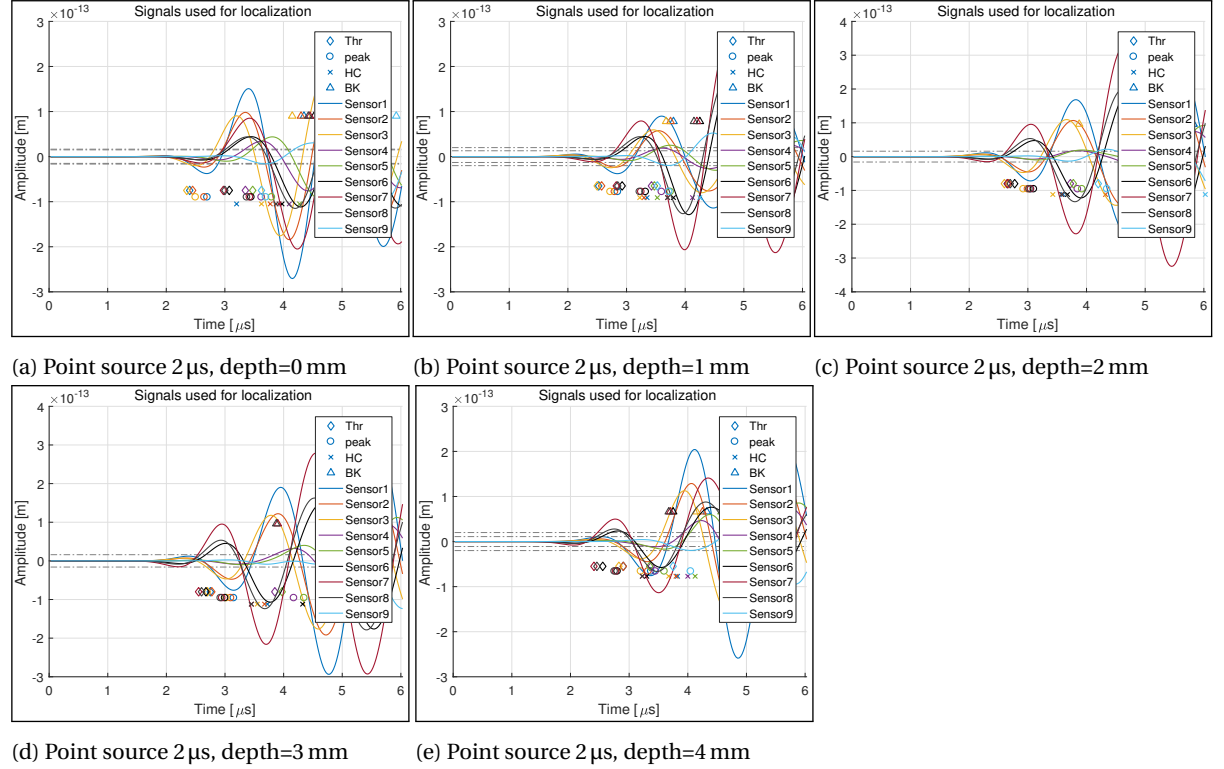
B.3. TIME PICKING FOR LOCALIZATION

(a) Point source 0.5 µs, depth=0 mm   (b) Point source 0.5 µs, depth=1 mm   (c) Point source 0.5 µs, depth=2 mm

(d) Point source 0.5 µs, depth=3 mm   (e) Point source 0.5 µs, depth=4 mm

Figure B.13: Point source 0.5 µs: Signals used for localization, and their picked times

(a) Point source 1 μs, depth=0 mm   (b) Point source 1 μs, depth=1 mm   (c) Point source 1 μs, depth=2 mm

(d) Point source 1 μs, depth=3 mm   (e) Point source 1 μs, depth=4 mm

Figure B.14: Point source 1 μs: Signals used for localization, and their picked times

(a) Point source 2 μs, depth=0 mm   (b) Point source 2 μs, depth=1 mm   (c) Point source 2 μs, depth=2 mm

(d) Point source 2 μs, depth=3 mm   (e) Point source 2 μs, depth=4 mm

Figure B.15: Point source 2 μs: Signals used for localization, and their picked times

(a) Extended source, depth=0 mm

(b) Extended source, depth=1 mm

(c) Extended source, depth=2 mm

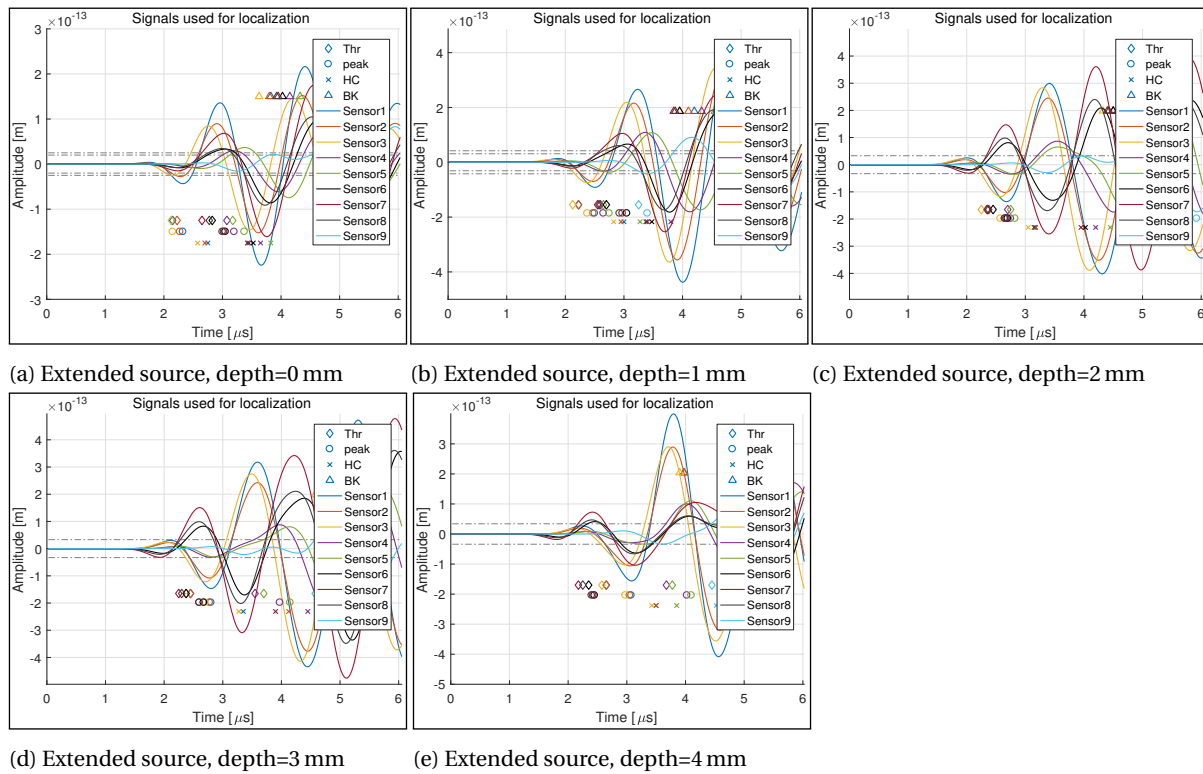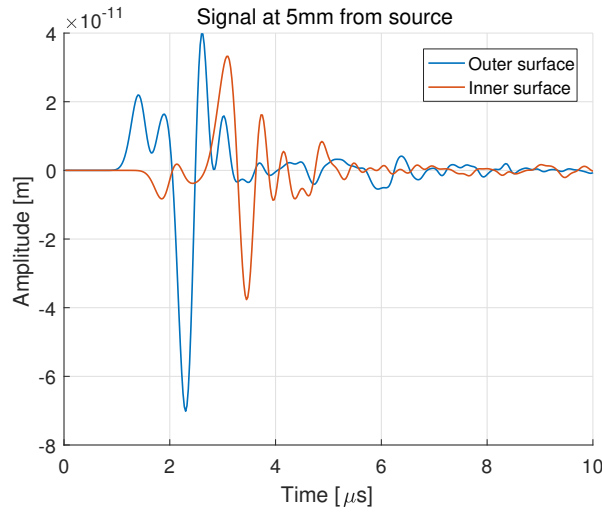(d) Extended source, depth=3 mm

(e) Extended source, depth=4 mm

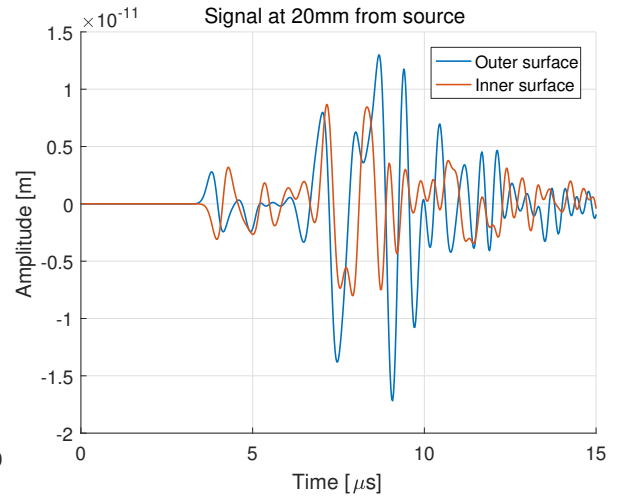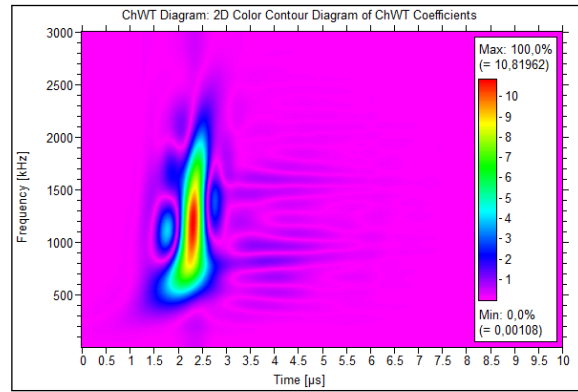Figure B.16: Extended source: Signals used for localization, and their picked times

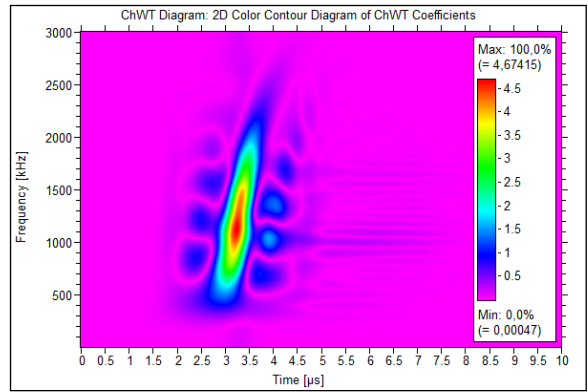# C

TUBULAR SPECIMEN AE SIMULATION
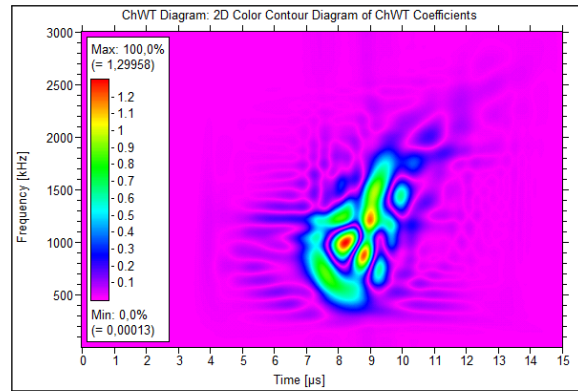
(a) Unfiltered signals at 5 mm travel distance

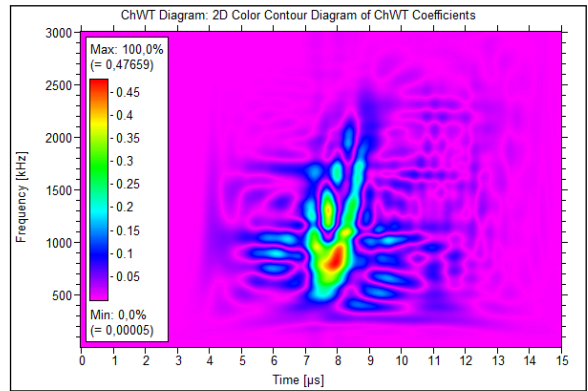(b) Unfiltered signals at 20 mm travel distance

(c) CW transform of outer surface signal at 5 mm

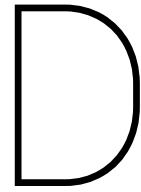(d) CW transform of inner surface signal at 5 mm

(e) CW transform of outer surface signal at 20 mm

(f) CW transform of inner surface signal at 20 mm

Figure C.1: Signals and their CW transforms at 5 mm and 20 mm at inner and outer surface of the tubular specimen, using crack depth of 3 mm

D

VALLEN EQUIPMENT

The following pages include the data sheets of the relevant acoustic emission monitoring equipment.

1. VS600-Z2 –Sensor data sheet [25].

2. VS600-Z2 –Single sensor verification, courtesy of Vallen Systeme GmbH.

3. AEP5H –Pre-amplifier data sheet [24].

4. ASIP-2 –Signal processor specification, [23].

AE–Sensor Data Sheet

VS600-Z2

The VS600-Z2 is a passive piezoelectric AE-sensor with integrated cable and full metal housing. Its frequency response is characterized by a peak at 600 kHz where it exhibits a resonance. Its small size makes it especially suited for being mounted on small samples where mounting space is restricted. Additionally it is ideally suited for gluing to the sample because of the full metal housing.
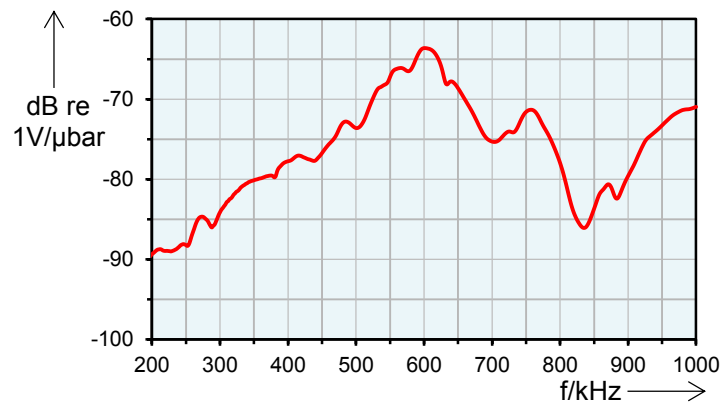
Technical Specification

Frequency Range (f$_{Peak}$) [kHz]	400 to 800 (600)	Size (D x H) [mm]	4.75 x 5.3
Capacity [pF]	200 (incl. Cable)	Weight [g]	20
Integrated Preamplifier	No	Case Material	Stainless Steel (1.4571/ 1.4404)
Operating Temperature [°C]	-40 to +110	Wear Plate	Stainless Steel (1.4571/ 1.4404)
Vibration – Sinus sweep	2 Oct/Min, 5 to 180 Hz, 40 g	Connector	SMA/BNC
Ingress Protection Rating	IP40	Shield Cross-Talk [dB]	< -80

Standards and Directives

EMC Directive	2014/30/EU
EMC Standards	EN61326-1:2013, EN61326-2-3:2013, EN61000-6-2:2006, EN61000-6-4:2011
Shock and Vibration Stand.	EN60068-2-6:2008
AE Standard	EN13477-1:2013, EN13477-2:2013

Accessories

Preamplifier	AEP5, AEP3N	Sensor Cable	(integral)
Mounting Holder			

Important instructions for your safety

The sensor was produced according to the state of technology and tested against highest quality standards and technical safety requirements. A risk of malfunction remains which can lead to danger to life of operator, uninvolved third parties as well as damage of object under test or objects in its vicinity. Read the safety instructions carefully before using the AE-sensor.

Supplemental safety directives

1. Read the Acoustic Emission Sensors document (http://www.vallen.de/quote-ref)
2. Make sure that you comply to regulations at the AE-sensor installation site
3. Store these instructions

⚠ CAUTION	*CAUTION indicates a hazardous situation which, if not avoided, may result in minor or moderate injury.*

Damaging of AE-sensor

An AE-sensor can get damaged when it is not operated within specified limits or handled carelessly. The function of the AE-sensor may be compromised or it may even be inoperable although its appearance e.g. housing, connector or wear plate do not indicate any damage.

Risk:

A damaged- or defective AE-sensor may not be able to detect potentially dangerous situations if it is used in a safety relevant inspection of e.g. pressure vessels or engineering structures such as bridges or dams. Failing of an object under inspection (e.g. bursting of a pressure vessel, collapsing of a bridge, etc.) may lead to fatal casualties.

How to avoid the risk of damaging an AE-sensor:

*   Do not store, transport or operate the sensor outside its specified environmental conditions
*   Do not drop the AE-sensor and handle it with care
*   Transport AE-sensors only in the boxes provided by Vallen Systeme

How to avoid using a non-functional AE-sensor:

*   Do not use an AE-sensor that is visibly damaged.
*   Check the function and response of an AE-sensor prior to an inspection or AE-test by the use of controlled artificial sources
*   Check the function and response of an AE-sensor in regular intervals or when suspected to be damaged or to have undergone severe environmental conditions
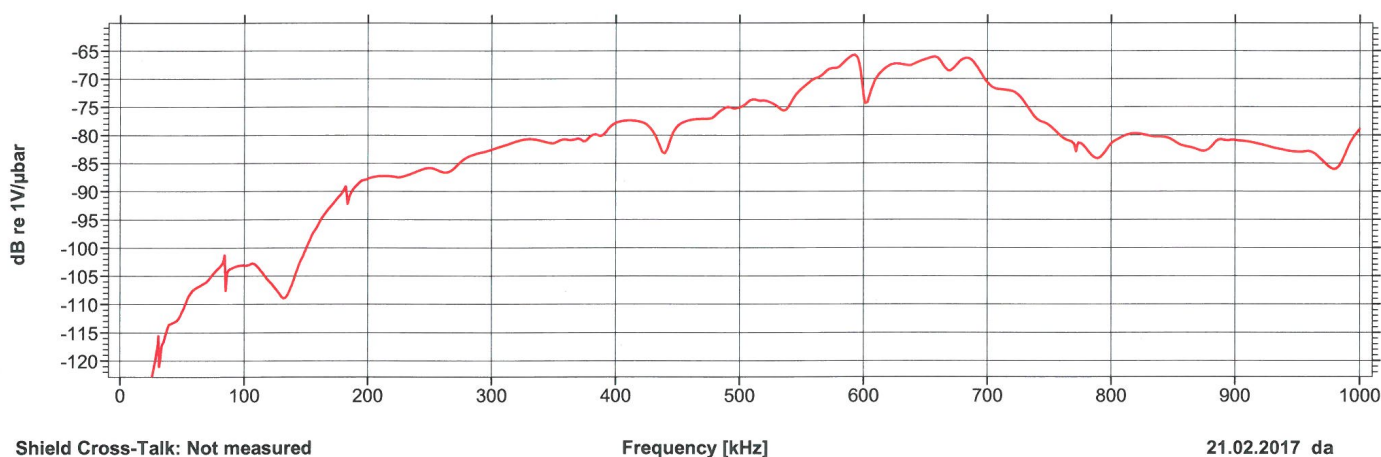
Vallen Systeme GmbH, Schaeftlarner Weg 26a, 82057 Icking, Germany
Email: info@vallen.de – www.vallen.de – Phone: +49 8178 9674-400

VS600-Z2_1512.docx
Page 2 of 2

Vallen Systeme GmbH

The Acoustic Emission Company

vallen
systeme

Test Certificate

VS600-Z2 No. ???

Shield Cross-Talk: Not measured   **Frequency [kHz]**   21.02.2017 da

This certifies that this transducer meets the performance characteristics listed in applicable Vallen Systeme GmbH specifications. Method based on ASTM standard E976. Face-to-face excitation: 0.1 Vrms at V103 (50 Ω), Offset -(114 + Gain) dB, coupling agent: light machine oil. For sensitivity to ANSI S1.2-1988, subtract 15 dB.
Measuring of Shielding Rejection n/a for this sensor type.

AE–Preamplifier Data Sheet

AEP5 / AEP5H

AEP5 / AEP5H are general purpose wide-band preamplifiers supporting single ended AE sensors. The only difference between AEP5 and AEP5-H are different frequency bandwidths. Gain can be set to 34 dB or 40 dB by a switch located inside the preamplifier. Changing the gain requires opening of the housing as described in the specification of preamplifiers. Thereby accidental change of gain is excluded.

As every preamplifier of Vallen Systeme GmbH the AEP5 / AEP5-H can put a voltage pulse (up to 450 V_{PP}) through the preamplifier to the connected AE-sensor (sensor coupling test) while the supply voltage for the preamplifier is interrupted.

Frequency Response
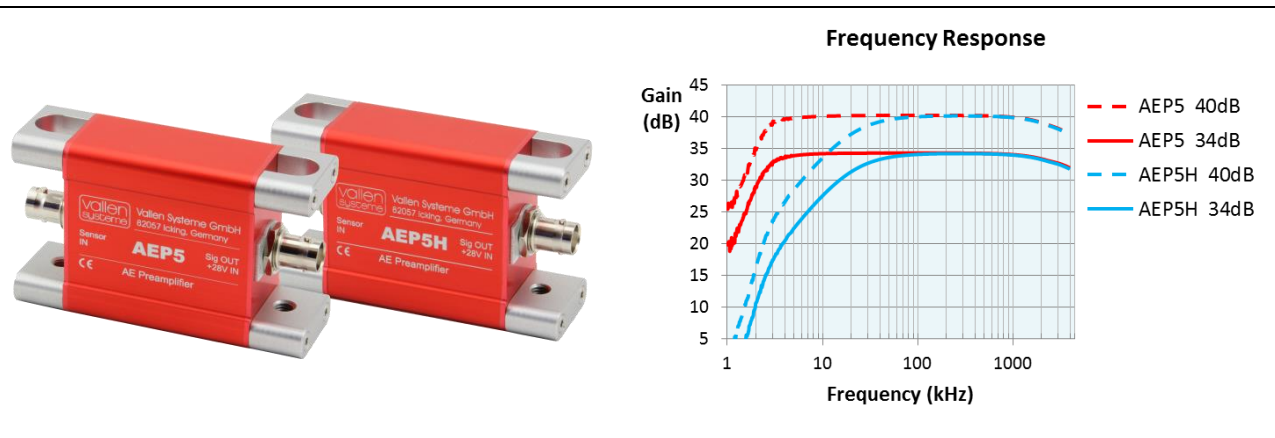
Technical Specification (typical)		
Preamplifier Gain @ 50 Ω [dB]	34, 40 switch selectable	
Bandwidth (-3 dB) [kHz]	2.5 to 2400 @ AEP5	20 to 2400 @ AEP5-H
Input Impedance [MΩ] | [pF]	50 | 22	
Power Supply [V_{DC}]	28 (fed in via signal cable)	
Typ. Power Cons. [W]	1.8	
Input Range [mV_{Peak}]	100 @ Gain 34 dB	50 @ Gain 40 dB
Output Range into 50 Ω [V_{PP}]	10	
Max. Puls Through [V_{PP}]	450 (suited for AMSY series)	
Noise (max. 1/s for dB$_{AE}$ values)	**Input 50 Ω**	**Input 330 pF**	**Input VS150-M**
Filter 95 to 300 kHz [dB$_{AE}$] | [µV$_{RMS}$]	12.5 | 0.8	10.9 | 0.7	24.7 | 4.3
Filter 95 to 850 kHz [dB$_{AE}$] | [µV$_{RMS}$]	18.5 | 1.6	16.9 | 1.3	25.8 | 4.9

Mechanical and Environmental Specification			
Input Connectors	BNC	**Case Material**	Aluminium
Output Connector	BNC	**Op. Temp. [°C]**	-20 to +85
Vibration – Sinus sweep	2 Oct/Min, 5 to 50 Hz, 20 g	**IP**	40
Size (H x W x L) [mm]	30 x 55 x 90	**Weight [g]**	160

Standards and Directives	
EMC Directive	2014/30/EU
EMC Standards	EN61326-1, EN61326-2-3, EN61000-6-2, EN61000-6-4
AE Standards	EN13477-1, EN13477-2

Accessories	
Mounting Holder	MAG4AEP5-V1, MAG4AEP5-V2
Cable	CBL-1-xM-V1 (BNC cable)
Filters	To be located in subsequent measurement chain (e.g. ASIP-2 with AMSY-6 series)

Supplemental directives

Read the Acoustic Emission Preamplifier document (http://www.vallen.de/quote-ref). Make sure that you comply with regulations at the installation site. Store these instructions for a later usage.

NOTICE	*NOTICE indicates a property damage message.*

Improper handling damages an AE-Preamplifier

- Do not store, transport or operate the AE-Preamplifier outside its specified environmental conditions
- Do not drop the AE-Preamplifier and handle it with care

How to avoid using a non-functional AE-Preamplifier

- Check function of AE-Preamplifier in regular intervals or when suspected to be damaged or have undergone severe environmental conditions

.

Vallen Systeme GmbH, Schaeftlarner Weg 26a, 82057 Icking, Germany
Email: info@vallen.de – www.vallen.de – Phone: +49 8178 9674-400

Datasheet_AEP5_1602.docx
Page 2 of 2

Figure 6: ASIP-2 with front panel elements: audio select switch, LEDs and BNC connectors

ASIP-2 is a dual channel AE-signal processor board which can be mounted in any of the chassis. Each ASIP-2 board and each channel on the board is processing data independent of each other. There are two versions of the ASIP-2:

- ASIP-2/S: standard version or
- ASIP-2/A: advanced version.

Both ASIP-2 versions can be used simultaneously within the same chassis. Following tables describe ASIP-2/S.

Mechanical properties

Mechanical properties	Description
Dimensions	Eurocard plug-in 100mm x 280 mm
Weight	0.32kg
Connectors	2x BNC, input impedance: 50Ω or 100kΩ
Flip switch	Toggles audio on/off (one position per channel)
Front panel LEDs	LEDs indicating threshold crossing, preamplifier saturation, preamplifier connected, DC-output overload, AC/DC input mode, pulsing mode, audio-selection (makes AE signal audible).
Transient recording (TR) memory	Each ASIP-2 can house one transient recorder storage module of type TR-2/xxMB (see section 3.2) to store waveforms in parallel to the classical AE features per channel.

Electrical properties

Electrical properties	Description
System noise	1.5µV$_{RMS}$, 6µV$_P$; (95-300kHz filter, referred to ±100mV$_{PK}$ range at preamplifier input; preamplifier not connected
Preamplifier power supply	28V$_{DC}$ @50Ω (see also input devices)
Input devices	Software selectable: 28V$_{DC}$@50Ω or AC@100kΩ

ASIP-2/S Signal processing

Signal processing	Description
Analogue band pass filters	1.6 or 18kHz (switch selectable) – 2.4MHz (at -3dB attenuation)
ADC	40MHz at 16 bit per channel
FIR low pass	Cut off: 3.6MHz (-6dB) at 40MSPS, 18 bit. Resulting bandwidth considering both, analogue and FIR Filter: 2.2MHz (at -3dB attenuation)
Application specific digital filter	Band-pass filter consisting of low-pass (LP) and high-pass (HP) filter of 8th order Butterworth each.
Digital filter roll-off attenuation	48dB/octave for LP and HP
Included digital filters	25-45kHz, 25-300kHz, 25-850kHz, 50-300kHz, 50-850kHz, 95-300kHz, 95-850kHz, 230-850kHz, Bypass (wideband option, e.g. required for System Verification and also recommended for Vallen Sensor Tester (VST)). Additional band pass filters available (see section 3.2
Digital filter selection	Software selectable for each channel individually.

Transient Recording (needs hardware option TR-2)

Transient data recorded to onboard DRAM. For available sizes of onboard DRAM see section 3.2

Transient Recording	Description
Sample interval	Programmable between 625kHz to 10MHz (1-16x0.1µs), globally valid for all AE-channels
Maximum samples per record	2M samples
Pretrigger	Individually programmable per AE-channel up to 64k samples
Trigger modes	Four trigger modes defined globally across multiple chassis for individual Trigger groups: Internal-, Pool- (Pool-trigger is when the first-hit channel simultaneously triggers all transient recorders of channels defined as Pool or Slave), Master- (Master triggers its own transient recording plus transient recording of all Slave and Pool channels) and Slave- (transient recording of slave channels can only be triggered by a Master channel) trigger.

Transient Recording	Description
Trigger group	A subset of channels, even across multiple chassis can be assigned to a trigger group. Trigger modes are applied per trigger group. The first hit channel of a trigger group triggers the other channels according to the selected modes. Each channel can be assigned to one trigger group, only
Recording modes	Two recording modes: Fixed page length recording: a predefined number of samples is recorded per trigger Duration adapted recording: number of samples that are recorded per trigger depend on duration of hit, pretrigger samples and post duration samples; maximum length of record is 2M samples.

Hit assembly

Hit assembly parameters	Description
Threshold	Software selectable for each AE-channel individually. Fixed or floating threshold.
Duration discrimination time (DDT)	A time setting used for discriminating hits
Rearm time (RAT)	A timer setting used for discrimination hit cascades

Feature extraction

Dual core feature extractor with loadable firmware for optimum flexibility.

Hit processing	Description
Sampling rate	10MHz
Arrival time resolution	100ns
Arrival time bit width	63bit
Peak amplitude resolution	Max (0.375dB, 76.3µV/Gain)
Threshold resolution	Max (0.375dB, 76.3µV/Gain)
Rise time resolution	Max (200ns, 0.025%)
Duration resolution	Max (200ns, 0.025%)
Ring down count resolution	16bit
Hit cascade[1] features	Number of cascaded hits, cascaded counts, cascaded energy and cascaded signal strength of the complete hit cascade[1]. Maximum number of hits in a hit cascade: 127
Hit flags	Hit flags indicating a time-out-hit, artificially started hit, hits because of pulses (active and passive), saturation of ADC

---

[1] Hit cascade: A hit cascade consists of hits that follow each other within an interval less than the rearm time (RAT). Features of a hit cascade are number of hits, sum of ring down counts and sum of energy of hits in a cascade. These features are part of the data set generated with the first hit of a cascade.

	and many more.
Energy calculation	True Energy
Hit processing	**Description**
Energy resolution	$1.8 * 10^{-18} V^2 s$ referred to sensor signal at 34dB preamplifier gain.
Energy units	$1 eu = 10^{-14} V^2 s$
True RMS resolution (true RMS before a hit)	<1 µV resolution referred to sensor signal at 34dB preamplifier gain.
True RMS resolution of a hit	<1 µV resolution referred to sensor signal at 34dB preamplifier gain, needs SW-option VAEUPE: User Processor Extension
Signal Strength resolution	0.3pVs referred to sensor signal at 34dB preamplifier gain.
Signal Strenght units	$nVs = 10^{-9} Vs$
Average noise level before a hit	<1 µV resolution referred to sensor signal at 34dB preamplifier gain.
Average noise level of a hit	<1 µV resolution referred to sensor signal at 34dB preamplifier gain; needs SW-option VAEUPE: User Processor Extension

Hit time-outs

A hit is artificially terminated after about 100ms. An artificial hit is started automatically after a hit is timed-out. A hit that is timed-out and thus terminated is assigned a "time-out" hit flag. A hit that is artificially started is assigned an "artificially started" hit flag.

Hit processing performance

About 19,000 hits/second (peak) can be filled into the buffer of each AE-channel, 100,000 hits/second can be transferred to the PC and stored on the hard disk drive continuously, in parallel with data analysis program.

Above 100,000 hits per second a buffer overflow of hit-data is avoided by setting the respective ASIP-2 into long duration mode, when the ASIP-2 buffer runs half full. The whole chassis is set into long duration mode if the USYC buffer runs 80% full.

Status data

Status data is generated per time interval. The time interval is software selectable. Following status data is generated:

- RMSS: RMS at the time of the generation of a status data set. RMS is calculated exclusive AE-signals that are part of hits.

- ENYS: True Energy cumulated between two status data sets

- SSS: Signal strength cumulated between two status data sets

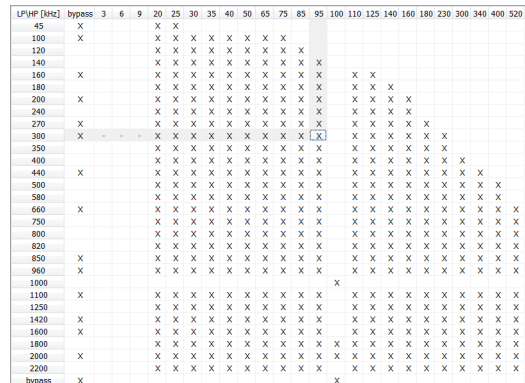- THRS: threshold at the time of the generation of a status data set

3.1 ASIP-2/A features

The ASIP-2/A fulfills the ASIP-2/S specification (see section 3). Additional features are listed below:

Electrical properties (additional to ASIP-2/S)

Electrical properties	Description
Preamplifier power supply	Software selectable: $28V_{DC}$ @50Ω (see also input devices), 8-28 V_{DC} (programmable voltage) @ 200Ω, 8-28 V_{DC} (programmable voltage) @ 50Ω
Input devices	Software selectable: $28V_{DC}$ @50Ω, AC@100kΩ, 8-28V_{DC} @200Ω, 8-28V_{DC} @50Ω

Signal processing (additional to ASIP-2/S)

Signal processing	Description
Application specific digital filters	over 500 band pass filters available *Figure 7: matrix of available filters for up to 20MHz sampling rate. Rows for low pass-, columns for high pass selection*
Digital filter order	8th order Butterworth at up to 20MSPS (each high- and low pass) 4th order Butterworth at 40MSPS (each high- and low pass)
Transient recording (TR)	Up to 40MSPS (requires TR-2)
Input ranges	Three software selectable input ranges (10Vpp, 5Vpp, 2.5Vpp) for better resolution for applications with low amplitude.
Notch filter stage	Notch filter rejects user-selectable frequencies. Max. notch filter frequency: 250kHz (8th order) or 500kHz (4th order) Notch filter rejects: • at 10MHz sampling rate: 4 frequencies each 2nd order. • at 20MHz sampling rate: 2 frequencies each 2nd order. • at 40MHz sampling rate: 1 frequency of 2nd order.

Feature extraction (additional to ASIP-2/S)

Hit processing	Description
Arrival time resolution	100ns, 50ns or 25ns (software selectable)
Arrival time bit width	63bit

3.2 Options for ASIP-2

Application specific filters (ASIP-2/S only)

Any number of application specific filters can be enabled for an ASIP-2/S.

Item-code	Description
DigBP-2/*hi-pass – low-pass*	One digital band-pass filter configuration for one ASIP-2 (i.e. for two channels). Over 500 digital band-pass filters are available for selection (see the table below)

Select corner frequencies from the following lists:

Filter type	Corner frequencies
Hi-Pass [kHz]:	3.1^+, 6.2^+, 9.3^+, 12.4^+,17^+, 20^+, 20, 25, 30, 35, 40, 50, 65, 75, 85, 95, 100*,110, 125, 140, 160, 180, 230, 300, 340, 400, 520
Low-Pass [kHz]:	45, 100, 120, 140, 160, 180, 200, 240, 270, 300, 350, 400, 440, 500, 580, 660, 750, 800, 820, 850, 960, 1100, 1250, 1420, 1600, 1800*, 2000*, 2200*

Examples

DigBP-2/95-300 means digital bandpass 95-300kHz,

DigBP-2/25-1420 means digital bandpass 25-1420kHz

$^+$ For these high-pass filters the switch on the analog filter shall be "ON" (for 1.6kHz high-pass), otherwise "OFF" (for 18kHz high-pass). Signal processing of frequencies below 12 kHz needs input mode "AC@100K" (no DC supply for preamplifier possible).

* These filters are of 4th order running at 40MHz.

Transient recording memory

Item-code	Description
TR-2/2GB	2GB TR module for ASIP-2 (1 GByte per channel)
TR-2/512MB	512MB TR module for ASIP-2 (256 MByte per channel)
TR-2/16MB	16MB TR module for ASIP-2 (8MB per channel)